UNIVERSITY OF CALIFORNIA SAN DIEGO

Investigation of the spatial distribution and temporal evolution of current and magnetic fields in gas-puff Z-pinches

A dissertation submitted in partial satisfaction of the
requirements for the degree
Doctor of Philosophy

in

Engineering Sciences (Engineering Physics)

by

Nicholas Aybar

Committee in charge:

Professor Farhat Beg, Chair
Professor Alexey Arefiev
Doctor Christopher Holland
Professor Antonio Sanchez
Professor Cliff Surko

2022

The dissertation of Nicholas Aybar is approved, and it is acceptable in quality and form for publication on microfilm and electronically.

University of California San Diego

2022

DEDICATION

To my family and friends.

EPIGRAPH

Let no man imagine that he has no influence. Whoever he may be, and wherever he may be placed, the man who thinks becomes a light and a power.

—Henry George

TABLE OF CONTENTS

List of Abbreviations

AMF	Axial magnetic field
CESZAR	Compact experimental system for Z-pinch and ablation research
CVR	Current viewing resistor
LDP	Low density plasma
LTD	Linear transformer driver
LTE	Local thermodynamic equilibrium
MCP	Microchannel plate
MHD	Magnetohydrodynamic
MRTI	Magneto Rayleigh-Taylor instability
QEOS	Quotidian equation of state
RLC	Resistor-inductor-capacitor circuit
STP	Standard temperature and pressure
XUV	Extreme ultraviolet

LIST OF FIGURES

ACKNOWLEDGEMENTS

This work has relied on the support and input of many individuals over several years to whom I owe much gratitude.

I would like to thank my advisor, Farhat Beg, for always challenging me to execute research at a high level and encouraging me to try new things.

I would like to thank my friend and mentor Fabio Conti, who has always helped me understand the various challenging topics in plasma physics and improved as an experimentalist since my first day in the lab. Studying plasma physics starting while coming from education in environmental engineering was a major challenge, but it was made less so by having a patient mentor in Fabio. I am grateful for the many hours we have spent together both within various laboratories and outside them as well.

Running MHD simulations without the help and guidance of Jeff Narkis would have been impossible. I want to thank Jeff for his support in all things MHD, and for always hearing out my sometimes half-baked ideas in addition to always providing excellent feedback for papers and talks. I also owe gratitude to David Reisman for offering his support and technical expertise regarding MHD modeling.

Marko Cvejic and Dimitri Mikitchuk offered a great deal of knowledge and support in my pursuit to learn the spectroscopic techniques which I have relied so heavily on. I want to thank Marko and Dima not only for sharing their knowledge, but for valuable technical discussions on this topic.

Running experiments in the CESZAR laboratory would not have been possible without the impeccable support of Vladimir Fadeev, not only for designing, building and maintaining the many systems in the lab, but also for making the day to day lab activities enjoyable, along with Apsara Williams and Joshua Guy.

I owe much gratitude to my wife, Maylis for supporting me as a researcher in every aspect.

Chapter 4 includes material as it appears in “Azimuthal magnetic field distribution in

gas-puff Z-pinch implosions with and without external magnetic stabilization", N. Aybar, M. Dozieres, D. B. Reisman, M. Cvejic, D. Mikitchuk, F. Conti, E. Kroupp, R. Doron, Y. Maron, and F. N. Beg, Phys. Rev. E, **103**, 053205 (2021). N. Aybar was the primary author of this paper.

Chapter 5 includes material as it appears in "Dependence of Plasma-Current Coupling on Current Rise Time in Gas-Puff Z-Pinches", N. Aybar, F. Conti, M. Cvejic, D. Mikitchuk, M. Dozieres, E. Kroupp, J. Narkis, Y. Maron, and F. N. Beg, IEEE Trans. Plasma Sci., submitted for publication in 2021. N. Aybar was the primary author of this paper.

Chapter 6 contains material which is being prepared for submission for peer-reviewed publication as "Role of Initial Conditions in Liner-on-Target Implosions" N. Aybar, F. Conti, J. Narkis, and F. Beg. N. Aybar is the primary author of this paper

VITA

2016	B. S. in Environmental Engineering *cum laude*, San Diego State University
2016-2022	Graduate Student Researcher, University of California San Diego
2019	M. S. in Engineering Sciences (Engineering Physics), University of California San Diego
2022	Ph. D. in Engineering Sciences (Engineering Physics), University of California San Diego

PUBLICATIONS

N. Aybar, M. Dozieres, D. B. Reisman, M. Cvejic, D. Mikitchuk, F. Conti, E. Kroupp, R. Doron, Y. Maron, and F. N. Beg, "Azimuthal magnetic field distribution in gas-puff Z-pinch implosions with and without external magnetic stabilization", *Physical Review E*, **103**, 053205 (2021).

N. Aybar, F. Conti, M. Cvejic, D. Mikitchuk, M. Dozieres, E. Kroupp, J. Narkis, Y. Maron, and F. N. Beg, "Dependence of Plasma-Current Coupling on Current Rise Time in Gas-Puff Z-Pinches", Submitted to *IEEE Transactions on Plasma Science*, (2021).

N. Aybar, F. Conti, J. Narkis, F. N. Beg, "Role of Initial Conditions and breakdown in Gas-Puff Z-Pinches", prepared for submission to *Physics of Plasmas*

ABSTRACT OF THE DISSERTATION

Investigation of the spatial distribution and temporal evolution of current and magnetic fields in gas-puff Z-pinches

by

Nicholas Aybar

Doctor of Philosophy in Engineering Sciences (Engineering Physics)

University of California San Diego, 2022

Professor Farhat Beg, Chair

Gas-puff Z-pinches are intense pulsed x-ray or neutron sources. In gas-puff Z-pinches, a pulsed current is delivered to a cylindrical gas column, leading to an implosion of plasma until it stagnates on axis and generates x-rays or neutrons. The distribution of the current within the imploding plasma greatly impacts the kinetic energy of the imploding plasma, the state of the stagnated plasma and therefore the radiation achieved. This dissertation examines the delivery of current in conventional pulsed power drivers and the latest pulsed power systems based on linear transformer driver technology throughout the implosion process.

A spectroscopic technique exploiting the polarization properties of the Zeeman effect

allow for local measurements of the azimuthal magnetic field (B_θ) in the high density conditions of the implosion phase.

This technique was employed on the CESZAR LTD (500 kA peak current, 180 ns rise time) and on a conventional, slower rising driver (300 kA peak current, 1500 ns rise time). Experiments on the conventional driver, performed at the Weizmann Institute of Science, Israel, found that over 80% of the current flowed within the imploding plasma. In addition, a pre-embedded axial magnetic field was shown to produce radial profiles of B_θ consistent with MHD simulations.

On the CESZAR LTD, 50% or less of the current was flowing within the imploding plasma. The radial charge state distribution observed on the CESZAR driver indicates that a trailing plasma composed of higher charge states and lower densities carries a significant portion of the current.

Furthermore, modifications to the electrode geometry of the LTD and to the initial gas density profile greatly impact the plasma-current coupling. Installing pins in the cathode oriented toward the anode improved the plasma-current coupling, ostensibly by creating a favorable initial breakdown plasma. Using a relatively short valve opening duration led to an increase from $\sim 50\%$ to $\sim 70\%$ of current in the plasma early in the implosion.

Chapter 1

Introduction

1.1 Introduction to Z-Pinches

The pinch effect is a phenomenon observable in many natural and laboratory electrical discharges. It occurs when an electrical current passing through an object and its associated magnetic field compress the material onto its axis. Lightning and solar flares are examples of the pinch effect found in nature. When the current is flowing in the axial or "Z" direction, and the self-generated magnetic field is therefore oriented in the azimuthal or "θ" direction, the configuration is known as a "Z-Pinch". The acting force in this process is called the Lorentz force, quantified by a cross product of the current and magnetic field, $\mathbf{J} \times \mathbf{B}$. The earliest laboratory Z-pinches were devices designed to counteract the thermal pressure of the hot plasma with the Lorentz force supplied by an electrical current, producing a pressure equilibrium during a steady-state phase [1, 2, 3]. Later, dynamic Z-pinches were developed in which the material would be accelerated radially inward by the Lorentz force to tremendous velocities until stagnating near the central axis where the plasma's kinetic energy would be converted to thermal energy [4]. With sufficient compression, the material involved in a Z-pinch may reach extreme conditions, with temperatures exceeding 1 keV leading to k-shell x-ray yields of nearly 100 kJ [5]. The ability to achieve

such extreme conditions has led to a great deal of scientific study of laboratory Z-pinches over many decades with a variety of motivations including, but not limited to fundamental science of matter in high-energy density conditions (where pressure, $P > 1\,Mbar$), improving Z-pinches as x-ray sources, laboratory astrophysical plasma studies, and perhaps most of all, as a controlled thermonuclear fusion energy device [4].

Several varieties of laboratory Z-pinch configurations have been developed and continue to serve as experimental platforms. Metallic wire-array Z-pinches are a popular choice for producing high fluxes of k-shell x-ray emission, where the element can be chosen to achieve the desired photon spectrum [4]. Alternatively, wires composed of frozen deuterium are used with the aim of thermonuclear fusion [6]. To produce a point-like source of x-rays, linear wire-arrays loads can be twisted to form what is known as an X-pinch; the hot, dense plasma appears at the cross point of the wires, leading to a localized plasma at extreme conditions and intense radiation fluxes [7]. Additionally, so-called 'Hybrid' X-pinches were also developed using solid cone electrodes separated by a short wire to create a more well defined cross point [8]. Wire arrays inherently exhibit azimuthal non-uniformity, since the mass is always initially confined to discrete thin wires. Metallic shells can be used instead to improve uniformity [4]. However, the practical lower limit of metallic shell thickness means that a great deal of electrical energy is required to compress such massive shells or "liners", which most university-scale pulsed-power drivers are incapable of supplying. The Magnetized Liner Inertial Fusion (MagLIF) program carried out at Sandia National Laboratories uses a solid shell liner as part of its design intended to study thermonuclear plasmas [9]. Another way to achieve azimuthal uniformity of the load with a sufficiently low mass is to use gas loads instead of solid loads. Using a fast opening electromagnetic valve and nozzle, a cylindrical puff of gas can be injected into the anode-cathode gap of the pulsed-power driver. This is known as the gas-puff Z-pinch.

The work presented here is focused on studying the properties and evolution of magnetic fields and currents in gas-puff Z-pinches using experiments of varied driver parameters and

magnetohydrodynamic (MHD) simulations of such experiments.

1.1.1 Gas-puff Z-Pinches

The gas-puff Z-pinch process can be described in three phases. First, the neutral gas must be converted into a conductive material so that the driver current can flow through it, across the anode-cathode gap of the machine. This first step, or *breakdown phase*, is often achieved by a cascading breakdown event due to the initial portion driver pulse. However, to improve experimental reproducibility, a separate pre-ionization system can be utilized via several methods [10]. After the plasma is produced and current begins flowing, the current and its self-magnetic field begin to accelerate the plasma radially inward. This is known as the *implosion phase*. Finally, when the cylindrical plasma converges on its axis, the implosion ends and the highest densities and temperatures in the process are achieved; this is known as the *stagnation phase*. The three phase process is illustrated figure 1.1 below.

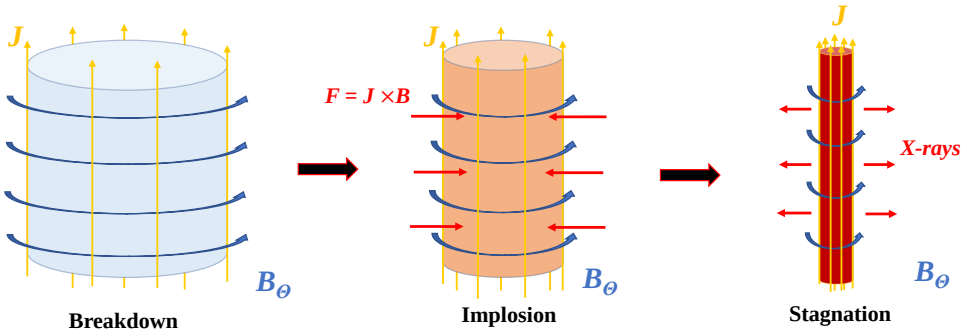

Figure 1.1: Illustration of three primary phases of a gas-puff Z-pinch. A conductive plasma is established in the breakdown phase, the current and magnetic field work on the plasma during the implosion phase until it collides on axis during the stagnation phase where high radiation flux is possible.

The first experiments of a gas-puff Z-pinch were published in 1978 by a group at the University of California Irvine [11]. This was followed by a hollow shell gas-puff Z-pinch design intended to optimize radiation yields by allowing for higher implosion velocities just before

stagnation [12]. Numerous modifications and improvements to the first gas-puff systems have been made and studied over decades including multi-shell designs which enhanced implosion stability and implementing the De Laval nozzle geometry which increased axial uniformity [10].

1.2 Motivation

Because the entire Z-pinch process is carried out by the current in the plasma and its associated magnetic field, information about the temporal evolution and spatial distribution of these quantities is of paramount importance in the endeavour to study the nature and behavior of Z-pinch plasmas. A great deal of work studying Z-pinches relies on simplified models of plasma dynamics, and especially the magnetic field distribution which may not fully reflect the physical processes involved [13], [14], [15]. The basic model of the Z-pinch or "Bennett pinch" considers a cylindrical plasma whose thermal pressure is in equilibrium with the magnetic pressure, equivalently, the Lorentz force [1]. In addition, the classical picture of the Z-pinch results in a balance of energy between joule heating from the supplied current and energetic loss due to radiation [16, 17]. Experimental results have shown that these classical considerations do not represent real Z-pinches. In fact, it has been shown by quantifying thermal pressure and internal energy during the stagnation phase, only about 1/3 of the circuital current flows within the stagnated plasma column for Z-pinches optimized for K-shell radiation of dramatically different scales [14]. How the current distribution evolves during the implosion and stagnation phases and what factors influence its evolution remain unresolved questions in the field of plasma physics, even considering recent advancements in knowledge of the field [18], [19]. To understand the physical mechanisms involved and to produce reliable models of Z-pinch dynamics, experimental characterization of the evolution of the magnetic field is of paramount importance.

A promising new pulsed power architecture known as the linear transformer driver (LTD) provides high peak current, short rise time pulses while taking a fraction of the footprint required

by conventional pulsed power drivers [20]. While some LTD-based drivers have been used for gas puff implosions [21, 22, 23], the current delivery to the plasma load on such platforms has not been systematically studied. The high energy efficiency of LTDs results from a low machine impedance relative to the impedance of dynamic loads such as Z-pinches. This dissertation explores the efficacy and characteristics of current delivery to gas-puff implosions on a fast current-rise (τ_{peak} ¡ 200 ns) LTD. This work may inform design choices that will improve the efficacy of LTDs as plasma accelerators and provide experimental measurements of the current distribution in imploding plasmas which may improve modeling of gas-puff Z-pinches.

Measuring the azimuthal magnetic field, B_θ, in Z-pinches, and therefore current, is a notoriously difficult task. There are several techniques which rely on probing the plasma, each with advantages and limitations which are discussed below. Passive techniques which cannot perturb the plasma involve emission spectroscopy and are the primary tool used to study magnetic fields presented in this thesis.

1.3 Probing techniques to Measure Magnetic Field

1.3.1 Inductive B-dot Probes

Perhaps the most straight-forward technique to measure magnetic field is the use of inductive b-dot probes. These devices consist of a loop or loops of wire at the end of a coaxial cable. When a time varying magnetic flux is present within and perpendicular to the loop of wire, the voltage induced on the cable is read by an oscilloscope and the time varying magnetic field can be determined by applying Faraday's law of induction, $\nabla \times E = -\frac{\partial B}{\partial t}$ to the b-dot geometry, so that $V = -N\frac{d\phi}{dt}$ where V is the voltage read by the oscilloscope, N is the number of turns in the wire and ϕ is the magnetic flux enclosed by a b-dot loop, equivalently $B \cdot A$ where A is the area of a loop. Combining these expressions yields the following practical relationship between

the time integrated voltage signal and the magnetic field:

$$B = \frac{c}{\pi R^2} \int_0^{t'} v(t)dt \tag{1.1}$$

Where c is a calibration factor for the probe ($c \approx 1$ for well made probes with ideal behavior and orientation) and R is the radius of the wire loop. An illustration of a b-dot probe is shown below.

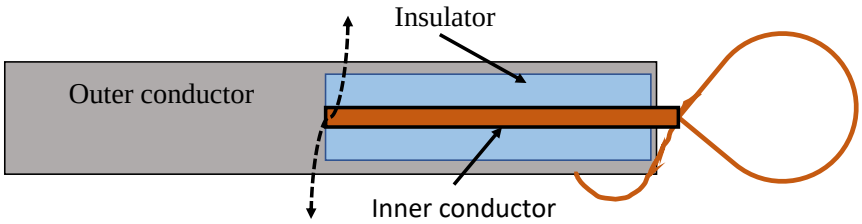

Figure 1.2: Illustration of a wire-loop b-dot in sectional view. The wire attached at the end of the coaxial cable is typically coated to prevent short-circuiting.

B-dot probes are commonly used in pulsed power systems to accurately measure driver current. B-dot probes have also been utilized in experiments to measure B within imploding wire-array plasmas [24, 25, 26]. However, the probes inherently perturb the plasma flow. To Improve spatial resolution, which requires using more probes, will further perturb the plasma of interest. The probes are also typically damaged during the experiment from the high levels of particle flux they encounter. This issue can be mitigated by protecting the probe with some material [25]. Inductive probes are well suited to experiments where plasma perturbation is not a concern, or measurements in regions where little or no plasma is expected [27, 28].

1.3.2 Faraday Rotation

The polarization of light passing through a material along a magnetic field will be rotated proportionally to the strength of the magnetic field interacting with the light. This phenomenon is known as the Faraday effect and can be exploited to measure magnetic fields in plasma, also

named ‘Faraday rotation’. When employed to measure B_θ in a Z-pinch, the technique involves sending a laser pulse through the plasma and then a polarizer before reaching the detector. The image is then compared to a reference image with no plasma (and no magnetic field) to determine the relative brightness and thus, the magnetic field. The effect of the magnetic field on the laser polarization is coupled to the line integrated density of the laser pulse through the plasma, so simultaneous measurement of the electron density is necessary for a quantitative determination of B_θ. This can be seen in expression of the polarization rotation angle of a light wave propagating through a plasma in the direction of $\hat{l}$ as a function of magnetic field **B** below from Hutchinson [29].

$$\alpha = \frac{e}{2m_e c}\int_L \frac{n_e}{n_c}\mathbf{B}\cdot\mathbf{dl} \tag{1.2}$$

Where the electron density, n_e varies along the chord path l and n_c is the plasma critical density, $n_c = \frac{\varepsilon_0 m_e}{e^2}\omega^2$ which is the number density at which electromagnetic waves of angular frequency ω dissipate due to shielding. Rewriting equation 1.2 in terms of the laser wavelength λ yields [30, 31]:

$$\alpha = 2.62\times 10^{-17}\lambda^2\int_L B n_e dl \tag{1.3}$$

Which now considers B as the projection of **B** along the path of integration.

Faraday rotation has been used to measure magnetic fields in gas-puff Z-pinches [32, 31]. Experiments at the University of California Irvine used it to measure the axial magnetic field when compressed by the imploding Z-pinch, reaching values of up to 1.6 MG [33]. Experiments at the University of Nevada, Reno examined the current distribution and evolution in wire array Z-pinches and X-pinches [30]. Later experiments studied the structure of the current distribution during stagnation and found that the majority of current was flowing in a trailing plasma, while a relatively low but significant portion of current flows within narrow ‘necks’ of the plasma column, which the authors attribute to an inhomogeneous implosion rather than MHD instabilities [34].

Requiring information of the line integrated density is just one limitation of the Faraday

rotation technique. In addition, if the probed plasma density is too high, ($n_e \sim n_c$), the laser cannot propagate and no magnetic field measurement is possible. For optical laser systems, the cutoff density is typically $n_e = 10^{19} cm^{-3}$. High density gradients also lead difficulties measuring either the density (necessary to measure B) or the magnetic field itself.

1.3.3 Proton Deflectometry

Recent advances in in high-intensity laser systems have led to the development of laser-produced particle beams [35]. While particle beams have been used to diagnose plasmas for years [36, 37, 38, 39], use of proton beams to measure magnetic fields in Z-pinches is a relatively unexplored development [40, 41]. This technique can result in high temporal resolution and spatial resolution of the measured magnetic field. The primary drawback for this method of determining magnetic fields in Z-pinches is the need for a high energy proton source in the same laboratory system as the pulsed-power Z-pinch driver. Few laboratories in the world are equipped with both a high-intensity short-pulse laser and a fast current driver coupled to the same experimental chamber. In addition, proton deflectometry is necessarily a path-integrated measurement, and local measurements of the magnetic field cannot be truly made. However, mapping of the magnetic field is possible using images of deflected protons using sophisticated computer codes [42].

The operating principle of proton deflectometry is the path-integrated Lorentz force resulting in an angle of deflection [43]:

$$sin(a) = \frac{q}{\sqrt{2mE}} \int \mathbf{B} \times d\mathbf{L} \tag{1.4}$$

Where E is the kinetic energy of the protons, q is the proton charge, m is the proton mass. The cross product indicates that the protons are always deflected in a direction perpendicular to both the proton momentum and magnetic field. One method to apply this principle experimentally to a

Z-pinch is to simply place a detector sensitive to high-energy protons but shielded from other radiation (x-rays) past the plasma. The spatially dependent response on the detector along with the intrinsic divergence of the proton beam and the experimental geometry indicates the degree which the beam protons were deflected by the magnetic field. The high energy proton beams produced by the so-called target normal sheath acceleration mechanism are not strictly mono energetic. Because the particle deflection by the Lorentz force depends on both the strength of the magnetic field *and* the perpendicular velocity, determining the magnetic field based on particle deflection requires knowledge of the particle energy spectrum. To deal with this experimentally, the detector is composed of multiple layers of radiochromic film (RCF). This way, filters between layers can be chosen in such a way that low energy protons will be stopped in the shallow layers of the detector while high energy protons will pass through and interact with a deeper layer.

Another interesting method for ion deflectometry uses high energy protons generated by high electric fields present during disruption of the Z-pinch plasma column. In this scenario, the ions are accelerated axially and deflected by the azimuthal magnetic field. Placing a wire mesh in the path of the high-energy protons results in a distorted image of the wire mesh due to the magnetic 'lensing' [44]. The main advantage to this approach is that the high energy ions pass near the central axis of the experiment, allowing measurements of B at the most extreme conditions. While this technique has made experimental mapping of the magnetic field possible, it is limited to the time period when instability induced disruption occurs and cannot be used to study the evolution of the magnetic field distribution. Furthermore, stable implosions and Z-pinches cannot be investigated using this method as the lack of plasma disruption will lead to no significant high-energy ion source.

1.4 Non-invasive Techniques: Zeeman Spectroscopy

1.4.1 The Zeeman Effect

Atomic energy levels are split when in the presence of a magnetic field, this phenomenon is known as the Zeeman effect. When photons are emitted by electron transitions to and from the split energy levels, the resulting emission spectrum contains a split pattern of lines instead of the single line observed with no magnetic field. The theoretical background for atomic processes described in this thesis are generally referenced to the text by Kunze [45], the text by Degl'innocenti & Landolfi [46], the text by Sobelman [47] and the handbook by Drake [48]. In the presence of a magnetic field, the so called 'M-degeneracy' of a given energy level is broken into multiple levels for each value of the magnetic quantum number 'M' (which corresponds to the orientation of the atomic orbitals). The energy associated with this interaction of the atomic orbital and the magnetic field is given by the following expression below.

$$\Delta E = g\mu_B B \tag{1.5}$$

where B is the magnetic field strength, μ_B is the Bohr magneton ($\mu_B = \not{e}\hbar/2m_e$), and g_L is the g-factor which depends on the type of spin-orbital coupling to the magnetic field.

An electronic state can be fully defined by a set of atomic numbers. The principal atomic number, **N**, quantifies the energy of the shell. The secondary or azimuthal quantum number, **l** defines the shape of the atomic orbital and the subshell and takes on integer values from 0 to **n** -2. The magnetic quantum number **m** specifies the orientation of the atomic orbital in space which takes on values from -**l** to **l**. The spin quantum number **s** describes the spin of the electron and is either +1/2 or -1/2.

Similarly, and perhaps confusingly, atomic energy levels are described using corresponding quantum numbers. The principal quantum number **n** still describes the overall energy level

and takes integer values. The total angular momentum is **L** and can be all values of the sum of individual azimuthal numbers, known as the 'term'. Now the magnetic quantum number for atomic levels is **M** which takes on values from -**J** to **J**.

For weak magnetic fields, where the strength of the external magnetic field sufficiently small so that the spin-orbital coupling remains much stronger than the magnetic interaction, the "Landé" g-factor is valid and given by the expression below:

$$g_L = 1 + \frac{J(J+1) - L(L+1) + S(S+1)}{2J(J+1)} \tag{1.6}$$

Where L is the orbital atomic number, J is the total angular momentum (the vector sum of spin and orbital angular momenta), and S is the absolute value of the sum of electron spin. An example transition under the Zeeman effect is shown in the figure below. Both levels involved in a particular transition are shown in figure 1.3, $3p^2S_{3/2}$ being the upper level and $3s^2S_{1/2}$ being the lower level. The level associated with each value of **M** is also shown in figure 1.3 along with each of the possible transitions (where $\Delta\mathbf{M} = \pm 1 \; or \; 0$).

The transitions where $\Delta\mathbf{M} = \pm 1$ are known as 'σ' transitions, while transitions where $\Delta\mathbf{M} = 0$ are known as 'π' transitions. The wavelength shift from the unperturbed transition (B = 0) can be determined using the energy shift of the upper and lower states given by equation 1.5. The resulting splitting observed from the transition as a function of magnetic field is given in the equation below in practical units.

$$\Delta\lambda = 4.669 \times \; 10^{-9}(M_q g_{Lq} \; - \; M_p g_{Lp})\lambda_0^2 B \tag{1.7}$$

Where $\Delta\lambda$ and λ_0 are in Å, and B is in Tesla (T). An example of the theoretical splitting observed for the $3s^2S_{1/2} - 3p^2P_{3/2}$ transition is shown in the figure below which includes both σ and π components of the transition although an experimental result will not necessarily observe both *sigma* and *pi* components. Furthermore, the individual transitions displayed in figure 1.4 are

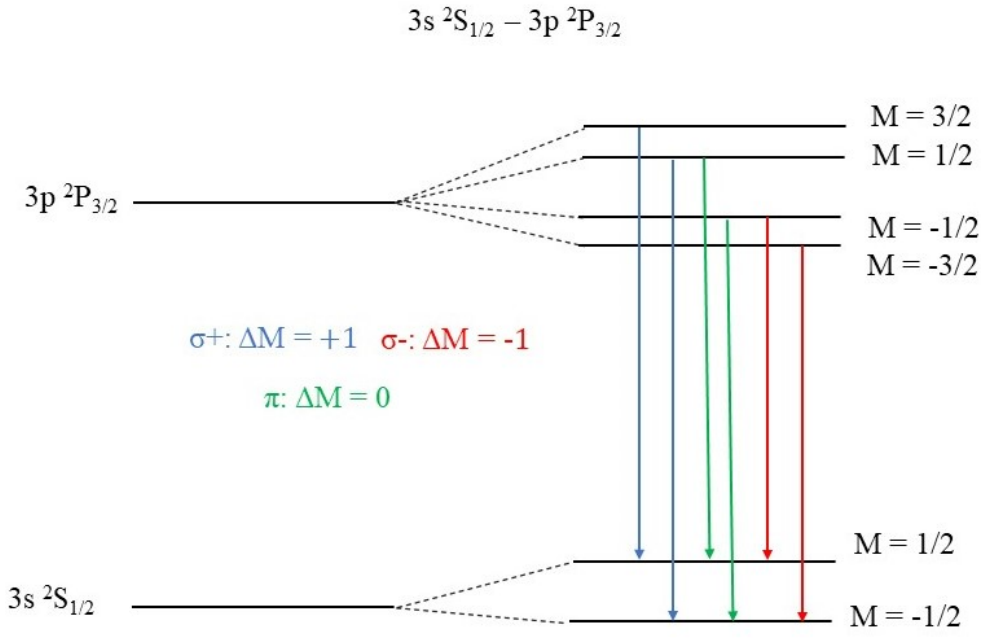

Figure 1.3: Split energy levels in the presence of a magnetic field for the $3s^2S_{1/2} - 3p^2P_{3/2}$ transition. Shown are all levels with their corresponding values of M as well as the possible transitions by type.

typically not resolved in Z-pinch experiments and the relative intensity of each transition will result in a broadened lineshape which is skewed toward the more intense components. The theoretical relative intensities can be calculated with the Wigner 3-j symbols shown in equation 1.8 [46, 49]. For practical uses in analysis of experimental data, a weighted average of the theoretical line splitting can be used.

$$I = \begin{pmatrix} J & 1 & J' \\ -M & M - M' & M' \end{pmatrix}^2 \tag{1.8}$$

In many experimental situations, the local magnetic field strength can be directly measured by simply observing a pattern of split emission lines and calculating B from the peak separation and equation 1.5. This is the simplest and most straightforward method to measure the magnetic field of a sample volume using emission spectroscopy. Various plasma experiments have utilized

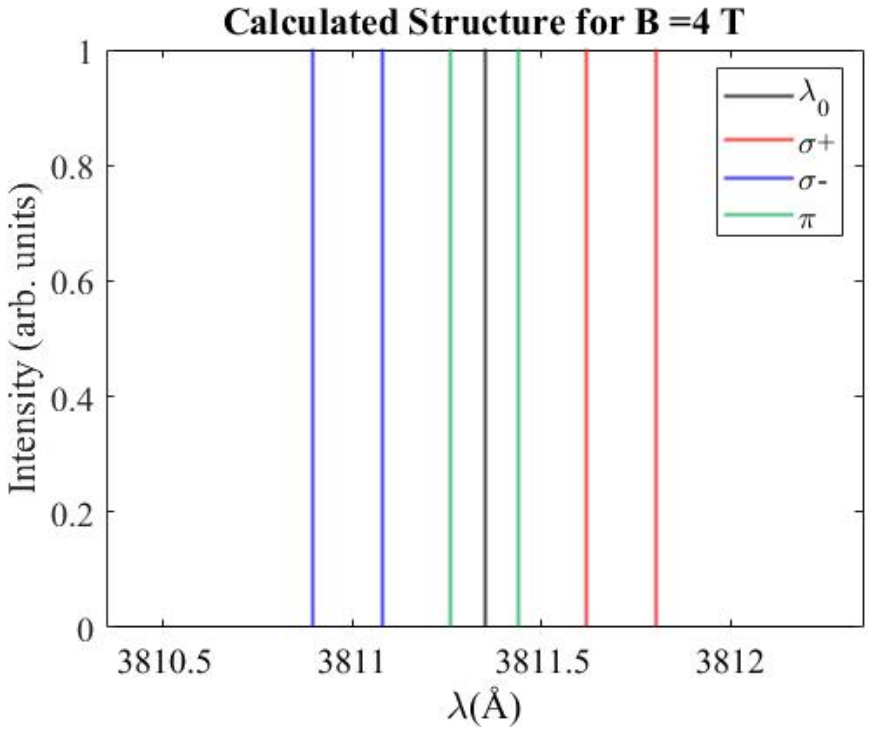

Figure 1.4: Theoretical Zeeman-splitting for σ and π components in the presence of a magnetic field for the $3s^2S_{1/2} - 3p^2P_{3/2}$ transition.

this technique for decades [50], [51], [52], [53], [54], [55], [56]. However, Zeeman-splitting spectroscopy suffers from several limitations. The most pervasive difficulty encountered in Zeeman-splitting spectroscopy for Z-pinches is line broadening due to physical effects unrelated to the magnetic field.

1.4.2 Line-Broadening

Several mechanisms are involved in producing the observed line shape of a spectral line. First, no spectral line can possibly exhibit a true 'delta' function in the frequency domain since the states exist for a finite amount of time. This is known as 'natural broadening'. In a plasma, emitters (atoms & ions) exhibit motion in three-dimensional space associated with their kinetic energy, or temperature in aggregate terms. The sum of Doppler shifts for all emitters within the collection volume of the spectroscopic system leads to a line shape which exhibits

'thermal-Doppler broadening'. Because this is a thermal effect, a Gaussian profile (shown in eq. 1.9 by I_G where a is the full-width at half maximum and λ_0 is the central wavelength) is well suited to model a spectral line dominated by thermal broadening.

$$I_G(\lambda, a) = \sqrt{\frac{4ln2}{\pi a^2}} e^{-4ln2(\frac{\lambda-\lambda_0}{a})^2} \tag{1.9}$$

Limitations of instrumental resolution also contribute to the experimentally observed line shapes by 'instrumental broadening'. This is typically a result of collection from a finite spatial window (or slit) with which light is dispersed by the spectral analyzer of the instrument. A small slit width and small spatial scale of the analyzer's periodic structure can reduce instrumental broadening. Perhaps most important for Z-pinch plasmas is 'Stark broadening'. The Stark effect can be understood as the electric field analogue of the Zeeman effect. In the presence of a macroscopic electric field, energy levels are perturbed in such a way that causes spectral lines to split and shift in proportion to the magnitude and direction of the electric field. For plasmas, a macroscopic electric field is generally implausible due to Debye shielding. However, on the spatial scale of each emitter, the presence of nearby charged particles will cause each emission event to be influenced by the Stark effect associated with the resultant local electric field. This phenomenon will occur for each emitter at each emission event with no directional preference. This ultimately results in line broadening known as the 'Stark effect' and is proportional to the strength of the local electric field for each emitter, which is proportional to the electron density n_e. The favored profile to model a line shape dominated by Stark-broadening is the Lorentz profile which is shown as I_L in equation 1.9 below where b is the full width at half maximum and λ_0 is the central wavelength.

$$I_L(\lambda, b) = \frac{b}{2\pi((\lambda-\lambda_0)^2 - (b/2)^2)} \tag{1.10}$$

In most Z-pinches, densities are sufficiently high so that the effects of the magnetic field on the line emission are undetectable due to Stark broadening. For example a number density

of $10^{18} cm^{-3}$ results in a Lorentzian full width half maximum of 5 Å for a C IV 3s-3p transition [57, 58]. Simultaneously accounting for thermal-Doppler, instrumental and Stark broadening in a single line shape profile requires convolution of Gaussian and Lorentz profiles. The combined line-shape is called a 'Voigt profile' and is given by I_V in equation 1.11 where c is the wavelength normalized to the half-width of the Gaussian profile ($c = \frac{\lambda-\lambda_0}{a} 2\sqrt{ln2}$) and $d = \frac{b}{a}\sqrt{ln2}$.

$$I_V(c,d) = \frac{d}{\pi} \int_{-\infty}^{\infty} \frac{e^{-t^2}}{d^2 + (c-t)^2} dt \tag{1.11}$$

1.4.3 Atomic Multiplet Technique

One promising method to determine magnetic fields in high-density plasmas involves line shape analysis of components of an atomic multiplet. The technique was recently developed by Stambulchik and collaborators at the Weizmann Institute of Science (WIS) [59] and was followed by an experimental proof of concept [60]. The central premise on which this technique relies is that two transition components of an atomic multiplet in close spectral proximity to one another will undergo nearly identical Stark, thermal-Doppler, and instrumental broadening while the Zeeman effect will be consistently and predictably different between the two. The fact that this is true regardless of the direction of the magnetic field with respect to the observed line of sight means that this technique can be used to measure B when the direction of B is unknown or 'quasi-isotropic' on the length scale of observation. The following figure from [59] displays the principle in plain terms: With minimal broadening mechanisms at play, the Zeeman splitting pattern for both π and σ components is observable in the spectra as shown in figure 1.5 a. Due to the weighting of the individual components, the ${}^2S_{1/2} - {}^2P_{1/2}$ transition is always wider than the ${}^2S_{1/2} - {}^2P_{3/2}$ transition whether σ, π or an arbitrary combination of the two sets of components are observed. This fact is still observable in the overall line-shape of a broadened line, as seen in figure 1.5 b.

Because this technique requires experimental observation of two components of a multiplet

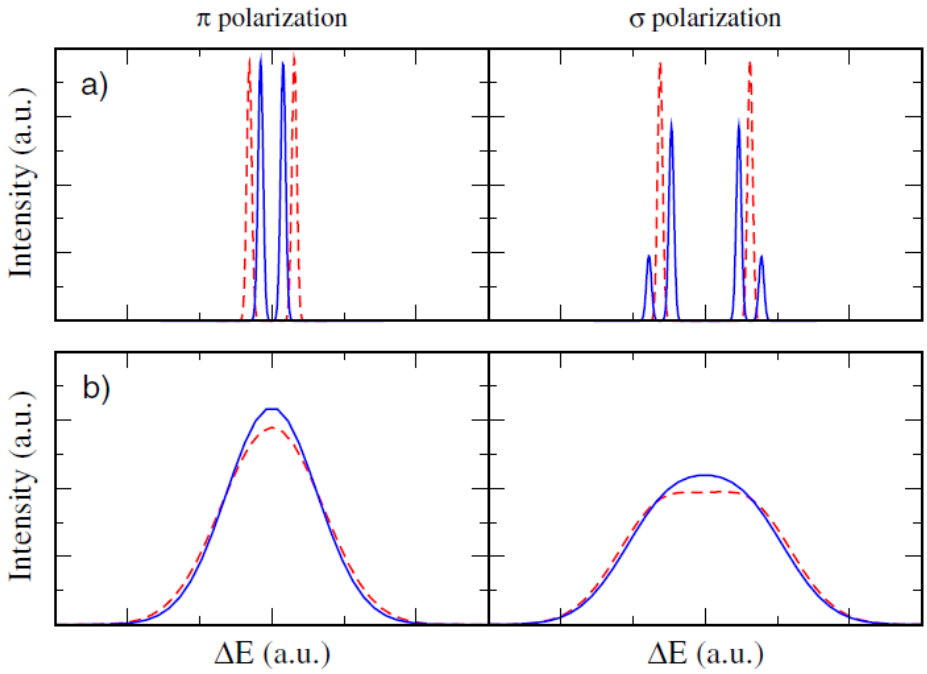

Figure 1.5: Calculated line shapes for ${}^2S_{1/2} - {}^2P_{3/2}$ (solid blue curves) and ${}^2S_{1/2} - {}^2P_{1/2}$ (dashed red curves) π transitions (left) and σ transitions (right). Minimal Gaussian blurring was applied to (a) with greater blurring applied to (b). Figure from Stambulchik et al. [59].

simultaneously, choosing transitions to attempt measurements with is restrictive. It is important that the multiplet components are in close enough spectral proximity to observe on the same detector (to ensure the same broadening on both lines) but far enough that they remain resolved. Experiments using an Al III doublet successfully measured magnetic fields near $12 \pm 1T$ using this technique [60]. The experiment consisted of aluminum plasma produced by laser ablation of an Al rod which also acted as a circuit load in the anode-cathode gap of the pulsed power driver, producing the magnetic field to be measured. To date, employment of this technique on Z-pinches or other applications has not been published in the literature.

1.4.4 Polarization-based Spectroscopy

Since Stark broadening often smears out the Zeeman-splitting pattern such that the magnetic field strength cannot be determined by simple emission spectroscopy, more advanced

techniques have are required to measure B in Stark-dominated conditions. Some methods exploit the polarized characteristics of the Zeeman effect. Emission viewed perpendicular to the global magnetic field will contain both σ and π components of a given transition. Along the line of site perpendicular to B, the π components will be linearly polarized along B while the σ components will be linearly polarized orthogonal to B. Exploiting this fact allows for measurement of B in Stark-dominated conditions. This technique will be referred to as the 'polarization perpendicular' technique in this thesis. Using this technique requires the use of a polarizing beamsplitter which separates the two orthogonal components onto two separate spectrometers or onto two regions of the detector on the same spectrometer. The magnetic field is finally determined by comparing the difference in line-widths of the two components of the same spectral line obtained from the spatial region at the same times. As seen in figure 1.4, the σ components exhibit a larger degree of splitting than the π components. Experiments carried out at the Weizmann Institute of Science (WIS) used the polarization perpendicular technique for a carbon dioxide gas-puff implosion [61]. The arrangement was such that emission was viewed parallel to the Z-axis, perpendicular to the $x-y$ or azimuthal plane, where $\mathbf{B} = B_\theta$. This allowed for measurements at multiple radial positions, always integrating in the z-direction. These experiments found that the entire discharge current was flowing within the outer plasma radius. This was determined by applying Ampere's law (equation 1.12) using the total circuital current I as measured by the Rogowski coil at the time of the diagnostic window and r_{spect} at the radial position where the spectroscopic data was used.

$$B_\theta = \mu_0 I / 2\pi r_{spect} \tag{1.12}$$

Using measurements of B_θ from a few radial positions as constraints, numerically solving the magnetic diffusion equation allowed for determination of the plasma conductivity which was found to coincide with the Spitzer value. This work provided substantial insight into the current distribution of gas-puff implosions but left some unanswered questions remaining and some improvements still desired. The high degree of axial non uniformity proved problematic, since

measurements made in this experiment were axially integrated. This made only early-time, large radius measurements possible, with 530 ns being the latest measured time (90 ns prior to stagnation at 620 ns).

Emission viewed parallel to the external magnetic field will contain only the σ components of line transitions and no π components. Additionally, the $\sigma+$ and $\sigma-$ components will be circularly polarized with opposite handedness. With proper use of polarization optics and knowledge of the direction of B within the observed volume in an experimental setting, the $\sigma+$ and $\sigma-$ components can be separated from one another, allowing for determination of magnetic fields even in Stark-dominated, high density plasmas. In this thesis, this technique will be referred to as the 'polarization-parallel' technique. A schematic of the experimental arrangement for the polarization technique to measure B_θ is shown in figure 1.6.

The most common utilization of the polarization parallel technique in a Z-pinch experiment involves imaging the plasma in the visible or UV range onto a fiber array which is coupled to the spectrometer. Use of a fiber array allows for a relatively simple alignment procedure and flexibility. Following the arrangement shown in figure 1.6, light emitted from the plasma is collimated by an lens placed at its focal length from the center of the plasma column. The collimated light is sent through a $\lambda/4$ waveplate which converts any purely circularly polarized light into linearly polarized light. Next, the light is sent through the polarizing beamsplitter cube (PBSC) which separates orthogonal polarized light into two paths. From each output path of the PBSC, a lens creates an image of the collimated light at the 'launch' of the fiber array. The exit of the fiber array is then imaged at the entrance slit of a high-resolution imaging spectrometer. Although emission may be collected from multiple chords of the plasma column simultaneously, only data collected from the outer edge of emission is valid for this technique since a line of sight parallel to the magnetic field is required. Selecting data from the outer edge of emission ensures the emission is parallel to B_θ at the point of emission; data collected from other chords includes emission with a component perpendicular to B_θ which is not circularly polarized.

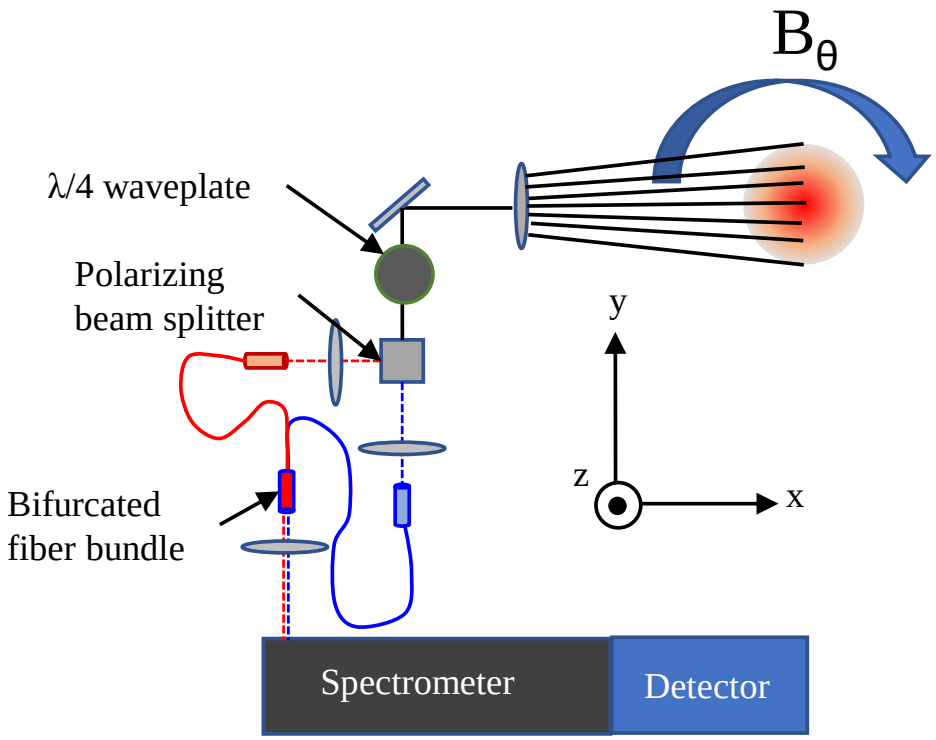

Figure 1.6: Diagram of the experimental arrangement for the polarization parallel technique applied to measuring B_θ in a cylindrical plasma. The arrangement shown images the plasma onto a fiber array after the light is sent through the λ/4 waveplate and polarizing beamsplitter cube.

In Z-pinches, the polarization parallel technique was developed at the University of Washington for Carbon Dioxide gas-puffs [62]. The technique has since been used for various studies at the Weizmann Institute of Science (WIS) to measure the azimuthal magnetic field in imploding Z-pinches [63], [64], [65]. Experiments performed at the WIS using the polarization parallel technique found a striking effect of an external axial magnetic field on the current distribution of imploding argon gas-puffs [65]. With no axial magnetic field, the spectroscopically measured values of B_θ at the outer edge of emission indicated that all of the driver current was flowing within the outer plasma radius, also determined using Ampere's law (equation 1.12 and the machine current measured by a B-dot probe. However, when the initial axial magnetic field (B_{z0}) was applied, it was found that only a fraction of the current was flowing at r_{spect} and this

discrepancy became more pronounced with greater values of B_{z0}. This trend is displayed in figure 1.7 below. The authors also observed that a low density plasma was present in a region peripheral to the bulk imploding plasma, made evident by low intensity carbon emission lines present in this peripheral region. The authors postulated that the axial magnetic field resulted in a force free configuration of low density peripheral plasma, allowing it to carry current while not imploding with the bulk plasma. Chapters four and six in this thesis will further discuss these results using more experimental results obtained on both the same experimental system as WIS and a separate system used at UC San Diego.

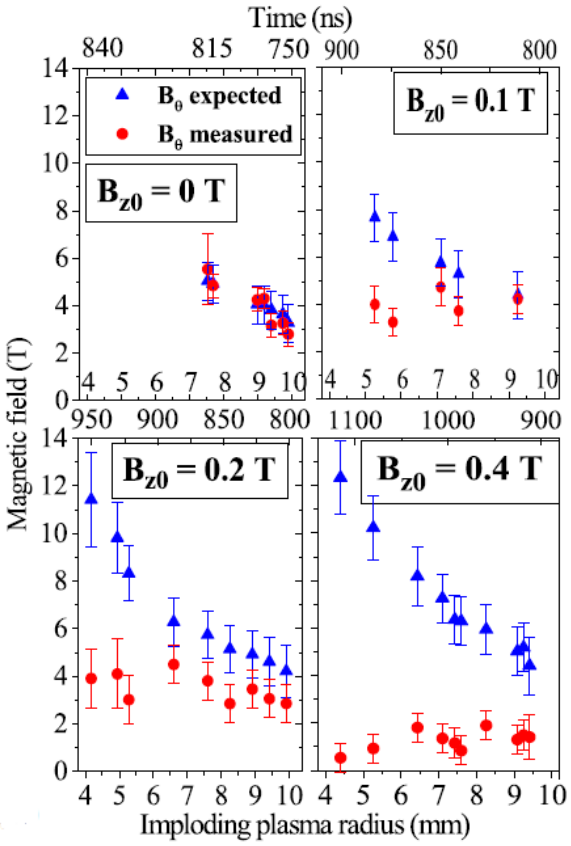

Figure 1.7: Measured and expected values of B_θ for various values of B_{z0} as a function of imploding plasma radius. figure from Mikitchuk et al. [65]

Another study carried out by the WIS compared experimental measurements of the radial distribution of B_θ to results obtained with two-dimensional MHD simulations of the experiment

[66]. These experimental results were unique in that they provided a measured radial distribution of B_θ up to and during the stagnation phase of the Z-pinch. Contrary to the work discussed above, no axial magnetic field was introduced in these experiments. While the total circuital current was found to flow within the outer plasma radius in these experiments, the nature of the radial dependence of B_θ did not follow predictions made by the MHD simulations, the results are shown in figure 1.8 below.

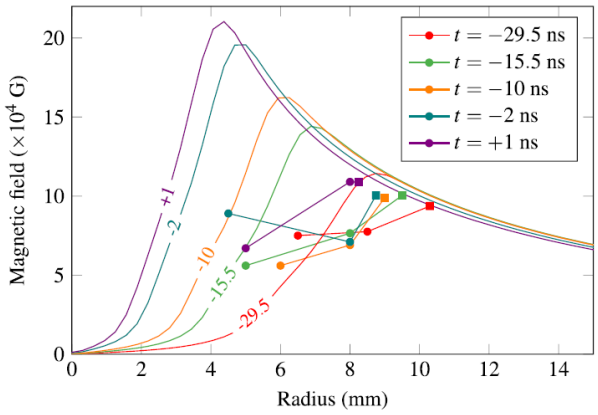

Figure 1.8: Measured and simulated radial profiles of B_θ for oxygen gas-puff implosions at WIS. Measured profiles are displayed by the straight lines and points. Radial profiles calculated in MACH2 are shown by the solid curves figure from Rosenzweig et al. [66]

In general, the measured radial profiles of B_θ did not follow the steep shapes predicted by MHD. This meant that near stagnation, the magnetic field did not follow a diffusive drop-off into the plasma, as was observed during the early implosions reported in the literature [61]. In addition, non-monotonic dependence of B_θ on r was observed at multiple instances in these experiments. The authors suggest this may be due to flaring or strong axial density gradients present in the imploding plasma. Chapters four through six in this thesis will cover experiments similar to those presented in [66], namely, observing the behavior or the spatial distribution of B_θ with and without axial magnetic fields and on drivers with varied timescales and initial conditions.

1.5 Outline of the Thesis

Chapter two covers the relevant theoretical models of plasmas used to describe and predict Z-pinch behavior. First, the most simple and restrictive model of the Z-pinch implosion is discussed, followed by increasingly more general MHD models. The importance and relevance of the physical processes that necessitate each MHD description is discussed as well. This is followed by a discussion of the instabilities present in Z-pinch implosions and how they are mitigated. Finally, some theoretical concepts specific to gas-puff experiments are considered, namely the breakdown phase and the effects of axial density gradients.

Chapter three discusses the experimental systems used for the studies discussed in the subsequent chapters. First, the characteristics pulsed power driver used at the WIS is covered followed by the details of the diagnostic arrangement used for the experiments there. Next, the design and characteristics of the CESZAR linear transformer driver are discussed including the machine diagnostics and calibrations as well as the primary subsystems of the CESZAR lab including the axial magnetic field system. The details of the CESZAR experimental arrangement and diagnostics are discussed. Lastly the Design and experimental characterization of the gas-injector used for the CESZAR experiments is covered.

Chapter four covers the results from oxygen gas-puff experiments conducted at the Weizmann Institute of Science. First, the force free configuration of low density peripheral plasma is discussed as well as the conditions associated with this phenomenon. Next, the methods used by these experiment to reduce contaminants associated with low density peripheral plasma are discussed. The MHD model code used to model these experiments is described followed by experimental results detailing the dynamics and stability of the implosions. Next, the measured radial distributions of B_θ in discharges with and without $B_z 0$ is presented as well as measurements of B_z at $r = 0$. Finally, implications of magnetic stability on the radial current profile are discussed.

Chapter five examines measurements of plasma-current coupling on two drivers of vastly

different current-rise times. Magnetic field measurements from gas-puff experiments using the driver at WIS and the CESZAR driver at UCSD are presented. Discrepancies of plasma-current coupling between the two drivers are discussed and potential causes are explored.

Chapter six presents experimental results which examine the role of various sets of initial conditions on the plasma current coupling in liner-on-target gas-puff experiments on the CESZAR driver. First, the liner-on-target configuration is described. Second, the various initial conditions explored in these experiments and subsequent results are discussed including the electrode design, the gas-puff parameters, and the axial magnetic field strength. Finally, MHD simulations results carried out in HYDRA are presented in conjunction with simulation results.

The concluding chapter summarizes the primary results covered in this thesis and their implications for Z-pinch research within the field of plasma physics.

Chapter 2

Theoretical Models of Z-Pinch Plasma Dynamics

2.1 Magnetohydrodynamic Theory

Magnetohydrodynamcis (MHD) is a framework which models the behavior of electrically conductive fluids considering both mechanical and magnetic forces and stresses. Plasmas, being ionized gases and therefore electrically conductive, can often be accurately described with an MHD framework. While MHD is not the most general theoretical framework for studying plasma dynamics, if applied under valid circumstances, MHD theory is a favored modeling approach over more computationally expensive models such as kinetic theory or particle-in-cell approaches. The description of the MHD model discussed in this thesis is generally cited to texts by Hans Goebloed [67], Francis Chen [68], Goldston & Rutherford [69], and Paul Bellan [70].

Because MHD is a fluid framework, the criteria of validity for modeling plasmas using MHD (instead of a more general framework) are primarily spatial and temporal scales whereby small-scale interactions of individual particles are not important. One important criterion for the validity of the MHD approach involves particle collisionality; ions (and, necessarily, electrons)

must undergo many collisions within the MHD timestep, τ_M, such that $\tau_M >> \tau_i$ where τ_i is the mean time between ion collisions. Alternatively, the collisionality assumption can be quantified by length scales. In this case, the MHD validity criterion requires much smaller collisional mean free path, λ_{MFP}, than the MHD length scale, d_M so that $\frac{\lambda_{MFP}}{d_M} = \kappa << 1$ where κ is known as the Knudsen number. This criterion is identical to the 'continuum approximation' in the area of fluid mechanics which assumes a high degree of collisionality [71].

Additionally, treating plasma as a single fluid must assume large enough length and time scales such that the effects of electric and magnetic fields at small ranges and short time scales are essentially averaged over. Quantitatively, this means that $d_M >> r_L$ and $\tau_M \sim d_M/v_A >> 1/\omega_i$ where $r_{Li} = \frac{mv_\perp}{qB}$ is the Larmor radius of ions, $v_A = \frac{B}{\sqrt{\mu_0 \rho}}$ is the Alfvén velocity and $\omega_i = \frac{qB}{m_i}$ is the cyclotron frequency of ions.

The MHD framework relies on solutions to the following system of equations which include the laws of classic electricity & magnetism in addition to laws for material and momentum conservation [69], [67]. The equations are shown below, vector quantities are represented with bold face symbols. The mass continuity equation:

$$\frac{\partial \rho}{\partial t} + \nabla \cdot \rho \mathbf{v} = 0 \tag{2.1}$$

The equation of motion:

$$\rho \left(\frac{\partial \mathbf{v}}{\partial t} + \mathbf{v} \cdot \nabla \mathbf{v} \right) = \mathbf{J} \times \mathbf{B} - \nabla p \tag{2.2}$$

Conservation of charge:

$$\frac{\partial \sigma}{\partial t} + \nabla \cdot \mathbf{J} = 0 \tag{2.3}$$

Faraday's law of induction:

$$\nabla \times \mathbf{E} = -\frac{\partial \mathbf{B}}{\partial t} \tag{2.4}$$

Ampere's law:

$$\nabla \times \mathbf{B} = \mu_0 \mathbf{J} \tag{2.5}$$

Gauss' law for magnetism:

$$\nabla \cdot \mathbf{B} = 0 \tag{2.6}$$

Ohm's law

$$\mathbf{E} + \mathbf{v} \times \mathbf{B} = \eta \mathbf{J} \tag{2.7}$$

Ohm's law accounts for the interaction of electric and magnetic fields with the conductive property of the plasma.

Some important relationships relevant to Z-pinches can be studied analytically with some of these equations. The first theoretical conception of the Z-pinch introduced by Bennett [1] considered a cylindrical plasma whose thermal pressure was balanced by magnetic pressure generated by an axial current. Considering equation 2.2 under static conditions ($\frac{d}{dt} = 0$) yields an equilibrium between the thermal pressure gradient and the Lorentz force:

$$\nabla p = \mathbf{J} \times \mathbf{B} \tag{2.8}$$

In this problem, current is only in the z direction ($\mathbf{J} = J_z$) and all values are only a function of radius, so that $\nabla p = \frac{\partial p}{\partial r}$. Applying equation 2.5 to the cylindrical conductive plasma yields $B_\theta = \frac{\mu_0 I(r)}{2\pi r}$. Using these expressions to simplify equation 2.8 and integrating along r to the plasma-vacuum boundary at R yields the following expression:

$$2\pi \int_0^R r p(r) dr = \frac{\mu_0 I^2(R)}{8\pi} \tag{2.9}$$

The thermal pressure can be expressed using the ideal gas law considering the contributions of both ions and electrons and assuming thermal equilibrium between both ($T_i = T_e = T$) so that $p = (Z+1)n_i k_b T$. The line-integrated density of the cylindrical plasma can be defined as $2\pi \int_0^R rn(r)dr$. Rewriting the left hand side of equation 2.9 using the ideal gas law and the line integrated density yields the Bennett relation:

$$I^2 = \frac{8\pi}{\mu_0}(Z+1)k_B NT \tag{2.10}$$

This relationship is significant as it expresses quantitatively how a hot plasma may be confined in a cylindrical geometry with just an axial current. Unfortunately, this equilibrium situation suffers from instabilities which are discussed in section 2.3 Another useful expression can be obtained by combining equations 2.5, 2.7, and 2.4, sometimes called the magnetic transport equation:

$$\frac{\partial \mathbf{B}}{\partial t} = \nabla \times (\mathbf{v} \times \mathbf{B}) + \frac{\eta}{\mu_0}\nabla^2 \mathbf{B} \tag{2.11}$$

Using a physical length scale δ and velocity v_0 in equation 2.11 and comparing scale factors on the right hand side reveals a non-dimensional parameter known as the magnetic Reynolds number, R_m.

$$R_m = \frac{\mu_0 v_0 \delta}{\eta} \tag{2.12}$$

The magnetic Reynolds number gets its name from its analogous nature to the Reynolds number ubiquitous in fluid mechanics which compares advective transport to diffusive transport of momentum seen in the Navier-Stokes equations. In the case of transport of magnetic field, or induction, the electrical resistivity of the medium (plasma) scales the diffusive transport, instead of viscosity.

2.1.1 Hall MHD

The most general MHD model makes no simplifying assumption about the MHD scale length and ion Larmor radius, resulting in additional terms to be included in Ohm's law. Shown below is the most general expression for Ohm's law, which is often called 'extended MHD' since the terms on the right hand side are sometimes neglected, most often the Hall term ($\frac{\mathbf{J}\times\mathbf{B}}{en}$) and the electron pressure gradient. Equation 2.13 shows that the Hall term is more important for low density situations. It is necessary when studying physical processes simultaneously at multiple scale levels. In gas-puff Z-pinches, Hall MHD may describe the relevant processes involved in axial magnetic flux amplification [72].

$$\mathbf{E}+\mathbf{v}\times\mathbf{B}=\eta\mathbf{J}+\frac{1}{en}(\mathbf{J}\times\mathbf{B}-\nabla p_e) \tag{2.13}$$

2.1.2 Resistive MHD

The MHD models used in this thesis primarily rely on resistive MHD, which is accurately represented by equation 2.11. Resistive models are required to study the spatial distribution of magnetic fields within the plasma to compare with experimental measurements. An important phenomenon relevant to Z-pinches is known as the skin effect which can be examined analytically. Applying equations 2.5, 2.4, and 2.7 and neglecting any motion $\mathbf{v}=0$ to an infinite rectangular system where $\mathbf{J}=J_z$ so that $\mathbf{B}=B_x$, a diffusion-type equation for current density is attained:

$$\frac{\eta}{\mu_0}\frac{\partial^2 J_z}{\partial y^2}=\frac{\partial J_z}{\partial t} \tag{2.14}$$

One solution to equation 2.14 is a dampened sinusoidal function with the form $J_z=J_0e^{\frac{-y}{\delta}}sin(\omega t+\frac{y}{\delta})$. Applying this solution to 2.14 reveals the 'skin depth' to be $\delta=\sqrt{\frac{2\eta}{\mu_0\omega}}$. In this simple picture, the current drops off exponentially into the conductor on a length scale associated with the material resistivity and the frequency of the changing current. This expression can be a useful

tool when applied to Z-pinches, since the frequency, ω, can be estimated with the pulsed power RLC frequency. The resistivity, η, can also be estimated based on the plasma parameters.

The most simple and common approach to estimating plasma resistivity is by considering coulomb collisions in a hot plasma following the discussion of collisions in Chen [68]. For this, the momentum exchange between ions and electrons is related to the collision frequency (ν_{ei}), density, ion mass m and relative velocities $\mathbf{P}_{ei} = mn(\mathbf{v}_i - \mathbf{v}_e)\nu_{ei}$. Likewise, the same momentum exchange due to the coulomb force is proportional to both the ion and electron charge densities (assuming $n_i = n_e$) and relative velocities using η as a constant of proportionality $\mathbf{P}_{ei} = \eta e^2 n^2(\mathbf{v}_i - \mathbf{v}_e)$. The collision frequency can be rewritten:

$$\nu_{ei} = \eta \frac{ne^2}{m} \tag{2.15}$$

Writing the momentum change as a product of the coulomb force and the impact duration yields:

$$\Delta mv = \frac{e^2}{4\pi\varepsilon_0 r_0 v} \tag{2.16}$$

Where r_0 is the 'impact parameter' of the collision, or length scale at which the particles will pass one another assuming a large angle of incidence and ε_0 is the permittivity of free space. Considering the collision frequency between ions and electrons is a product of the particle density, velocity and collisional cross section, $\sigma = \pi r_0^2$, equation 2.15, can express the constant of proportionality η in terms of velocity:

$$\eta = \frac{e^2}{16\pi\varepsilon_0^2 mv^3} \tag{2.17}$$

Considering that the motion associated with v as thermal, equation 2.17 can be rewritten in terms of the plasma temperature since $k_b T = mv^2$:

$$\eta = \frac{e^2 m^{1/2}}{16\pi\varepsilon_0^2 (k_B T)^{\frac{3}{2}}} ln\Lambda \tag{2.18}$$

This formulation of resistivity is known as Spitzer resistivity which includes the impact parameter $ln\Lambda$ to account for small angle collisions where $\Lambda = 12\pi n\lambda_D^3$ and λ_D is the Debye length.

Considering the state variables of ions and electrons separately is useful to improving the resistive MHD model without the need for an entire set of conservation equations for both species. This is often done in computer MHD models, such as the Lawrence Livermore National Laboratory (LLNL) code HYDRA used for comparison with experimental results in this thesis [73].

2.1.3 Ideal MHD

Ideal magnetohydrodynamics simplifies the fluid approach to plasma by assuming that the diffusive effects of plasma resistivity on the transport of magnetic flux are negligible. This assumption requires that $R_m >> 1$ and is sometimes referred to as 'frozen-flux theorem' since magnetic flux is only and always transported advectively with the plasma in this model. Under this approximation, Ohm's law becomes:

$$\mathbf{E} + \mathbf{v} \times \mathbf{B} = 0 \tag{2.19}$$

Therefore, the magnetic transport equation is reduced to the following:

$$\frac{\partial \mathbf{B}}{\partial t} = \nabla \times (\mathbf{v} \times \mathbf{B}) \tag{2.20}$$

A value for R_m estimated for implosions studied in this thesis can be obtained using a typical implosion velocity of $v_0 = 100km/s$, the initial gas diameter for a scale length of $\delta = 3cm$, and resistivity of $\eta = 2 \times 10^{-5}\Omega m$ for $k_bT = 10eV$ yielding $R_m \approx 200$. This means that at the scale of the entire imploding plasma, the ideal assumption is fairly valid. When these assumptions are applied to Z-pinch plasmas, some important effects can be studied analytically, especially MHD

instabilities which are discussed below in section 2.3.

2.2 Snowplow Model

One of the simplest and most common model of a Z-pinch is known as the snowplow model. This is a 0D approach to model Z-pinch implosions and is inspired by ideal MHD. This model describes an implosion in which current is restricted to flow in an infinitesimal layer at the plasma-vacuum boundary and all mass encountered by the imploding shell is swept up with it. As the current shell implodes with each time-step, all mass encountered by the shell is added to the shell. It is also assumed that all energy is radiated away by the plasma, so thermal energy is neglected along with thermal pressure, necessarily. While lacking spatial detail and some important physical processes, the 0-D snowplow model allows rapid estimation of Z-pinch behavior which using the most important bulk quantities: total mass and current, while very roughly capturing the dynamics of the implosion.

The equation of motion applied to the snowplow model appears in equation 2.21

$$m(t)\frac{d^2r}{dt^2} + \frac{dr}{dt}\frac{dm}{dt} = \frac{\mu_0 I(t)^2}{4\pi r(t)} + P_c\left(\frac{r_{min}}{r(t)}\right)^8 \tag{2.21}$$

Where the left hand side is the time derivative of momentum, the first term on the right hand side is the magnetic force generated by the current and the second term on the right hand side is an arbitrary counter force acting as a surrogate for thermal pressure which limits compression. The mass added to the imploding shell is modeled by equation 2.22.

$$\frac{dm}{dt} = -2\pi r(t)\frac{dr}{dt}\rho(r) \tag{2.22}$$

The time dependent current is dependent on the load impedance, which is dynamic since

the conductor is imploding. Equation 2.23 couples the radius $r(t)$ to the current $I(t)$.

$$\frac{d^2}{dt^2}(IL) = \frac{1}{C} - R\frac{dI}{dt} \tag{2.23}$$

Where R is the nominal circuit resistance and $L(t)$ is the total circuital inductance expressed in equation 2.24

$$L(t) = L_0 + \frac{\mu_0 l}{2\pi} ln\left(\frac{r_{return}}{r(t)}\right) \tag{2.24}$$

and r_{return} is the return current radius of the load region.

Solving this set of equation numerically yields a time evolution of all parameters. The most useful parameters to examine when studying the general dynamics of the problem are the current $I(t)$ and radius $r(t)$. A solution of a sample problem using the CESZAR circuit parameters (discussed in chapter 3) and a Gaussian initial gas profile ($\rho(r)$) is shown in figure 2.1.

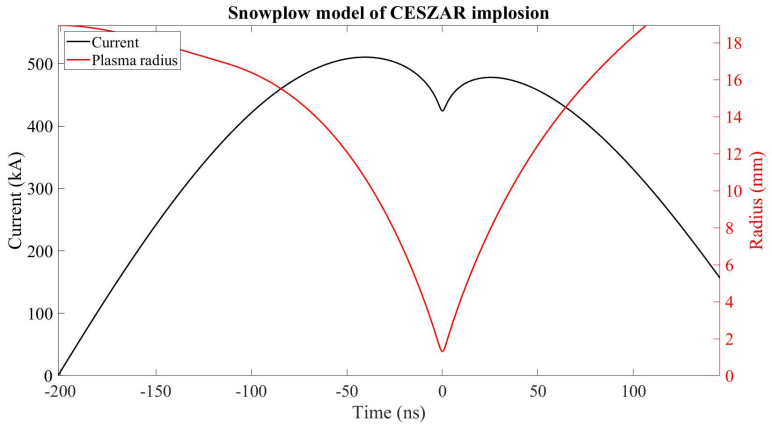

Figure 2.1: Numerical solution of the plasma radius and current of a CESZAR implosion using a 0-dimensional snowplow model. The calculation was initialized with a Gaussian density profile and the nominal CESZAR circuit parameters.

The pronounced dip in the current profile is a result in the sharp rise in inductive impedance accompanying the dramatic contraction of the current sheath during peak compression. Observing the second term in equation 2.24 shows the load inductance increasing dramatically at small radii. The importance of this term is best understood relatively to the static inductance of the pulsed

power circuit, L_0. A plot of the inductance produced by the snowplow calculation is shown in figure 2.2. The inductive peak coincides with the minimum radius (and local current minimum shown in figure 2.1. Pulsed power drivers with a relatively high static impedance (compared to the inductive reactance) will not exhibit such a pronounced dip in the current profile. Likewise, implosions that do not exhibit snowplow-like behavior, i.e. the current sheath does not closely follow the imploding plasma, will not exhibit inductive dips or notches in the current profiles.

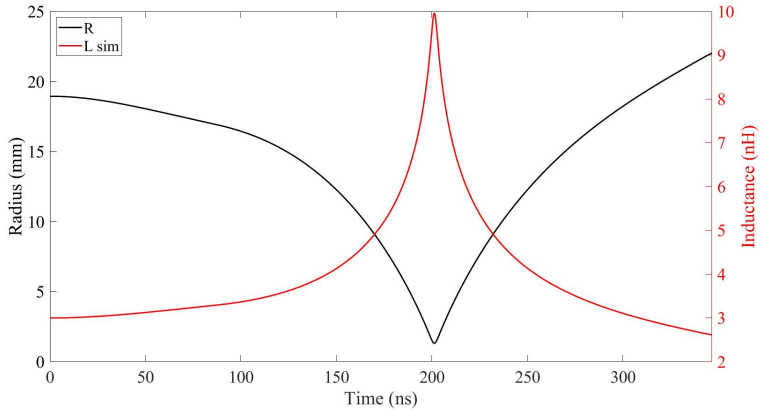

Figure 2.2: Numerical solution of the plasma radius and inductance of a CESZAR implosion using a 0-dimensional snowplow model.

2.3 Instabilities in Z-Pinches

2.3.1 Current-driven Instabilities

Instabilities have been observed in Z-pinches since the first experiments [4]. Current-driven instabilities occur as a result of differential magnetic pressure around the plasma-vacuum boundary due to the magnetic field's dependence on radius in the vacuum region. Using the same static equilibrium considered when discussing the Bennett relation, the right hand side of equation

2.8 can be rewritten only in terms of B using 2.5, and since $B = B_\theta$ we have:

$$\nabla p = \frac{\nabla B^2}{2\mu_0} \tag{2.25}$$

where $\frac{B^2}{2\mu_0}$ is known as the magnetic pressure. While an axially dependant perturbation to the sharp plasma-vacuum boundary is present, magnetic pressure will be greater wherever the perturbed plasma column is constricted, while the magnetic pressure will be less at any point where the perturbed surface bulges radially outward, causing the perturbations to grow. This effect is illustrated in figure 2.3 below.

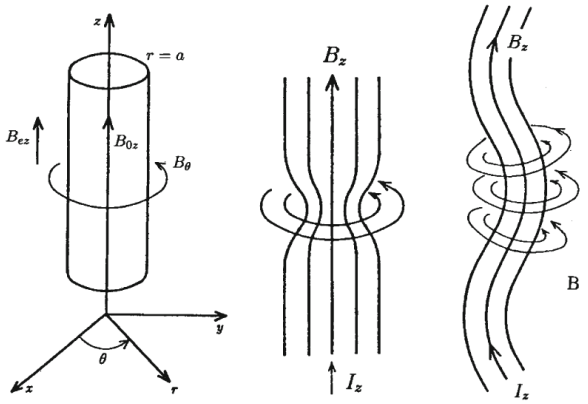

Figure 2.3: Illustrations of the MHD instabilities with the 'sausage' instability in the center and the 'kink' instability on the right. figure from Miyamoto [74].

When an axial magnetic field is present, equation 2.8 becomes:

$$\nabla p = \frac{\nabla B^2}{2\mu_0} + \frac{(\mathbf{B}\cdot\nabla)\mathbf{B}}{\mu_0} \tag{2.26}$$

where the second term on the right hand side describes the force associated with the 'stiffness' of the magnetic flux [69]. In this situation, the global magnetic field is helical and a secondary mode of the current-driven instability occurs known as the 'kink' instability. With a pre-embedded axial magnetic field under ideal MHD assumptions, a perturbation of the plasma-vacuum boundary will tend towards a bent perturbation due to the 'tension' term in equation 2.26 [70]. A 'kink'

type perturbation in the plasma column, will be accompanied by a region of higher magnetic field strength on the inside of the kink, and lower field strength on the outside of the kink, causing the kink to grow. In fast gas-puff Z-pinches, these types of current-driven instabilities are only important, if at all, during the stagnation phase where the plasma reaches a small radius and the magnetic fields can be high.

2.3.2 Magneto Rayleigh-Taylor Instability

The most important instability in the type of gas-puff implosions presented in this thesis is known as the magneto Rayleigh-Taylor instability. This is the MHD analogue to the gravitational Rayleigh-Taylor instability common in fluid mechanics. The gravitational instability occurs at the interface between two fluids of different densities, ρ_1 and ρ_2 where the low density fluid pushes onto the higher density fluid. For example, a vessel of fluid where low density oil sits below relatively high density water. This situation may be momentarily balanced, but any disturbance in the oil-water boundary will lead to runaway buoyant motion of both fluids until the oil sits above the water. This can also be described as a misalignment between pressure and density gradients at the interface leading to runaway baroclinic torque [75]. To translate this picture to Z-pinch implosions, the 'light' fluid is the vacuum region where the magnetic field pushes into the plasma. Alternatively, $\nabla\rho < 0$ while $\nabla p > 0$ and $\nabla\rho \nparallel \nabla p$. Figure 2.4 shows an illustration of the MRT instability mechanics. In this picture, the plasma exists in the lower half with no magnetic field. The top half contains no plasma but the magnetic field is oriented out of the page. This configuration results in a density gradient across the boundary towards the plasma, and since the magnetic pressure is greater than the plasma thermal pressure,

Linearizing the ideal MHD equations assuming the time varying perturbations to an equilibrium state are sufficiently small, the evolution of the perturbed interface boundary, ξ, can be solved analytically, resulting in an exponential growth of the perturbation $\xi(t) = \xi e^{i\gamma t}$ [76].

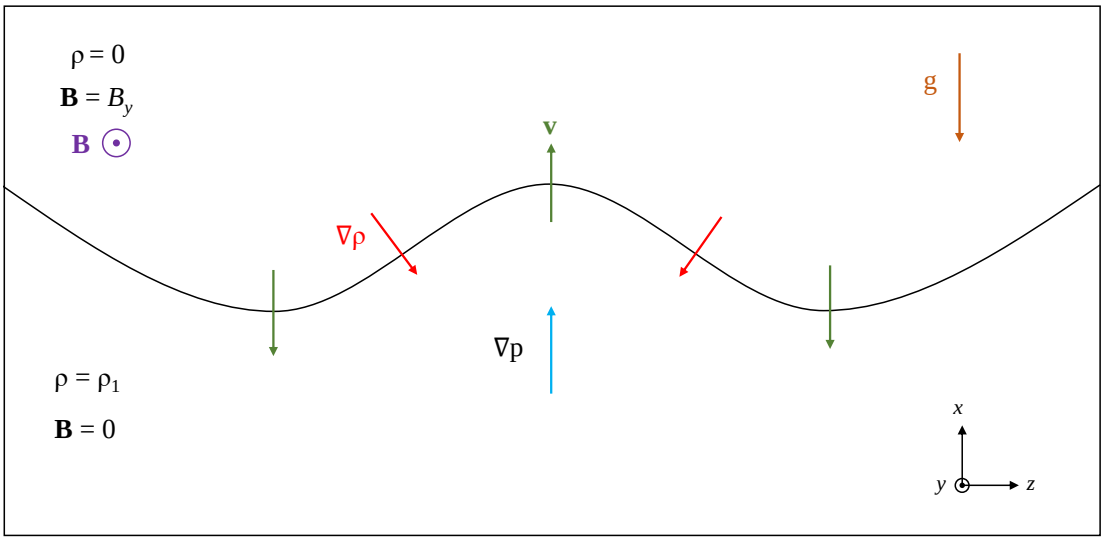

Figure 2.4: Illustration of the magneto Rayleigh-Taylor instability. The lower region represents the plasma with density ρ_1 and no magnetic field, while the upper region represents the vacuum with **B** oriented out of the page

The growth rate is

$$\gamma^2 = gk - \frac{(\mathbf{k}\cdot\mathbf{B})^2}{\mu_0 \rho} \tag{2.27}$$

where g is the acceleration and k is the spatial frequency of the perturbation. Equation 2.27 indicates that the growth rate is reduced by a magnetic field oriented along the instability mode vector. In the simple picture shown in figure 2.4, $\mathbf{k}$ is in the z direction, so if $\mathbf{B} = B_y\hat{y} + B_z\hat{z}$ everywhere, the instability growth will be mitigated. This is one of the primary reasons why external axial magnetic fields are often utilized in Z-pinch experiments. The axial magnetic field ultimately reduces the pressure gradient across the boundary, reducing the magnitude of the misaligned pressure and density gradients. Equivalently, the axial magnetic field provides a restoring force to the perturbation, since compressing the magnetic flux requires more work by the driving force. The stability of Z-pinches, MRTI, and effects of an axial magnetic field have been widely studied and remain important areas of Z-pinch research [77, 78, 79, 80, 81, 82].

2.4 Gas-puff Considerations

2.4.1 Initial Breakdown

An important process in gas-puff experiments is the initial breakdown phase. Since gases are composed of neutral atoms and molecules, they are very poor electrical conductors. To allow for current to flow through the material and accelerate it, the gas must be ionized to some degree. Often, the initial portion of the current or pre-pulse may be sufficient to initiate what is known as an electrical breakdown in the gas, which at least partially ionizes the gas into an electrically conductive medium.

An electrical breakdown, sometimes called 'dielectric breakdown' occurs when material is subject to an electric field that is greater than the dielectric strength of the material. Equivalently, the applied voltage exceeds the material's breakdown voltage V_{bd} which depends on the geometry of the electrodes. In gases, the breakdown voltage varies between species and also depends on the gas pressure. The physical mechanism at play in breakdown of gases is known as the 'Townsend avalanche'. A neutral gas contains some small portion of free electrons. When positioned between two parallel plates with V_{bd} across them, some of these free electrons will accelerate and gain enough kinetic energy to ionize a neutral atom it encounters, releasing more free electrons who in turn, accelerate and ionize more atoms. This cascade continues until many ionization events occur and a large portion of the gas is ionized between the two plates and current can easily flow in the ionized gas. For a given gas and electrode geometry, the breakdown voltage is only a function of the gas pressure and spacing between anode and cathode. The relationship is known as Paschen's law [83].

$$V_{bd} = f(pd) \tag{2.28}$$

A graphical representation of Paschen's law is shown in figure 2.5 from Kuffel. At $(pd) < (pd)_{2N}$, accelerated electrons have a relatively low chance to encounter and ionize an

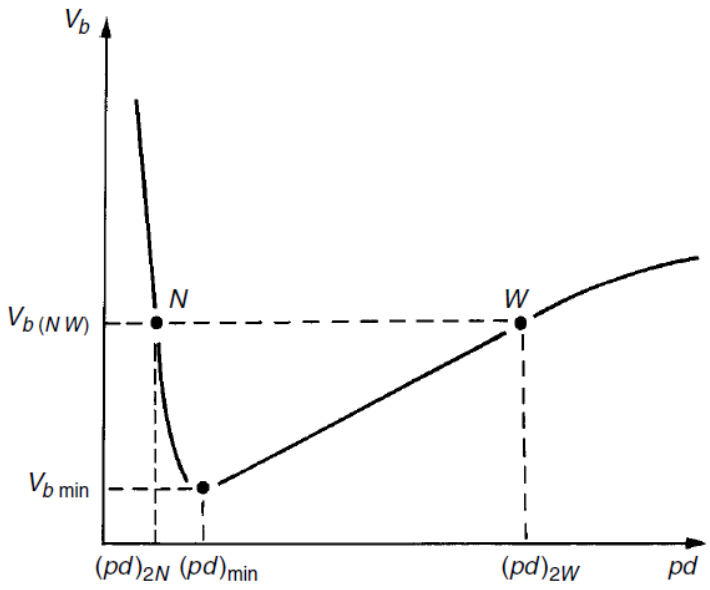

Figure 2.5: Paschen curve displaying the dependence of breakdown voltage on the product of gas pressure and gap distance. The points labeled N and W correspond to notable transitions in the conditions for the breakdown can occur, resulting in the visible inflection points in the curve. Figure from Kuffel [83].

atom between the anode and cathode since the avalanche or cascading breakdown is ultimately a probabilistic phenomenon. Small increases in pd in this region lead to a dramatic increase in ionization probabilities and therefore a lower breakdown voltage. This relationship holds until a minimum breakdown voltage is reached, where voltages below this threshold will not breakdown, regardless of (pd). At $(pd) > (pd)_{min}$, for a given voltage along the Paschen curve, further increasing pd means the electrons that might have initialized the cascade are more likely to collide with atoms before they have reached sufficient kinetic energy to ionize them, making breakdown impossible, unless the voltage is increased.

The Paschen law well describes voltage breakdown for a specific scenario where an electric breakdown disrupts a static charge separation through a gas between two electrodes. A key difference between this picture and the self-breakdown preceding a gas-puff Z-pinch is the fact that the voltage pulse supplied by the driver is highly transient. For a fixed gap distance, the pressure dependence for gas breakdown a pulsed plasma focus device was studied by Kies [84].

It was found that significantly higher voltages were necessary than indicated by Paschen's law for breakdown to occur in the pulsed voltage scenario. For these experiments, the relationship between pressure and breakdown voltage appeared more similar to the low pressure regime of the Paschen curve ($(pd) < (pd)_{min}$) meaning that ions do not often strike the cathode surface and generate secondary electrons. Additionally, the breakdown will occur at some 'lag time' after the voltage is applied [83]. Like the breakdown voltage, the lag time depends on pressure, electrode geometry and voltage pulse. Because the breakdown event requires ambient free electrons typically thought to exist due to cosmic radiation, breakdown in Z-pinches can be assisted by preionizing the gas with UV radiation, increasing the number of free electrons available to initiate the cascade, thereby reducing the 'statistical lag' associated with the breakdown lag time. In gas-puff Z-pinches, facilitating the breakdown phase ostensibly improves shot-to-shot reproducibility [10].

2.4.2 Axial Density Gradients

A gas injected into a vacuum region from a valve will undergo adiabatic expansion. In cylindrical geometry, a volume of gas with an initial bulk velocity in the z direction will exhibit expansion in the radial direction. Because of this expansion and bulk motion, there will exist an axial dependence on the radial density profile of the gas and a cone-like shape of the gas-puff. Assuming that current flows near the vacuum, plasma boundary, the force driving the implosion will be greater where the gas is more radially confined, leading to a faster implosion near the nozzle, and a slower implosion at axial positions further from the nozzle. This phenomenon is known as 'zippering' and results in a reduced and stretched peak x-ray flux.

This effect can be mitigated in a number of ways. On the timescale of the current pulse (hundreds of ns), the gas injector flow is negligible, since the flow evolves over 100s of microseconds. One technique to mitigate zippering is to time the current pulse to a favorable unsteady flow of the gas nozzle, e.g. when the flow rate is still increasing and not yet steady. This

way, there exists an axial gradient in linear mass (defined in equation 2.29) which can counter the zippering caused by the axial gradient in the current radius.

$$M_L(z) = 2\pi \int_0^R \rho(r,z) r dr \tag{2.29}$$

where R is the radius of the vacuum boundary. Another method to minimize zippering is to reduce the flaring of the gas puff with a supersonic flow. With a de Laval nozzle geometry, flow past the choke point will be supersonic ($M = \frac{v}{v_s} > 1$) where M is the Mach number, a ratio of the flow velocity and sound speed of the medium. Because adiabatic expansion occurs at the sound speed, a flow greater than the sound speed can produce a more collimated density profile before radial expansion becomes significant. Work by Hussey et al. [85] using a modified snowplow model found that zippering could be reduced for high Mach number nozzles. Details of the injector design used in the CESZAR experiments will be covered in chapter 3.

Chapter 3

Pulsed-Power Drivers and Diagnostics

3.1 Weizmann Institute of Science Laboratory

3.1.1 WIS Circuit Characteristics

The pulsed power driver used for experiments at WIS presented in this thesis consists of four 4 μF capacitors coupled to the load region. The capacitors are charged to 23 kV and discharged through the gas-puff load where the anode is the metallic injector and the anode is a transparent wire mesh. The cathode is connected to ground via return current posts residing a radius of $\sim$ 12 cm. The circuit diagram for the pulsed power system is shown in the figure 3.1 and upon discharge, represents a series RLC circuit.

While the nominal parameters for the pulsed power machine are $L = 55nH$, $R = 15m\Omega$, $C = 16\mu F$, the measured transient response of the driver do not match these values. The driver current as a function of time can be modeled as a dampened sine wave shown equation 3.1.

$$I(t) = Ae^{\frac{-t}{\tau}} sin(\omega t + \phi) \tag{3.1}$$

For which $A = V_0\sqrt{\frac{C}{L}}$, $\tau = 2\frac{L}{R}$, and $\omega = \sqrt{\frac{1}{LC}}$ and V_0 is the charge voltage of the capacitors.

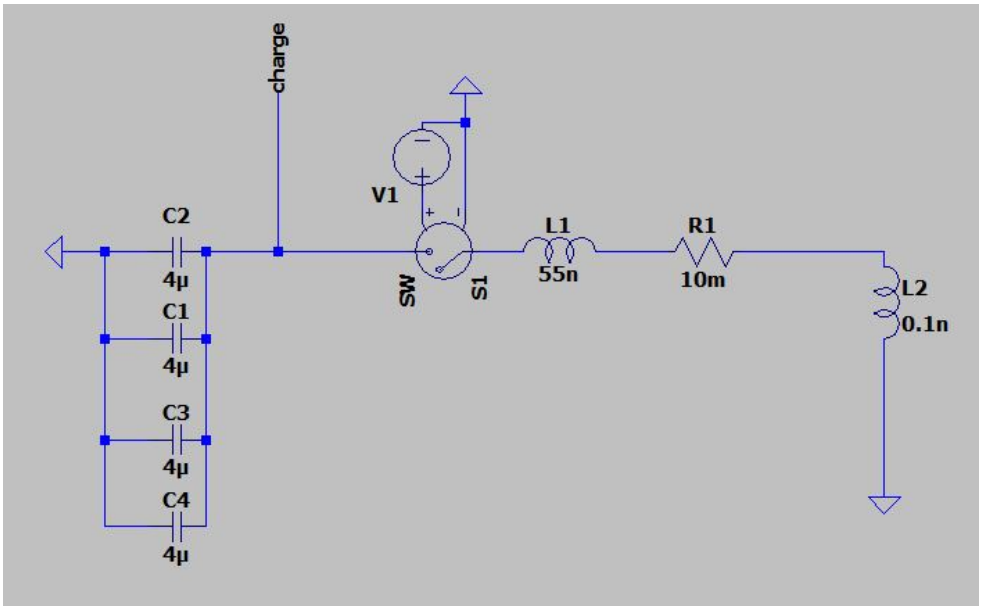

Figure 3.1: Circuit diagram of the WIS driver used for LTspice simulations with a static load. The circuit parameters were chosen to match a measured current profile. The values for capacitance (C), resistance (R), and inductance (L) are expressed in μF, nH, and $m\Omega$. A closing switch is included in the model to allow for a pulsed current.

Adjusting the value of R and L and to match the analytic response to an experimentally measured current profile with a short circuit load yields a machine inductance of $L = 55nH$, and $R = 10m\Omega$. This was also confirmed in numerical simulations of the modeled circuit. The measured current profile, analytic fit, and LTspice results are shown in figure 3.2. To better fit the experimental data, a phase shift of $\phi = 0.1$ was added to the analytic expression. This shift likely accounts for the relative delay between the switches which discharge the capacitors in the experimental discharge.

Current traces during a plasma discharge exhibit some features distinct from short circuit discharges. Figure 3.3 compares an experimental current traced averaged over several discharges of the same conditions as well as the analytic profile shown in figure 3.2 and a modified analytic expression. The first important feature in the experimental current trace is the dip in current at ~ 700 ns. This is due to the sudden increase in inductive impedance in the load as the plasma column pinches. Next, it is clear from figure 3.3 that the nominal circuit parameters do not match the experimental trace. There are several reasons for this. As mentioned previously, the initial rise

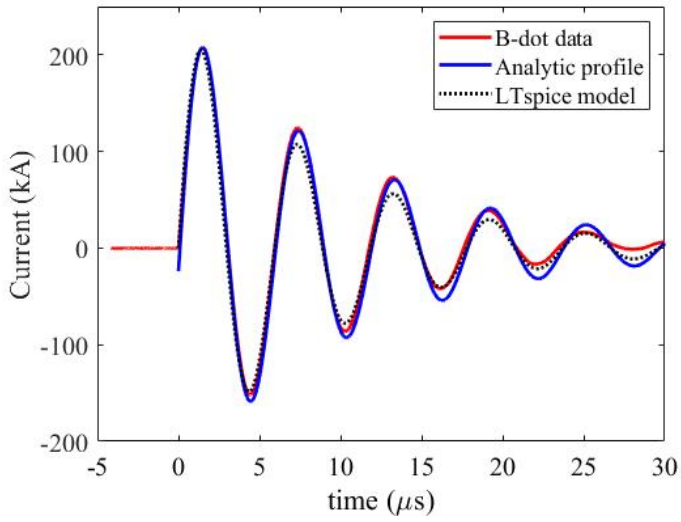

Figure 3.2: Current profiles for a discharge into a short-circuit load on the WIS driver. The red curve is the current measured by a calibrated B-dot probe, the blue curve is the dampened sine wave and the dotted black curve is the LTspice simulation result.

of the discharge is affected by the imperfect synchronicity of the closing switches which cannot be captured by the analytic model nor a numerical simulation. Second, the gas-puff load exhibits greater inductive impedance than the short circuit load and greater resistance. For a stationary coaxial conductor, the inductance can be calculated from equation 3.2

$$L = \frac{\mu_0 d}{2\pi} ln(\frac{R_{return}}{R_{load}}) \tag{3.2}$$

Where d is the length of the conductor or load, R_{return} is the radius of the return posts and R_{load} is the radius of the load, or gas-puff. For the WIS experiment, $d = 2cm$, $R_{return} = 120cm$, and $R_{load} \approx 1.9cm$ which results in an initial load inductance of $L = 7.4nH$. To produce the adjusted curve in figure 3.3, a value of $L = 70nH$ and $R = 20m\Omega$. These values are 15 nH and 10 $m\Omega$ greater than the nominal circuit values, but considering the discrepancy due to the switch synchronicity, the true load inductance and resistance are likely much less than 15 nH and 10 $m\Omega$, respectively.

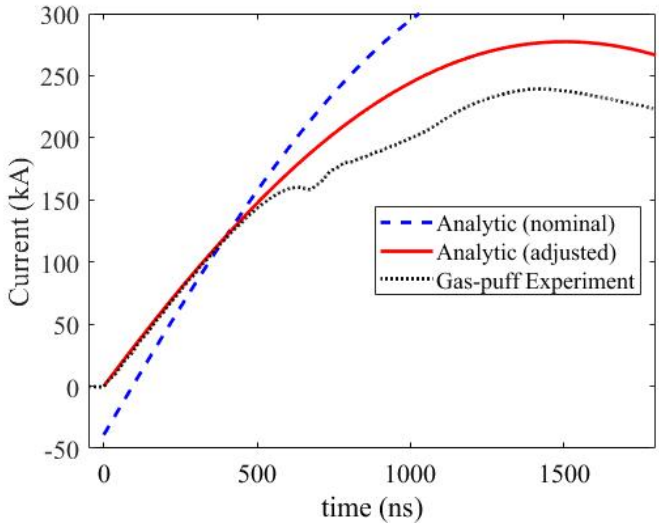

Figure 3.3: Current profile for gas-puff discharges on the WIS driver and analytic profiles. The black dotted curve is an experimental current profile averaged over several shots, blue dashed curve is the analytic expression for nominal circuit values and the red curve is an analytic expression with adjusted circuit values.

3.1.2 Diagnostics Arrangement

The experiment at WIS employed three separate time-gated spectrometers, one dedicated to measure the axial magnetic field, one to measure the azimuthal magnetic field, and one to measure the plasma temperature and ionization distribution.A time gated intensified charge-couple device (ICCD) camera was employed to capture a 2D image of the plasma self-emission. In addition, a photodiode was used to observe the time dependent UV-visible emission from the plasma. A diagram of the experimental arrangement used at WIS is shown in figure 3.4. For clarity, some optical elements (such as mirrors) were omitted from the figure. To assist with the initial breakdown of the gas-puff, the cathode was designed with a cylindrical knife-edge geometry as illustrated in figure 3.4. A wire-mesh is placed at the base of the knife edge to allow transparency of the gas through the cathode while providing a quasi-continuous conductive material at the electrode. The knife-edge radius is 19 mm to match the outer extent of the gas-puff and protrudes 1 cm from its base, leaving an additional 1 cm from the knife edge to the anode (gas injector exit plane). This geometry means that approximately half of the plasma column is

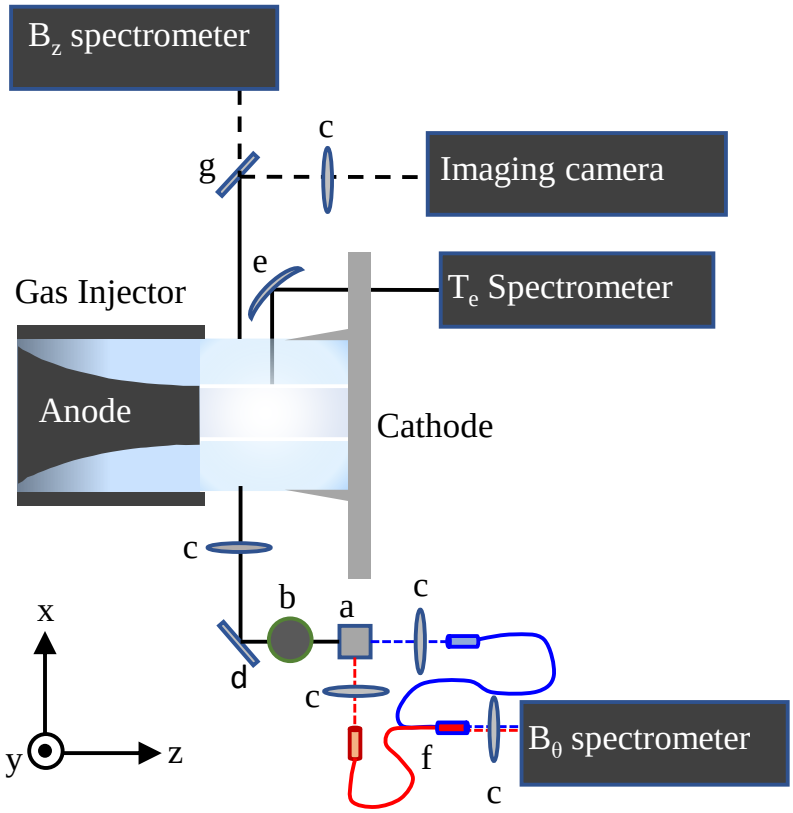

Figure 3.4: Diagnostic arrangement of the WIS experiment. The following elements are as follows: a) polarizing beam splitter cube, b) λ/4 wave-plate, c) lenses, d) flat mirrors, e) spherical mirror, f) bifurcated fiber bundle, g) beamsplitter.

hidden from diagnostic view by the cylindrical knife edge.

The axial magnetic field spectroscopic system used direct Zeeman splitting of the Al III $4s^2S_{1/2} - 4p^2P_{1/2}$ transition at $\sim$ 5722 Å. An aluminum plume was produced with a pulsed infrared laser aimed at an aluminum plate positioned at the center of the gas injector exit plane. The laser system produced a 7 ns pulse with 300 mJ of energy at 1064 nm. The emission from the Al plume was observed to be typically 1-2 mm in diameter, so that measurements of B_z were limited to $r < 2mm$. Because the Al plasma is transient and short lived, the laser pulse was carefully timed with the plasma implosion and diagnostic windows. An illustration of the Al

plasma plume for B_z measurements is shown in figure 3.5 The spectrometer used for the axial

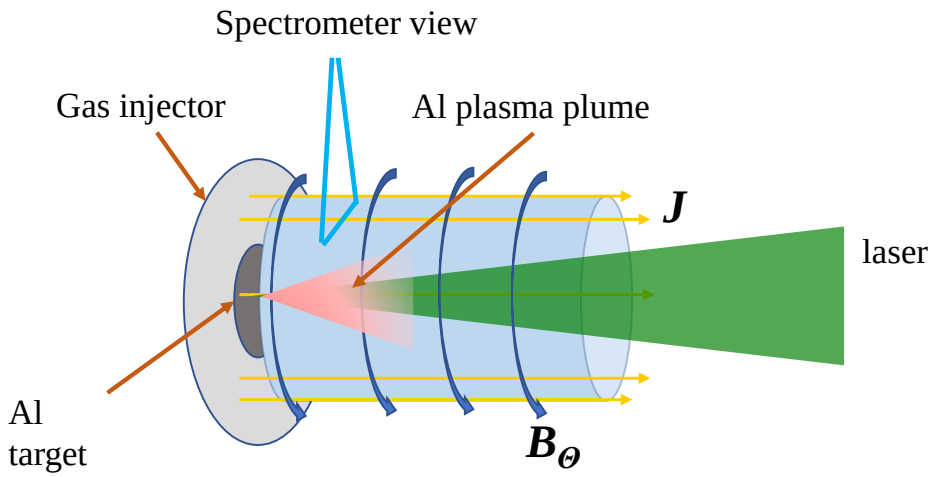

Figure 3.5: Illustration of the axial magnetic field diagnostic system. Shown in green is the laser focused on the Al plate located at the gas injector exit plane in the center of the gas puff (blue) and the Al plasma plume in pink.

magnetic field measurement had a 2400 gr/mm grating and 1 m focal length. With a 50μm slit, the spectral resolution was $\sim$ 0.4 Å. A polarizer was used to select for only the σ transitions, as both σ and π components are observable in the perpendicular line of sight used in the B_z diagnostic. Because the σ components are split to a greater degree than the π components, filtering out the π components simplifies the measurement and provides greater certainty in low signal to noise situations. 3.6.

The spectrometer was coupled to a gated ICCD to record the spectral image using a telescopic lens system in the optical line of sight. For these experiments, a gate of 30 ns was used to acquire a strong enough signal from the Al plasma emission. A spectral image of the Al emission is shown in figure The $^2S_{1/2} - ^2P_{1/2}$ emission line was chosen over the $^2S_{1/2} - ^2P_{3/2}$ line because even though the signal of the later appears brighter, the former contains only one component of each $\sigma+$ and $\sigma-$. This means that no averaging of multiple components is required which would reduce the certainty of the measurement. The spectral lineout of the $^2S_{1/2} - ^2P_{1/2}$

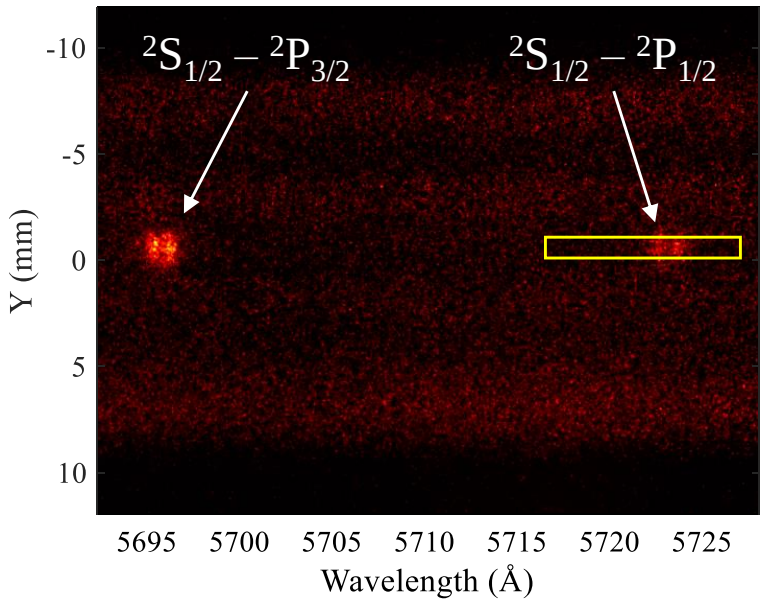

Figure 3.6: Spectral image of the Al plasma on the WIS experiment. Two components of an atomic multiplet transition are observable, though only one is used for B_z determination.

Al III transition is shown in figure 3.7 fitted to a double Gaussian function used to determine B_z.

The spectrometer used to measure the plasma temperature (labeled T_e Spectrometer in figure 3.4) was a 0.5 m focal length imaging spectrometer with an 1800 gr/mm grating. A spherical mirror was used to image the plasma onto the entrance slit of the spectrometer. The spectral window was set to $5500-5620$ Å with high reflectivity in the second order, meaning emission in the range of $2750-2820$ Åwas also detectable. The spatial view of the spectroscopic system was between $y = -10\,to\,14\,mm$ across the load region, with the central axis at $y = 0$. The axial position of the field of view was adjusted throughout the experiment from $z = 1-9\,mm$. An ICCD camera was coupled to this spectrometer. The gate of the detector was adjusted from 3 ns to 20 ns. The axial position of the field of view for all three spectrometers were set at the same position simultaneously.

The azimuthal magnetic field (B_θ) diagnostic utilized the polarization parallel method discussed in section 1.4.4. The system is illustrated in figure 3.4. The first lens in the imaging

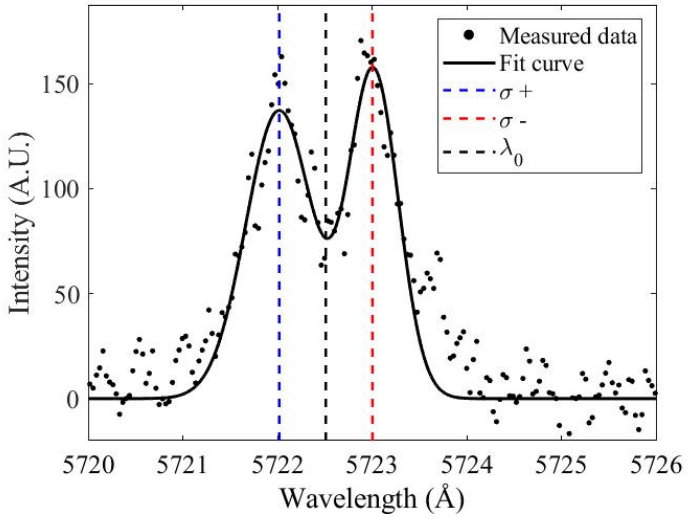

Figure 3.7: Spectroscopic data of Al plasma fitted to two Gaussian profiles. Shown is the central wavelength of the un-split emission line. The peak separation is used directly to calculate B_z.

system is placed at a distance equal to its focal length from the central axis. A $\lambda/4$ waveplate allows circularly polarized light to be converted to linearly polarized light before it passes through the polarizing beam splitter cube. The polarization optics used in this experiment were specifically chosen to operate in the UV range of interest which was near 3800 Å. After the beam splitter, the collimated light was focused onto the entrance of a fiber array. Each half of the bifurcated fiber bundle consisted of 50 fibers. The combined 100 linear fiber array is imaged onto the the spectrometer which used a 2400 gr/mm grating and 1 m focal length coupled to a time gated ICCD with a resulting spectral resolution of ~ 0.4 Å. The gate width used for this diagnostic system experiment was 30 ns. A sample spectral image is shown in figure 3.8. The spectral calibration, or dispersion, of each spectrometer was determined using emission lines of a lamp placed in the load region. For the B_θ spectrometer, the positions of Hg lines near from 3650 - 3664 Å were recorded. The known wavelength of this set of lines provides the linear dispersion (Å/pixel) at the chosen central wavelength. Since the Hg lines are near 3650 Å and the oxygen lines of interest are near 3800 Å, a recording of the Hg lines was repeated at various central wavelengths to verify that the relative dispersion is unaffected by the set central wavelength of

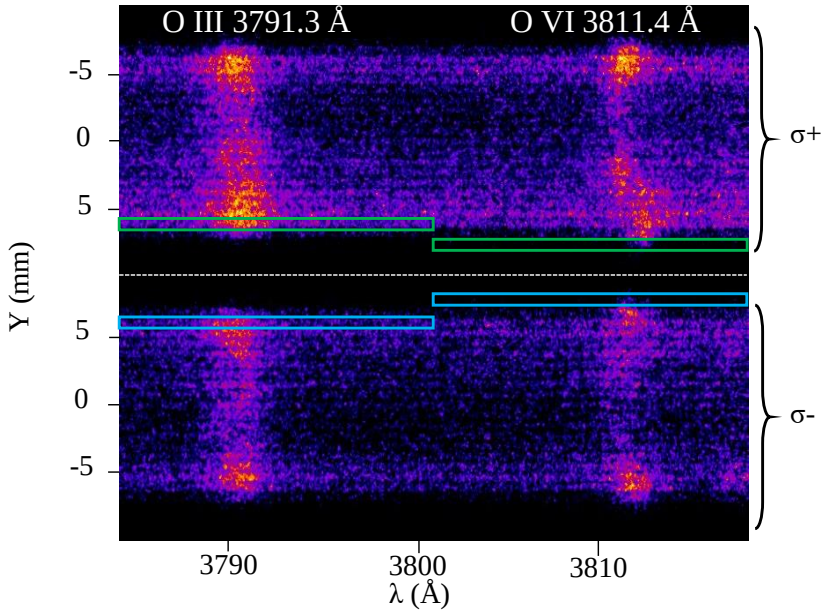

Figure 3.8: Spectrum from an oxygen implosion in the WIS experiment. Emission lines from both O III and O VI are detected simultaneously. The dotted center white line separates data from each path of the bifurcated fiber bundle. The blue and green rectangles represent the region of data selection at the outer edge of emission for both emission lines.

the spectrometer. A spectral image of emission from the Hg lamp is shown in figure 3.9.

Several processing steps are made to the selected data. First, a correction to an optical aberration is applied. The correction was determined using a spectral image obtained from emission of a mercury lamp placed in the load region. The curvature of the spectral line is measured as a deviation from the center of the image. Using the spectral dispersion (in Å) The deviations are then fitted to a polynomial as a function of vertical position. The aberration correction is then applied to the vertical position of the selected data. Figure 3.10 shows the curved emission line from the Hg lamp and the polynomial fit used for the correction. This aberration correction is especially important to for the B_θ diagnostic, since the wavelength shifts involved are small (0.076 Å/T for O VI) while the optical aberration can be responsible for a shift of up to 0.15 Å near the edges of the detector (though most data is obtained where the aberrations are less pronounced, and the correction is typically less than 0.05 Å). The corrected wavelength

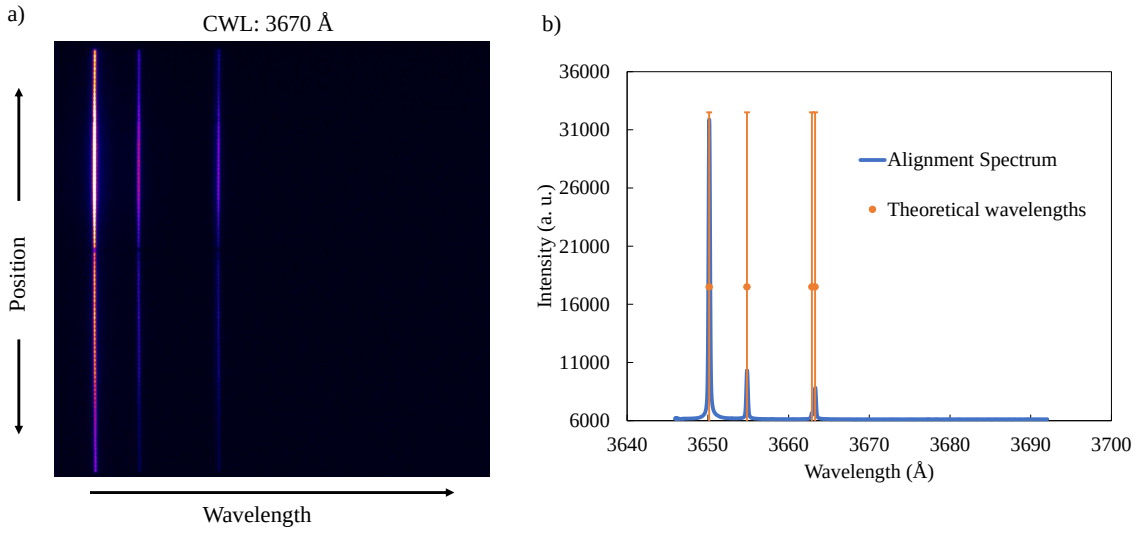

Figure 3.9: Spectrum obtained from alignment acquisitions using a Hg lamp centered at $\lambda = 3670$ Å. Part (a) shows the spectral image used for calibration. Part (b) shows the spectral lineout obtained through the center of the image in (a) along with the theoretical wavelengths in the range of the spectral window.

calibration can be understood by the expression in a practical expression of wavelength (Å) and horizontal pixel position (x) including the aberration correction which depends on the vertical pixel position $(C(y))$ shown in equation 3.3.

$$\lambda(x,y) = \lambda_0 + xD + C(y) \tag{3.3}$$

Where D is the spectral dispersion in Å/pixel.

Next, the background emission is subtracted by fitting a a polynomial to the continuum emission data lying in between the spectral lines and subtracting the background polynomial from the data. The processed data from each region shown in figure 3.8 are fitted to Voigt profiles to determine the spectral shift. The fitted profiles are shown in figures 3.11.

The UV-visible photodiode trace was recorded on a digital oscilloscope spliced together

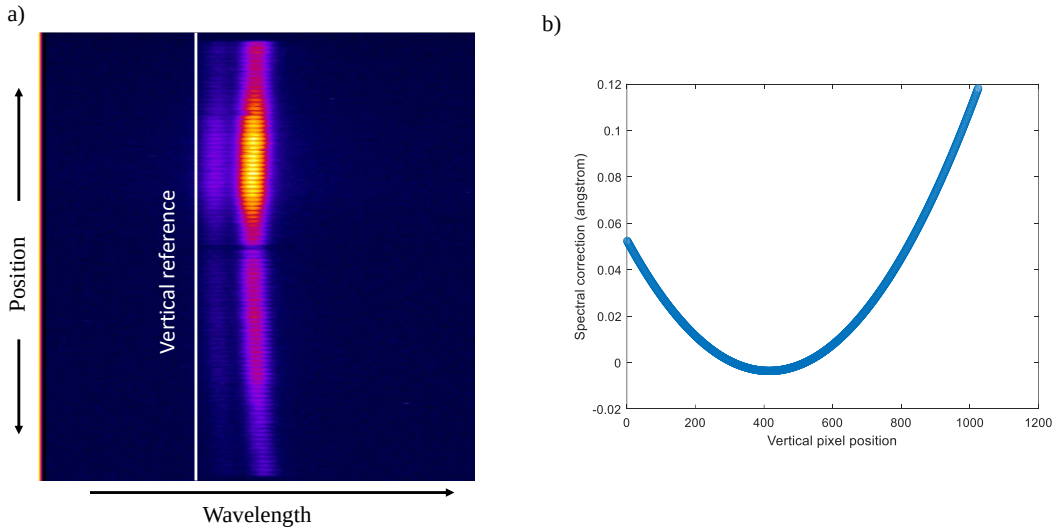

Figure 3.10: Image of one spectral line from the Hg lamp showing the optical aberration (a) and the spectral deviations as a function of vertical position of the image by pixel (b).

with a photodiode which detected the laser pulse as well as the diagnostic trigger pulse. The current trace and combined oscilloscope trace are shown together in figure 3.12.

The 2D imaging system consisted of a pair of lenses used along the same line of sight as the B_z spectrometer using a beam splitter and coupled to an ICCD. The gate of the ICCD was set to 5 ns for all shots and the spatial resolution was $\sim 0.5mm$.

3.2 The CESZAR Linear Transformer Driver

The Compact Experimental System for Z-Pinch and Ablation Research (CESZAR) is a linear transformer driver (LTD) [86]. The linear transformer driver is a relatively new technology used for HED experiments and allows for high peak currents on short time scales within a compact design [20]. The The CESZAR LTD cavity contains twenty "bricks" arranged in parallel and connected to a conical transmission line leading to the gas-puff load region. Each "brick" consists

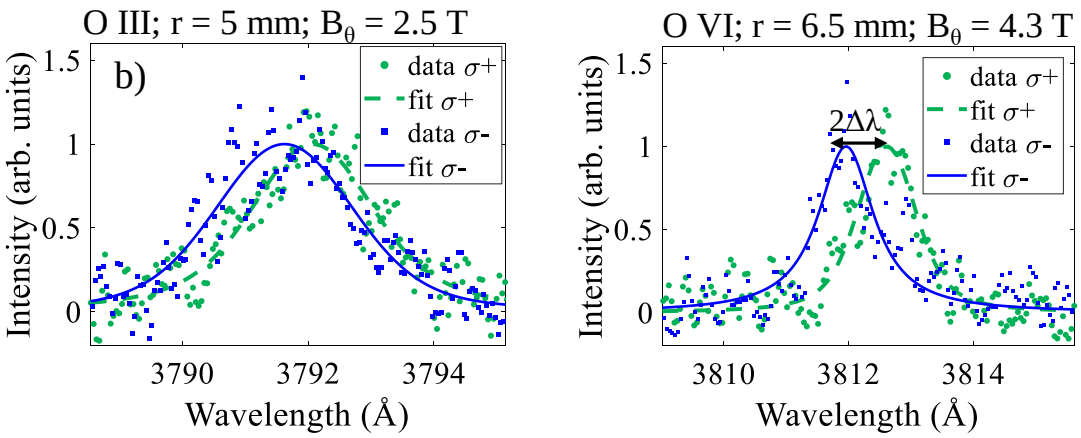

Figure 3.11: Experimental data (points) and Voigt fitted profiles (curves) for the O III lineout (left) and O VI lineout (right).

of two high-voltage capacitors connected in series to a spark-gap switch in between. This allows a dual polarity charge across the spark gap switch so that a charge voltage of $+V_c$ on one side is matched by a $-V_c$ charge on the other side, resulting in $2V_c$ across the switch (V_c is typically set to 60 kV for plasma experiments). The capacitors are connected directly to conical transmission lines feeding to the load region. Figure 3.13 shows a cross section of the CAD model of the machine as well as a photo of the open cavity from Conti et al. [86]. The LTD can be divided into two main sections, the cavity and the vacuum power feed. The cavity contains all twenty bricks and the trigger line and is filled with dielectric oil during normal operation. The top and bottom layer rows of capacitors are separated by an insulating polymer 'Rexolite ®' disk in which the trigger line is embedded. This disk also bears the seal between the oil filled cavity and vacuum power feed section. The vacuum section contains the conical transmission lines, gas-puff hardware and diagnostic access.

The transmission lines are in direct contact with the cavity body which is grounded. To prevent a significant portion of the discharge current from bypassing or shunting the load region directly to ground, two ferromagnetic cores are placed at the junction of the the vacuum and cavity sections, one for each polarity of the machine. The cores are composed of two Metglas® alloy toroids which consist of metallic glass tape wound around a central support ring with insulating

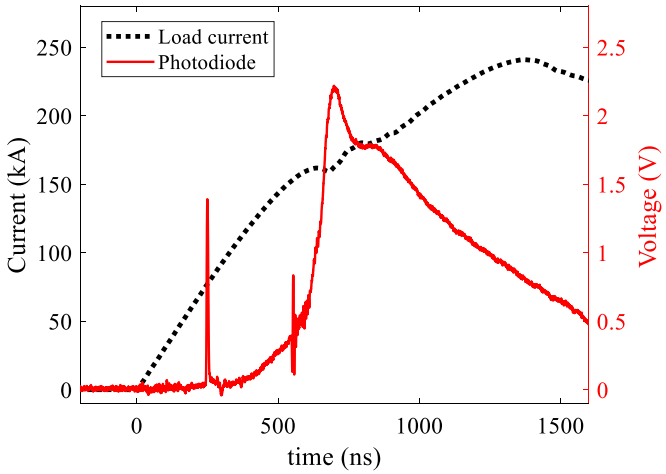

Figure 3.12: Sample current trace for an oxygen gas-puff shot (black) and combined photodiode, laser, and diagnostics trigger trace (red). The peak diode signal near 700 ns corresponds to the UV burst of the stagnation. The peak at $\sim$ 250 ns corresponds to the laser pulse, and the peak near 600 ns corresponds to the diagnostics trigger.

layers between each wrap. The presence of the ferromagnetic cores causes the direct circuital path to ground to hold a significantly greater inductive impedance than the path through the load region. To prevent the ferromagnetic cores from saturating to their magnetization limit during a CESZAR discharge, the cores are magnetically biased, or 'pre-magnetized' with an external pulsed current system prior to the CESZAR charge sequence so that the magnetization of the cores opposes the flux generated in them during the CESZAR discharge. During short circuit tests, the core pre-magnetization was shown to substantially increase the peak current in the load region during discharges [86].

Each switch is pressurized with filtered dry air to a calibrated "hold-off" level for a desired charge voltage. This procedure allows for reliable breakdown of the spark gap switch by the high voltage trigger system while preventing potentially damaging 'self-break' induced pre-fires during the charge sequence.

The primary CESZAR trigger system consists of a single 80 nF capacitor and spark gap-switch assembly which is charged to a greater voltage than one side of the CESZAR cavity (typically $V_c + 10kV$). The single spark gap switch is triggered to close by a $\sim$ 6 kV trigger

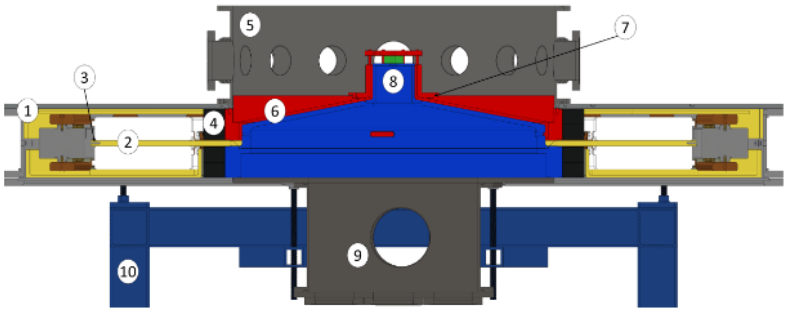

(a)

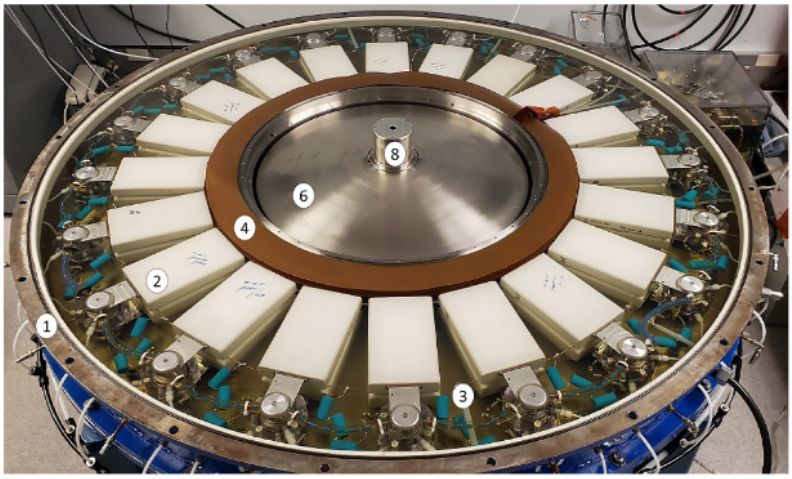

(b)

Figure 3.13: Cross section of the CESZAR 3D model (a) and photo of the open cavity (b). The labels are as follows: 1) LTD cavity, 2) brick assembly, 3) trigger line, 4) ferromagnetic cores, 5) vacuum section, 6) vacuum transmission lines, 8) load region, 9) vacuum pump section, 10) LTD support structure . Figure from Conti et al. [86]

pulse from a PT-55 unit which is itself triggered by a low voltage (300 V) pulse. When activated primary CESZAR trigger system sends a voltage pulse through a coaxial cable which is split to reach two halves of the CESZAR cavity, each half triggering 10 brick spark gaps through $\sim 1k\Omega$ trigger resistors which partially isolate each brick during breakdown. The circuit diagram of the CESZAR trigger system is shown in figure 3.14

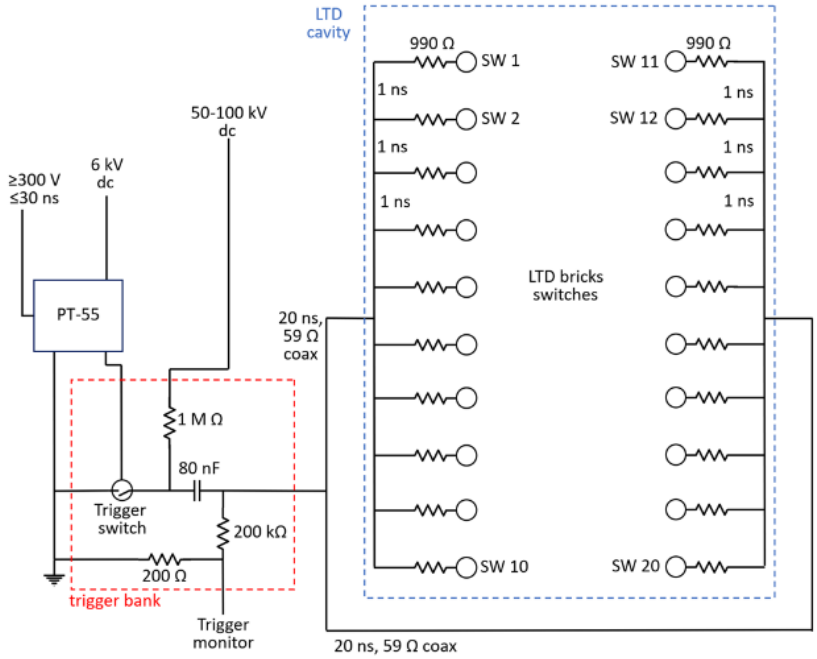

Figure 3.14: Circuit diagram of the CESZAR trigger system. The region outlined in blue is the CESZAR cavity while the primary trigger system is outlined in red. Figure from Conti et al. [86]

3.2.1 Machine Diagnostics

The measure the CESZAR discharge current, three pairs of deferentially wound b-dot probes are placed within the transmission line. The probes are placed at the end of the conical section of the transmission line at a radius of 10 cm from the central axis and 120 degrees from each other azimuthally. The differential probes consist of a pair of identical wire loops wound in opposite direction and set less than 0.5 cm apart. This design allows for subtraction of the capacitive coupling inherent in each probe since the voltage polarity induced by the changing flux within the loop will be opposite between the two loops, but the capacitive response will be nearly identical. The time dependent voltages of each normalized and filtered probe pair is then integrated and multiplied by its calibration factor to obtain the local machine current. The three sets of local current measurements are then averaged to obtain the total driver current trace.

The B-dot probes were absolutely calibrated using a current viewing resistor (CVR).

The CVR contains a resistor with a value low resistance and high precision, allowing accurate measurements of current based on the voltage differential across the shunt resistor ($I(t) = \frac{V(t)}{R}$). The integrated responses of the differential B-dot probe pairs were scaled to match the current measured by the CVR yielding a calibration factor for each individual probe. An example of

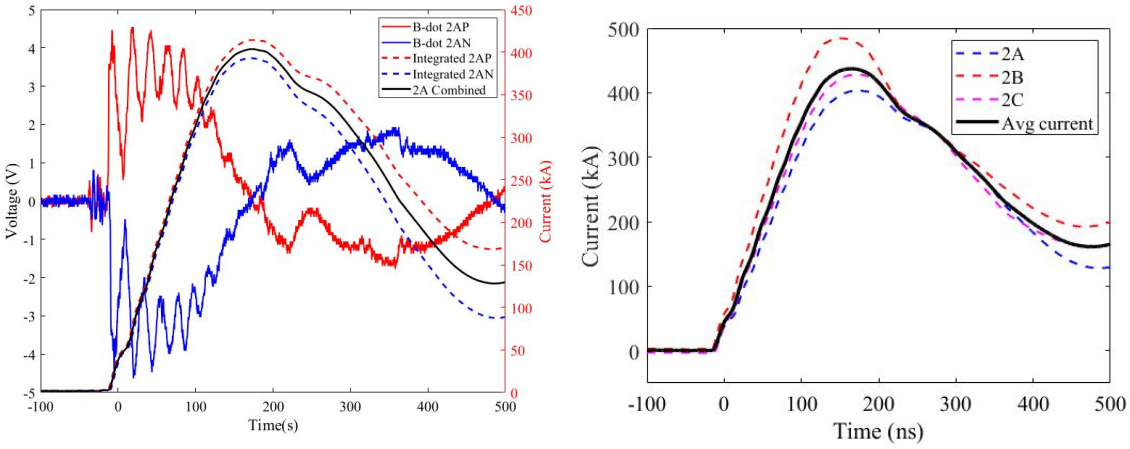

Figure 3.15: Raw b-dot voltage traces for one differential b-dot loop pair and integrated signals (a) and measured currents for all three differential probes (b). The blue and red curves in (a) result in opposite signals due to opposite winding (labels P, and N representing the positive and negative signals). The integrated and normalized signals are shown in the dashed curves and averaged to produce the black curve. In (b), current measurements for each differential b-dot probe and the total average machine current. The colored dashed curves represent the individually measured currents for each probe, and the black curve displays the total average current. The labels 'A', 'B', and 'C' refer to each differential probe.

differential b-dot traces and their averages are shown in figure 3.15. For clarity, only one of the three differential b-dot probes is shown. Figure 3.15 (b) shows the integrated differential b-dot current traces for all three probes and the total average current.

Each spark-gap switch in the CESZAR cavity is monitored by a coaxial D-dot probe placed near the mid-plane of the spark gap switches. These probes are open coaxial cables oriented towards the spark gap switch. The Electromagnetic waves generated by the highly transient spark-gap breakdown induce a voltage between the coaxial conductors, resulting in a signal corresponding to the time rate of change of the electric field near the D-dot probe. The switch monitors, while not absolutely calibrated, can provide a clue of the switch behavior. The

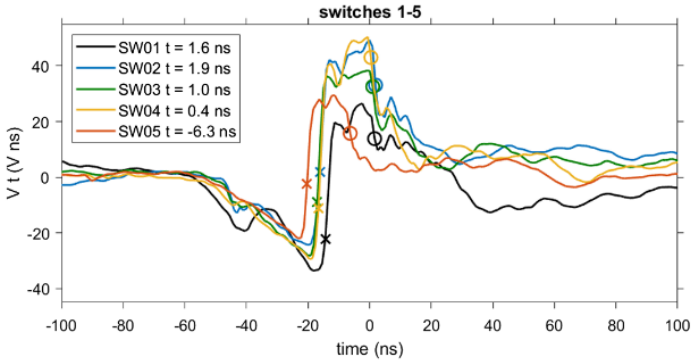

Figure 3.16: CESZAR switch monitor integrated signals for five spark-gap switches on the same CESZAR discharge. The asterisk points mark the point when the trigger pulse arrives at the spark-gap and the circles mark the point when the switch closes. Figure from Conti et al. [86]

integrated voltage signals shown in figure 3.16 indicate the time at which the trigger pulse arrives at the mid plane and when the switch closes, since the peak $\frac{\partial E}{\partial t}$ is expected to occur between these two events.

3.2.2 CESZAR Circuit Characteristics

The LTD cavity, CESZAR is a modified version of an LTD cavity developed at Sandia National Laboratories. Initial tests conducted at Sandia provide the nominal circuit characteristics of the components [87]. The nominal inductance, resistance, and capacitance of each brick is 172 nH, 300 mΩ, and 58 nF, respectively. Connected in parallel, the total cavity parameters are then expected to be 8.6 nH, 15 mΩ, and 1160 nF. The vacuum section parameters were calculated to an inductance calculated to be 5.2 nH and resistance of 3 mΩ resulting in pulsed power driver circuit parameters of $L_0 = 14.2nH$ and $R_0 = 18m\Omega$ [86]. A circuit diagram of the CESZAR driver is shown in figure 3.17.

The behavior of the CESZAR driver was studied with a series of test discharges simple short circuit placed between anode and cathode. The current profile measured with the b-dot probe array is then compared to numerical simulations of the circuit model to determine the true circuit

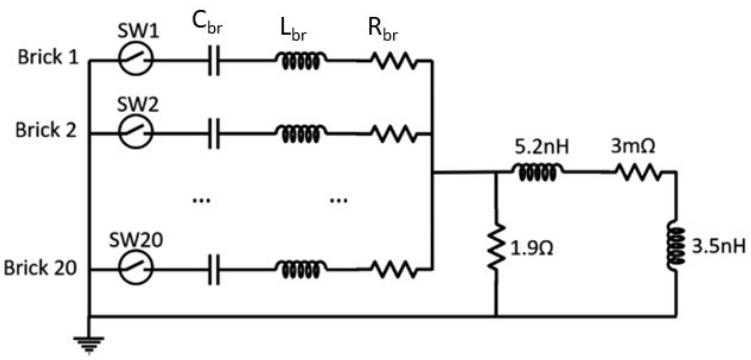

Figure 3.17: Circuit diagram of the CESZAR LTD cavity. The diagram is for-shortened to display the circuits of only bricks 1, 2, and 20 since each brick appears identical in the circuit diagram. Figure from Conti et al. [86]

parameters. The short circuit used was a 5 cm diameter, 2 cm long Al cylinder. Given the return current radius of 6 cm and using equation 3.2, the estimated load inductance is $L_{load} = 3.5nH$, resulting in a total load inductance of $L_{total} = L_0 + L_{load} = 17.7$ while the load resistance for the short circuit is negligible. The measured and modeled current profiles are shown in figure 3.18

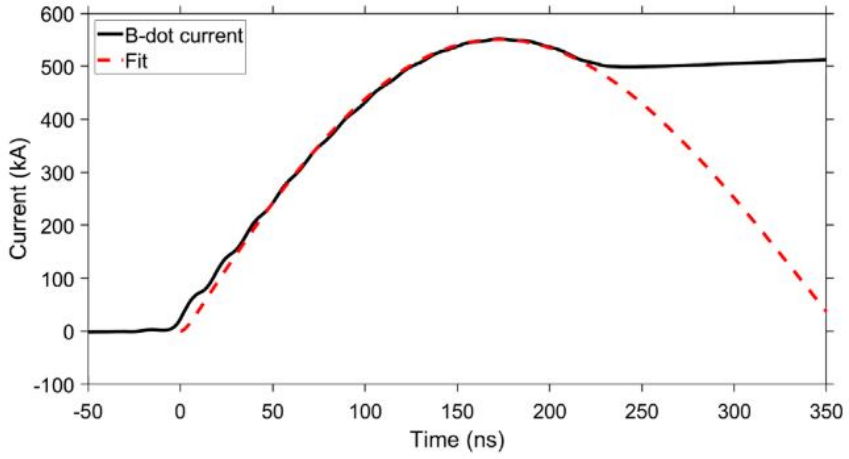

Figure 3.18: Measured and calculated current profiles of CESZAR discharge through a short circuit load. Figure from Conti et al. [86]

The resulting total circuit parameters determined by fitting the circuit model to the measured current profile resulted in $L_{total} = 22nH$ and $R_{total} = 21m\Omega$. The total measured

inductance is 4.3 nH greater than the nominal values, possibly resulting from altered brick connectivity compared to the original Sandia assembly. The machine inductance, is then $L_0 = L_{total} - L_{load} = 18.5nH$ The measured current trace in figure 3.18 does not oscillate as expected by the circuit model. This may be due to current shunting across the conical transmission lines, bypassing the region where the b-dot measurements are made. This observation was prevalent during initial tests of the CESZAR cavity and is less pronounced in later plasma experiments presented in this thesis.

While the driver circuit parameters remain constant during plasma experiments (L_0, R_0, C_0), the total inductance and resistance depends on the load geometry. For gas-puff experiments, the initial load inductance can be estimated with equation 3.2 with a return current radius of 6 cm, load radius of 1.8 cm and length of 1.3 cm resulting in a load inductance of $L_{gp} = 3nH$. Because the plasma implosion means the radius changes in time, the inductance is time dependant. Furthermore, to accurately model the current during a gas-puff implosion, the inductive reactance must be considered in the circuit model ($I\frac{dL}{dt}$). The plasma resistivity also depends on the plasma temperature as discussed in chapter 2. Accurately modeling the circuit behavior of a dynamic plasma load requires coupling the circuit model to the MHD problem.

3.2.3 CESZAR Plasma Diagnostics

The gas-puff Z-pinch experiments conducted on the CESZAR driver relied on a similar suite of diagnostics to those used in the WIS experiments discussed in section 3.1.2. These included a UV-visible spectrometer dedicated to B_θ measurements, a fast-framing XUV camera and filtered photodiodes to observe the temporal evolution of XUV/x-ray emission from the plasma. A diagram of the experimental arrangement used for the CESZAR experiments is shown in figure 3.19.

The spectroscopic system used for B_θ measurements for the CESZAR experiments was set up similarly to the system used in the WIS experiment discussed in section 3.1.2. The collection

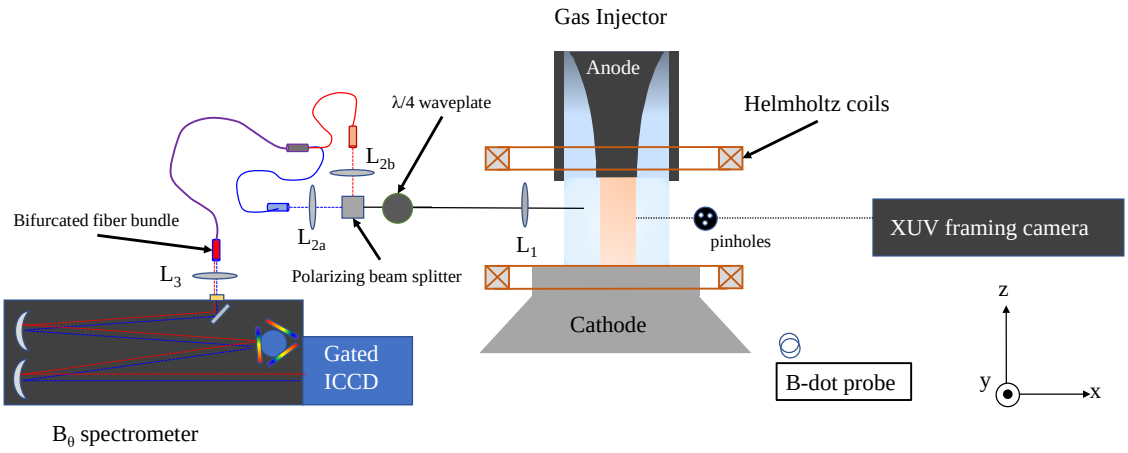

Figure 3.19: Diagram of the diagnostics arrangement for the CESZAR experiments. Shown are the B_θ spectroscopic system and XUV framing camera. The lenses used in the spectroscopic system are denoted as L_i.

lens (L_1 in fig 3.19) was placed inside the vacuum chamber 15 cm from the chamber center which is the focal length of L_1, so that the collected light is collimated as it is sent through the polarization optics ($\lambda/4$ waveplate and polarizing beam splitter cube), the collimated light is then focused on the entrances of each branch of the bifurcated fiber bundle using two 2.5 cm lenses (L_{2a} and L_{2b} in fig 3.19). The spectrometer used was a 750 cm focal length imaging spectrometer with a 2400 gr/mm grating and an entrance slit width of 50μm. The nominal spectral resolution of this system was 0.3 Å. The entire fiber bundle consists of twenty fibers each with a 200 μm silica core and a numerical aperture of 0.22. The array of fibers for each ten fiber leg form a 2.5 $\times$ 0.245 mm slit while the combined fiber array forms a 5.0 $\times$ 0.245 mm slit.

The optical system was set up and aligned in several steps. First, a laser diode beam was used to roughly align the center of each optical element with the center of the desired field of view of the load region. Second, a white lamp was placed at the joint end of the bifurcated fiber bundle and the positions of L_{2a} and L_{2b} were adjusted until a clear image of the illuminated fibers at a large distance ($\sim$ 2 m) which is considered as an 'infinite image' since $2\ m >> f_2 = 0.025\ m$.

The collection lens (L_1) is then adjusted to create a focused image of the illuminated fibers from one path (path a) at the chamber center, the pitch angle and position of the fiber bundle entrance for path a is finely adjusted to the desired field of view, and the image of the fibers from path b is adjusted to match that of path a. A mercury lamp was then placed at the joint end of the fiber bundle along with an appropriate band-pass filter to fine-adjust the image focus in the near-UV range using the ICCD detector to observe the UV-illuminated fiber bundle image. A similar aberration was observed with the Hg lamp emission as was observed in the WIS experimental system. A spatially dependent spectral dispersion correction was determined in the same manner as discussed for the WIS experiment 3.1.2 using the Hg lamp images obtained with the CESZAR spectroscopic system and applied to experimental plasma data obtained from CESZAR.

The spatial field of view of the spectroscopic system was obtained by capturing images of emission of the Hg lamp placed in the load region. A $\sim$ 2 mm object was placed at several positions with respect to the load hardware within the field of view of the spectroscopic system so the shadow of the object could be observed on the detector. Additionally, a scaled grid was placed in the load region and centered in the load hardware to verify the field of view of each fiber, and distance between each fiber to verify the measured spatial calibration and field of view. The spectral calibration was achieved using emission lines from the Hg lamp placed in the vacuum chamber in the same manner as was carried out in the WIS experiment and discussed in section 3.1.2.

The XUV framing camera consists of four pinholes located on the same plane mapped onto four quadrants of a micro-channel plate (MCP) detector which are each activated independently, however one of the quadrants was defective, so only three images were obtained for these experiments. The MCP quadrants are activated with a high voltage pulse which amplifies the photoelectrons generated by incident photons at each channel. The voltage pulse is approximately 5 ns in duration, resulting in three time gated images or 'frames'. The frames are temporally separated by using varied coaxial cable lengths whose associated pulse delay time were measured

within $\sim$ 0.5 ns. Typical inter-frame delays for CESZAR experiments are 20 ns. Because MCP operation requires high vacuum conditions to avoid arcs across the delicate plate, the MCP amplified images are relayed to a phosphor screen with a transparent window within the vacuum chamber so the image can be captured with a digital camera outside of the chamber. With a pinch to pinhole distance of 73 mm and pinhole to MCP distance of 37 mm, the magnification was set to $\sim$ 0.5 with an approximate resolution of 300 μm. The spectroscopic line of sight and framing camera line of sight are co-linear, meaning the 2D structure of the plasma-vacuum boundary surrounding the field of view of the spectroscopic system is directly observable by the imaging system.

Emission from oxygen during stagnation conditions is expected to be brightest between 500 - 600 eV photon energies (see chapter 5). For this reason, metallic filters of specific elements and thicknesses were selected to detect only the bright emission from the stagnated oxygen plasma while attenuating emission earlier in the implosion. The x-ray filters used for the CESZAR oxygen experiments were 3 μm Al, 10 μm Al, 1 μm Cu, and 75 μm Be. To determine 'stagnation time' or 'bang time', the average peak time of all non-saturated diode signals was used. The photodiodes were each biased to 50 V to allow photo-sensitivity. The transient signals of each diode were recorded onto digital oscilloscopes through direct current blocking 'bias Ts'.

3.2.4 Axial Magnetic Field System

To mitigate the magneto Rayleigh-Taylor instability inherent gas-puff implosion on the CESZAR driver, an axial magnetic field system was designed, installed and characterized on the experimental system. The system consists of a Helmholtz coil connected to a pulsed power circuit separate from the CESZAR driver. The Helmholtz coil was made by winding magnetic wire around two sections of a polymer frame and cast in epoxy. The Outer diameter of the coil is $\sim$ 23 cm and inner diameter is $\sim$ 19 cm with a separation between the two coils of 4 cm. An image of the Helmholtz coil is shown in figure 3.20.

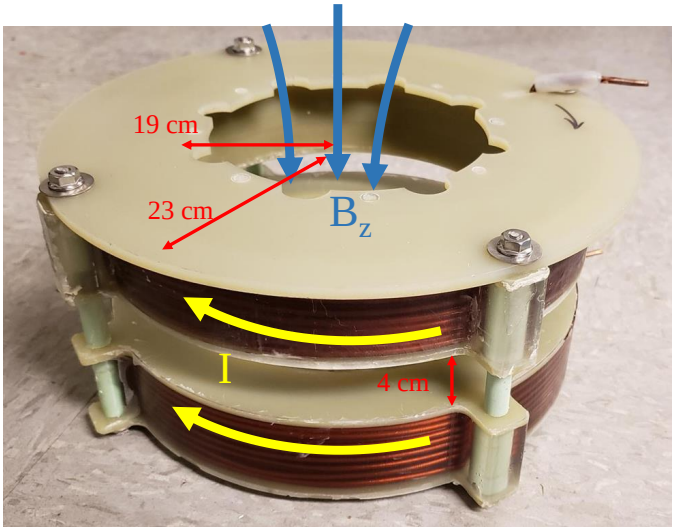

Figure 3.20: Photo of the axial magnetic field Helmholtz coil. The current path through the winding and resulting axial magnetic field as well as approximate coil dimensions are illustrated by the annotations.

The magnetic field generated by the axial magnetic field (AMF) system was first characterized outside of the vacuum chamber using two separate b-dot probes of different sizes. The smaller probe allowed measurement of the spatial dependence of B_z for measurements within the vacuum chamber while the larger probe provided a cross-calibration measurement for the smaller probe. The 'small' b-dot probe loop diameter was 18.55 mm with three turns, while the 'large' b-dot probe diameter was 76.5 mm with 10 turns. The measurements were repeated within the vacuum chamber with all of the electrode and gas-injector hardware installed. The calibration factors used for both b-dots were determined only based on the geometric measurements of the probes. Strong agreement of the measured field between the two probes indicates a high degree of certainty of the magnetic field measurements. Because the load hardware is metallic and therefore highly conductive, the transient response of the magnetic field within the load region is significantly affected. The result is that the peak magnetic field is reduced, and the time elapsed to reach the peak field is delayed. Measurements made in air and within the vacuum chamber in figure 3.21. Because the load hardware prohibited measurements with the large b-dot probe,

only the small probe was used for in-situ measurements. The peak of the the measured axial

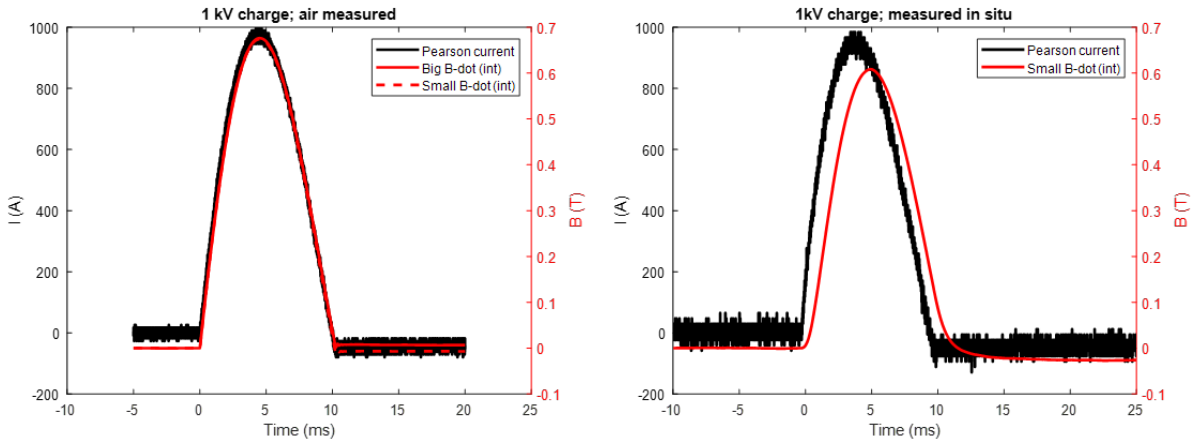

Figure 3.21: B-dot measurements of the axial magnetic field measured outside (a) and inside (b) of the vacuum chamber. In (a) The measured current of the pulsed power system is shown in black and the integrated b-dot signals are shown in red (large b-dot is solid and small b-dot is dashed). Only the small b-dot measurement is shown in figure (b). The current measurements of the pulsed power driver were made using Pearson current monitors.

magnetic field is shifted from ~ 4.7 ms to 5 ms when installed in the vacuum chamber. During experimental plasma shots with the AMF system, the CESZAR trigger is delayed by 5 ms to allow the peak axial magnetic field to be set-up in the load region.

Measurements were repeated at different charge values of the AMF pulser to measure the dependence of the axial magnetic field strength on charge voltage. This allows the selected axial magnetic field strength to be 'dialed-in' by selecting the charge voltage of the AMF pulser before experimental plasma shots. The peak field strength depends linearly on charge voltage, as shown in figure 3.22

The spatial uniformity of the axial magnetic field in the vacuum chamber was also measured by recording over several discharges at three radial positions ($R = 0, 1, 2$ mm from the central axis). Measurements were limited to a radius of 2 cm since the initial gas-puff radial extent is approximately 2 cm. The results of the measured peak field strength for both 1 kV and 0.5 kV charge voltages are shown in figure 3.23. The radial dependence appears independent on charge voltage (and therefore, B_z magnitude) and has a slight dependence on radius with a three

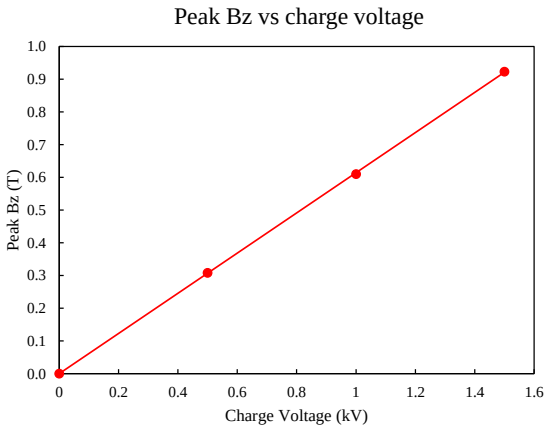

Figure 3.22: Dependence of peak axial magnetic field strength on charge voltage.

percent higher field strength at 2 cm radius than on axis for 1 kV charge. For practical purposes of the experimental and modeling work of the CESZAR gas-puff implosions, the initial axial magnetic field can be considered uniform.

3.3 Gas Injector

3.3.1 Design

The CESZAR gas-puff experiments were carried using a custom designed dual gas injector [88]. The injector consists of two independent plenum-valve-nozzle systems, a central jet (target) surrounded by a annular jet (liner). The plenum of each injection system can be pressurized to the desired value using any chosen gas species. Each valve can be operated independently, so that the relative timing between the two injection systems can be adjusted as well as the timing of each relative to the CESZAR discharge. A cross-sectional diagram of the gas injector is shown in figure 3.24. The valve is operated by electromagnetic action in which the plenum-nozzle interface is normally sealed by disc poppet supported by a compressed ring spring. A wire coil sitting beneath the poppet provides an impulsive force to the poppet when a fast-changing current runs

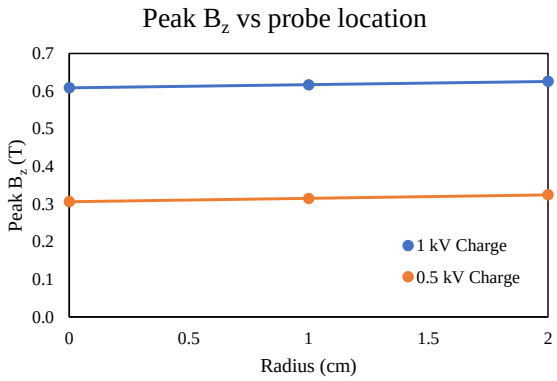

Figure 3.23: Spatial uniformity of the axial magnetic field system. the blue line corresponds to measurements made with a 1 kV charge voltage, and the orange curve represents the 0.5 kV charge voltage measurements.

through the coil, opening the valve during the current pulse. The liner and target valves each contain separate coil-poppet-plenum systems. The current-pulse generators for the liner and target valves consist of capacitor banks charged to $\sim$ 500 kV and produce a peak current of 4.5 kA in $\sim 40\mu s$.

The liner and target injector nozzles were designed with significantly different profile geometries. The target nozzle is a simple straight barrel geometry with a diameter of $\sim$ 1 cm and is 4 cm from the valve to the exit plane. The liner nozzle uses an axisymmetric de Laval profile geometry. The curvature of expansion of the nozzle profile is defined by a pair of polynomial functions symmetric about the throat center radius. This nozzle geometry creates a super sonic flow past the throat, which allows for a low radial divergence of the gas flow past the injector plane into the CESZAR anode-cathode gap.

3.3.2 Characterization

Knowledge of the gas-puff characteristics and properties generated by the gas injector is crucial for carrying out plasma experiments as well as modeling them with MHD simulation packages. The dynamic behavior of the gas-puff implosions heavily depends on the initial radial

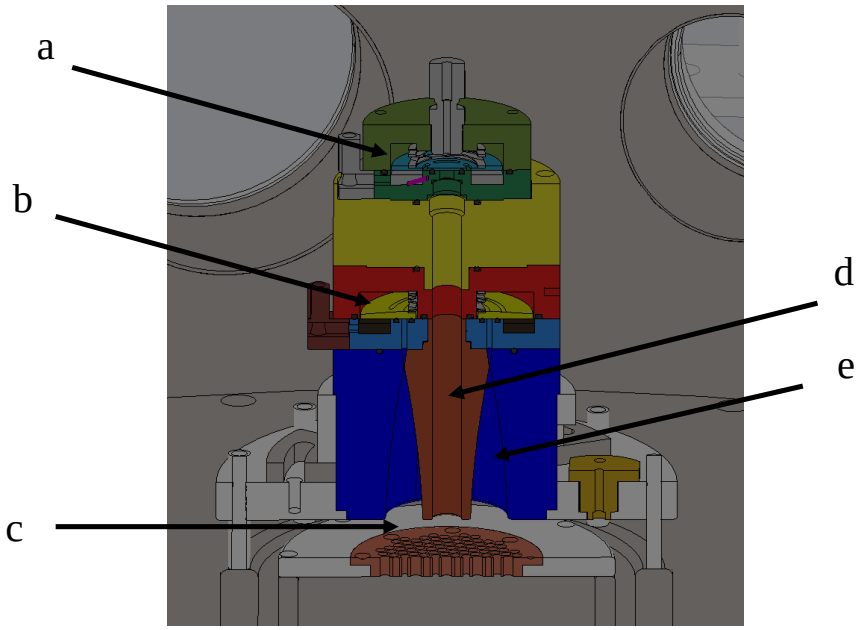

Figure 3.24: Cross section of the gas injector assembly on the CESZAR driver. The labeled points on the figure are as follows: a) target valve plenum, b) liner valve plenum, c) load region and transparent cathode plate, d) target nozzle, e) liner nozzle.

(and sometimes, axial) gas density profile, therefore, any hope of accurately simulating the implosion requires an accurate density profile with which to initialize the problem. Knowledge of the transient flow of the injector and the dependence of the total injected mass on plenum pressure is also important in carrying out controlled experiments. Ideally, measurements of the initial gas-density profile would be made for each individual shot. However, the large length scales associated with the CESZAR chamber, diagnostic access, and mechanical vibrations of the machine make sensitive density measurements impractical or impossible. Instead, the gas injector characterization is carried out on a separate test stand with a smaller vacuum chamber.

The primary method used to measure the initial gas-density profile is a one dimensional Michelson interferometer. An interferometer operates by detecting a phase shift of an interference

pattern due to a change in the relative effective path length of a sample and reference beam. In the case of gas-density measurements, the change in the effective path length of the sample beam is due to the changes in refractive index of the the gas puff which is related to its integrated density along the sample beam path. A diagram of the Michelson interferometer is shown in figure 3.25.

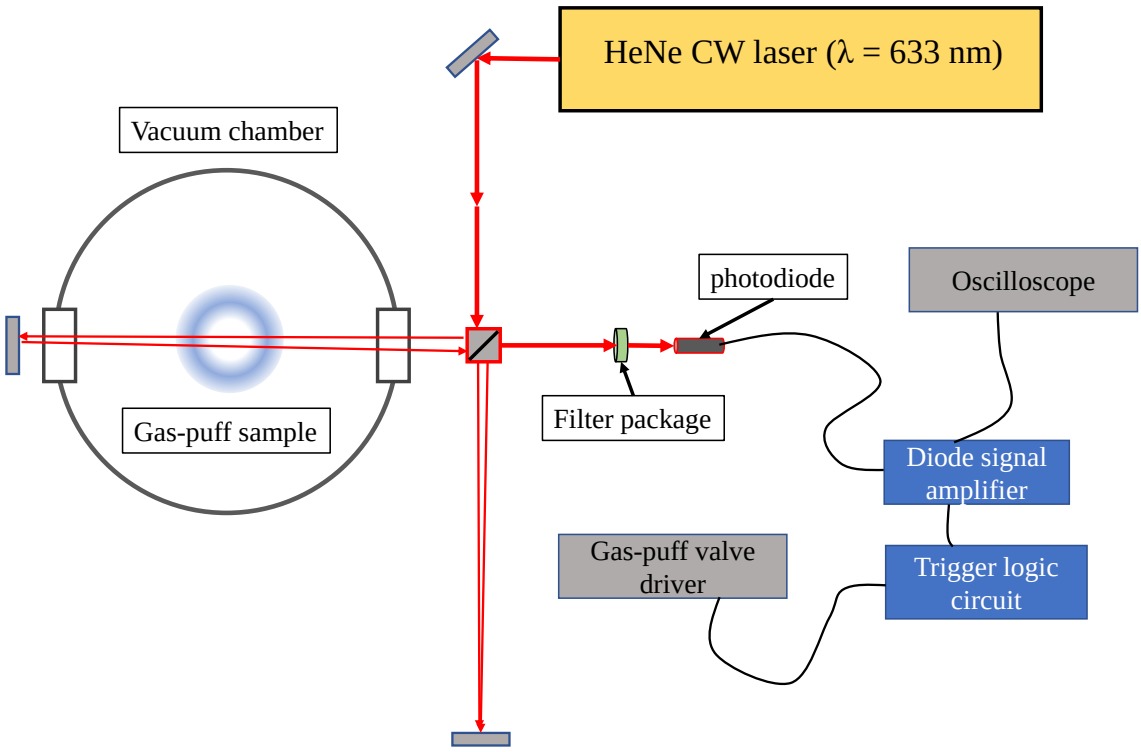

Figure 3.25: Diagram of the Michelson interferometer used for the gas-puff characterization test stand.

The overlapping recombined beams of the Michelson interferometer will exhibit an interference pattern due to a small difference in the intrinsic path lengths of each leg of the system (sample and reference). The one-dimensional 'pencil-beam' arrangement allows for a time resolved measurement of the phase of one fringe to be made using a photodiode. As the effective path length of the sample leg is increased due to the presence of the injected gas, the photodiode will see a corresponding shift in laser intensity as the bright/dark pattern moves over the detector. Because the laser intensity observed by the photodiode leads to a greater

current of photoelectrons (and not a higher voltage), an amplifier circuit is necessary to produce a voltage signal to be read by the digital oscilloscope. In addition, mechanical vibrations of the vacuum system and optical table lead to an irregular background oscillation of the interference pattern seen by the photodiode. This introduces two problems. First, the phase shift associated with background vibrations must be identified and subtracted from the signal. Second, because the instrument sensitivity is optimal between the minimum and maximum signal positions (the detected phase shift occurs near the maximum contrast level), the trigger system must be properly timed with the background vibrations. This is achieved with a trigger logic circuit coupled to the gas-puff valve driver. The raw data obtained by the oscilloscope is shown in figure 3.26.

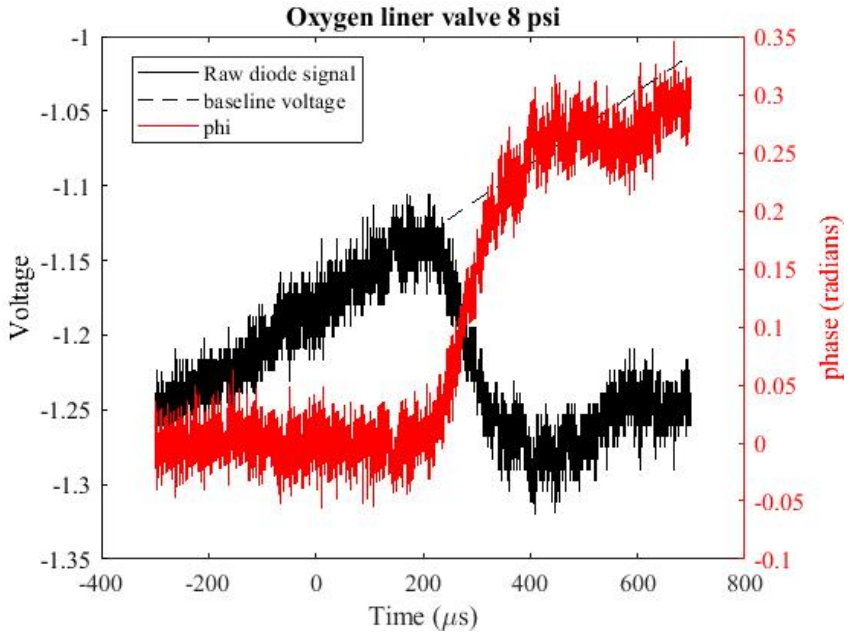

Figure 3.26: Raw data (black) and calculated phase shift (red) for an oxygen gas puff at 8 psi. The background or baseline trend of the voltage signal is

A moderate change of the effective path length of the sample beam will produce a phase shift of that interference pattern. The measured phase shift is proportional to the line integrated density along the path of the laser which is defined in equation 3.3.2.

$$LID = \int_L N(x,y,z)dy$$

Where the beam path, L, is taken in the y direction. The phase shift associated with the density-dependent refractive index along the beam path is then given by equation 3.4

$$\Delta\phi = \frac{2\pi}{\lambda}\int_L n([N(x,y,z)]-1)dy \tag{3.4}$$

The relationship between number density and refractive index of a neutral gas is given by the Gladstone-Dale relation [89].

$$(n_{gas}-1) = (n_0-1)\frac{N_g}{N_0} \tag{3.5}$$

where n_{gas} is the measured refractive index of the gas, n_0 is the refractive index of the gas at standard temperature and pressure (STP), N_g is the number density of the gas, and N_0 is the number density of an ideal gas at STP conditions. The value of n_0 depends on the species and is tabulated in [90]. For Oxygen, $n_0 = 1.000271$, and for helium, $n_0 = 1.000035$.

Using equations 3.4 and 3.5, the line integrated density is determined. The line integrated density and valve driver current are shown in figure 3.27 from measurements made at $x = 0$ (across the center of the gas puff) and $z = 5mm$ from the exit plane of the injector. Measurements of the gas density profile are temporally referenced to the start of the valve driver current pulse as shown in figure 3.27.

Measurements were repeated at $x = 0mm, z = 5mm$ at multiple plenum pressures ranging from 4 psi to 10 psi in the liner, with 5-10 repeated measurements made at each pressure. Separate measurements of the target valve gas-puff were made at $x = 0mm, z = 5mm$ for target plenum pressures ranging from 5 to 30 psi. The relationship between plenum pressure and line integrated density at a given time is linear for both the liner and target valves. Figure 3.28

To construct the entire radial density profile, multiple line integrated density measurements must be made at various chords of the gas column so that an inverse Abel transform can be performed using measurements at each chord. This process is detailed for a gas injector of nearly identical design [88]. Assuming the same shape of the gas density profile for the injector

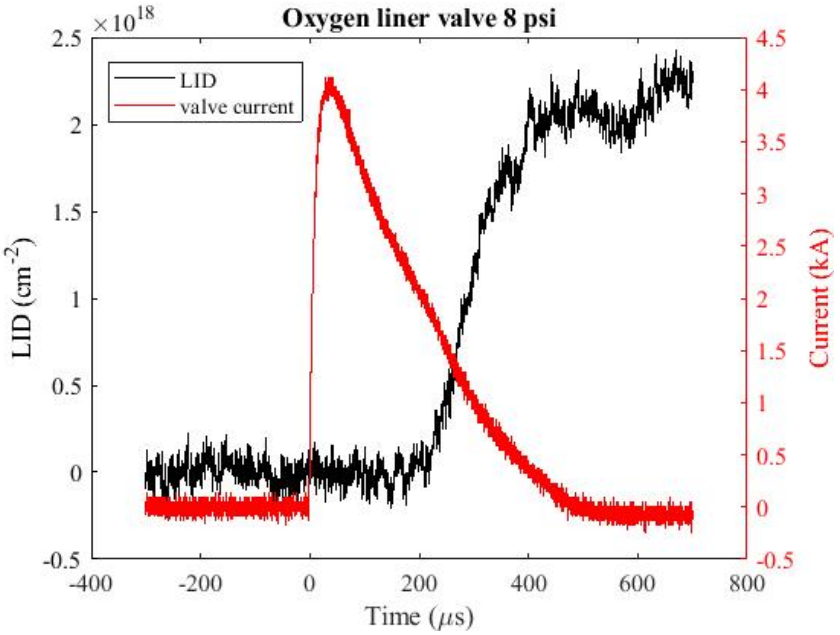

Figure 3.27: Calculated line integrated density (black) and valve driver current (red).

designed for the CESZAR driver, the liner profile can be estimated by scaling the LID using factor approximately equal to twice the average width of the gas puff, which is approximately 2.4 cm.

This process can be repeated for the Helium target valve, which has an approximate with of 1 cm. Although these estimates are based on measurements, the entire gas-density profile is not completely measured. However, the resulting gas-density profiles provide accurate estimates of the total linear mass injected into the load region and are therefore suitable for many MHD simulations. A combined estimated gas-density profile and total linear mass is shown in figure 3.29. The profile was constructed by matching a Gaussian function to the measured density profiles discussed in [88] using the corresponding LID measurements, and appropriate molecular weight of each gas species.

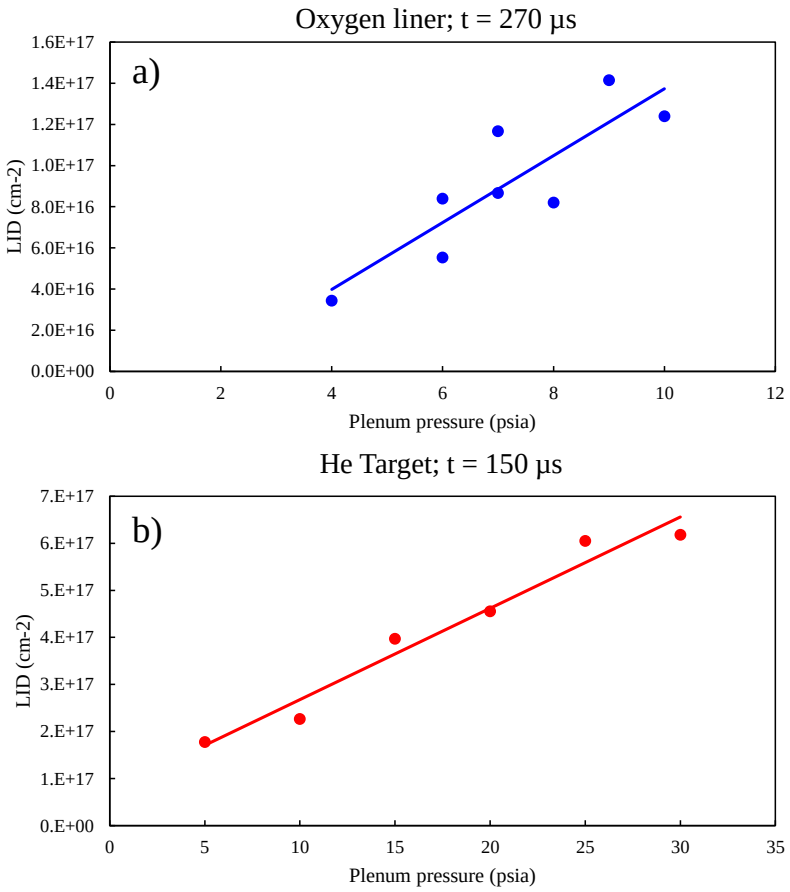

Figure 3.28: Measured LID for both oxygen liner and helium target measurements as a function of plenum pressure.

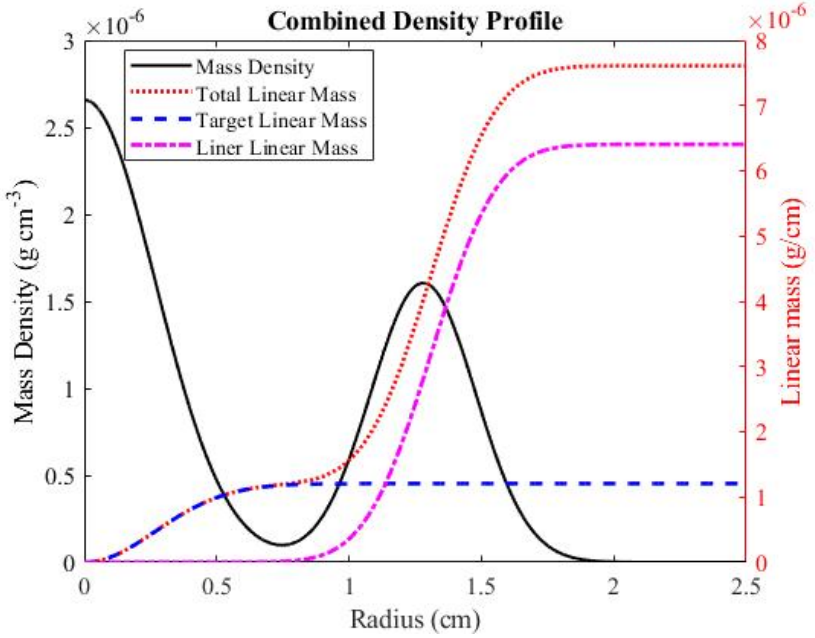

Figure 3.29: Estimated gas density profile for a liner-on-target gas-puff. The combined density profile (black) is expressed in g/cm^{-3}, the combined linear mass (red), liner (magenta) and target (blue) are expressed in g/cm. The gas-puff parameters associated with this profile are an oxygen liner at t = 270 μs, 6 psi and helium target at 150 μs at 20 psi.

Chapter 4

Effects of an Axial Magnetic Field on Current Distribution

This chapter discusses results from experiments carried out at the Weizmann Institute of Science. The machine characteristics and diagnostics used are discussed in chapter 3. These experiments primarily discuss the evolution of the azimuthal magnetic field distribution in oxygen implosions both with and without an axial magnetic field. Measurements are compared with simulations performed in TRAC-II which is described in section 4.1. The dynamics and stability of the implosion across multiple shots is analyzed and discussed. Next, the measured radial distribution of B_θ and its evolution are investigated along with the evolution of the axial magnetic field during the implosion.

4.1 TRAC-II Simulations

Calculations were performed with TRAC-II, a 2D azimuthally symmetric radiation magnetohydrodynamic (MHD) code [91]. In Lagrangian codes such as TRAC-II, mesh tangling can become problematic if MRTI growth is significant. For this reason, the simulations were run in

one-dimensional (1D) Lagrangian mode and were driven by the experimentally measured current waveform. TRAC-II uses the quotidian equation of state model (QEOS) [92]. The QEOS model reduces to the ideal gas law for high temperatures ($T >> T_{melt}$) and low densities ($\rho << \rho_{solid}$). The Lee-More model [92] is used for electrical and thermal conductivities. The Lee-More model for a plasma approximates the Spitzer resistivity with corrections that depend on the magnetic field, the chemical potential, and ionization fraction. A single-group radiation model is used with tabular Rosseland and Planck opacities.

The initial gas density profiles used in the simulations were scaled from interferometric measurements of argon gas puffs, the process of which is described in [93]. Since mass density profiles were not characterized for O_2, MHD simulations were initialized assuming a similar profile structure. To estimate the appropriate initial density profile, the argon measured profile was scaled so that the simulated peak compression time approximately matched the stagnation time observed in experiment. This was achieved with an initial linear mass density of $\sim 1.2 \times 10^{-5}$ g/cm.

4.2 Dynamics and Stability of WIS Implosion

The images obtained from the time-gated ICCD provided measurements of the outer plasma radius in the visible range and instability growth over the course of the implosion. An example of such images is presented in figure 4.1, where the right four images featured the applied axial magnetic field, and the left four did not. Qualitatively, the images for the case with initial axial magnetic field (B_{z0}) show no significant growth of current driven instabilities or the magneto-Rayleigh-Taylor instability and present a roughly uniform plasma column near stagnation. On the other hand, instability growth is clearly apparent in images where $B_{z0} = 0$. The absence of instability mitigation reduces the shot to shot reproducibility of the implosion.

Combining data from dozens of shots provides an evolution of the radius for all observed

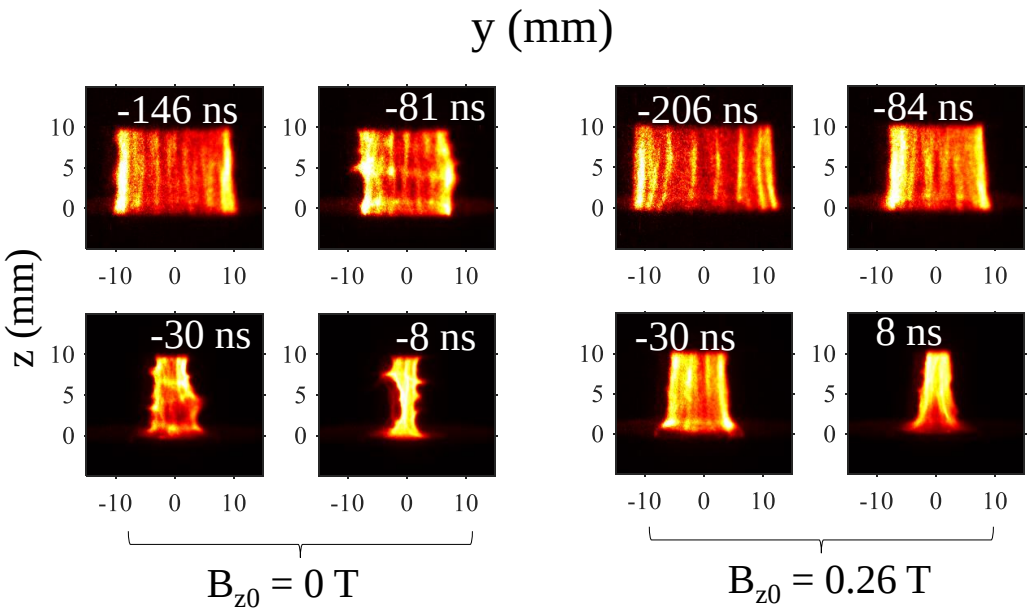

Figure 4.1: Images obtained from the time-gated ICCD for eight shots, each taken at different times relative to the pinch. The left four images correspond without B_{z0} and the right four with B_{z0}. The z = 0mm position corresponds to the edge of the nozzle injector (anode).

z positions with and without external applied B field, as shown in figure 4.2. Measurements of the outer plasma radius were made by axially integrating the intensity from z = 3 to 9 mm from the anode to avoid edge effects observed near the injector nozzle at $z < 3mm$. The outer plasma radius is defined by the full width at half maximum intensity of the horizontal lineout of the image. These data are compared with the one-dimensional simulation results from TRAC-II. The simulation peak compression (the point in time during the simulation characterized by a minimum outer radius) occurred at 682 and 673 ns for cases with and without B_{z0}, respectively. The experimentally determined stagnation times agreed well with the simulations, occurring at 697 ± 15 ns in the cases with B_{z0}, and 660 ± 15 ns without. The times reported in Fig. 5 are referenced to the stagnation time for each respective shot. Note that the peak photodiode signal coincides with the minimum plasma radius to within 10 ns.

The simulations with $B_z = 0$ show a minimum radius of $\sim 0.5mm$, a significantly lower value than measurements made near stagnation time. Measurements of the plasma radius taken

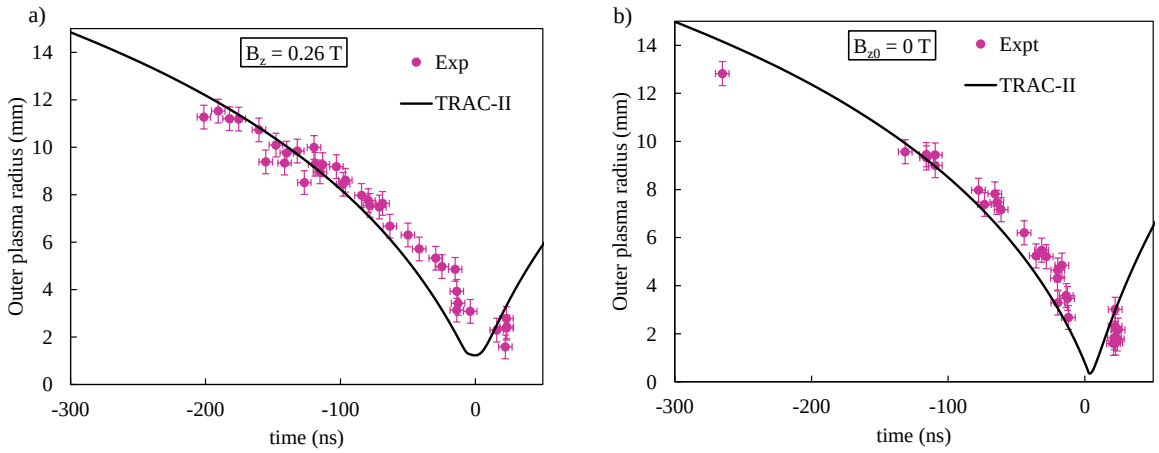

Figure 4.2: Implosion trajectories for cases with and without initial axial magnetic field. Each data point is taken from a separate shot and axially integrated between 3 and 9 mm from the anode. The horizontal error bars correspond to the 5 ns integration time of the detector while the vertical error bars account for the resolution limitation of the imaging camera. The solid curves represent the motion of the outer plasma radius from the TRAC-II simulation results.

from several shots within ±25 ns of stagnation produced an average value of 2.9 ± 1.2 mm (1 σ) for $B_z = 0$ and 3.2 ± 1.1 mm (1 σ) for $B_z = 0.26T$. Considering that the measurements of the outer plasma radius were made with $\sim 6mm$ axial integration, any present instability structures were averaged over when determining the outer plasma radius from the images. Since the 1D simulations cannot incorporate instabilities present in the experiment, the compression is overestimated, resulting in the smaller minimum radius. Overall, the implosion dynamics is well captured by the 1D simulations considering the overall implosion trajectory. However, the measured outer radius is consistently larger than simulation predictions by 1.25 mm on average between -60 and 0 ns. While the evolution of the plasma dynamics is overall well reproduced by the TRAC-II simulations, it is important to keep this discrepancy in mind when comparing $B\theta$ measurements to simulations in section 4.4. Comparison between experimental data and simulation results suggests that some additional effects, besides counterpressure of B_z, are slowing down the plasma implosion. Additionally, the uncertainty in the estimated initial mass density profile used to initialize the simulations may be partly responsible for the discrepancy between experimental and simulated implosion trajectories.

4.3 Evolution of B_θ at the plasma-vacuum boundary

This section discusses the evolution of the azimuthal magnetic field at the outer edge of the plasma, corresponding with the radii discussed in 4.2 and shown in figure 4.2. The evolution of the measured azimuthal magnetic field (B_θ) is shown in Fig. 6 for the cases with and without B_{z0} and compared to the values of B_θ calculated using Ampere's law:

$$B_\theta = \frac{\mu_0 I}{2\pi r_0} \tag{4.1}$$

where I is the circuital current measured with the B-dot probe and r_0 is the measured outer plasma radius as defined by the outermost radial position at which the spectroscopic measurement could be made. The horizontal position of the measured values of B_θ corresponds to the time relative to stagnation at which the spectral measurement was taken. For ease of viewing, the range of calculated B_θ values are presented as wide gray curves shown in figure 4.3 All data points presented in figure 4.3 were calculated using a spectral outline taken within 0.5 mm of the measured outer plasma radius.

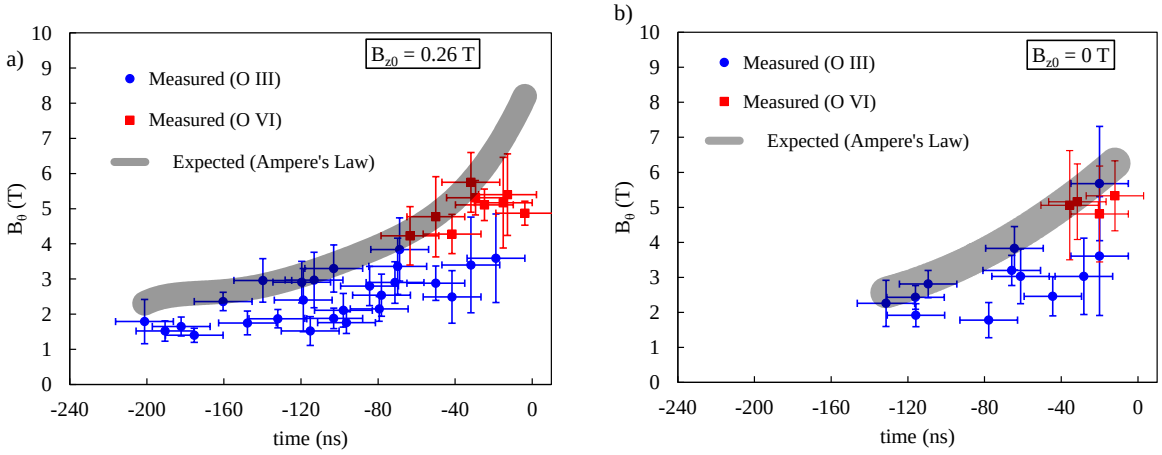

Figure 4.3: Evolution of B_θ at the outer plasma radius for the cases (a) with a preembedded axial magnetic field and (b) without a pre-embedded axial magnetic field. The expected (Ampere's law) curve represents the range of calculated values of B_θ based on the B-dot measured current and outer plasma radius at the time of the B_θ measurement. The horizontal error bars correspond to 30 ns integration time of the detector.

While we can see in Fig. 6 that many points agree with the expected results, indicating that all of the current is flowing within those radial positions, several experimental values of B_θ remain lower than calculated. It is possible that a fraction of the current is carried by peripheral plasma at radii greater than the apparent plasma-vacuum boundary at which the spectroscopic measurement was made. It has been seen in references [11,13,23] that there exists a radial ionization state distribution. The charge-state distribution observed in our plasmas shows that higher ionization states reside at larger radii. As the implosion progresses, the ionization state distribution evolves, and emission from O VI is observed in B_θ measurements past 60 ns prior to the stagnation time with or without initial Bz0, as seen in Fig. 6 (red square data points). The O VI emission also provided B_θ values similar to the ones expected according to Ampere's law, while O III emission mainly shows points below the expected B_θ values. However, when only O III was observed on the B_θ spectrometer, the spectrometer dedicated to Te measurement detected O IV and O V lines at radii beyond the apparent outer edge of the plasma. This observation indicates that a plasma composed of higher ionization states at larger radii is carrying part of the current, which explains the lower than expected B_θ values found for O III in figure 4.3 Note that the highest "expected" values shown in Fig. 6(b) are less than the highest expected values in Fig. 6(a), even though a smaller minimum radius is expected where $B_{z0} = 0$. This is due to the fact that the data collected for cases where $B_{z0} = 0$ were not taken as close to stagnation as some of the $B_{z0} = 0.26$ T data.

In cases where O VI is apparent on the B_θ measurement, the measured values of B_θ inferred from the O VI emission line are in good agreement with the calculated values until within ~ 20 ns of the pinch, indicating that the current is, in those cases, fully flowing within the outer edge defined by the imaging camera until times near stagnation where potential higher ionization states might exist.

Finally, it is important to note that during this experiment we did not observe significant differences between expected and measured B_θ for the case with initial $B_{z0} = 0.26$ T and for the case without B_{z0}, as can be seen in figure 4.3 However, in reference [65] the effect of the axial

magnetic field on a similar experiment has shown a stark contrast between discharges with and without B_{z0}. The results shown in reference [65] indicate that a low-density peripheral plasma was responsible for current loss in the imploding plasma. According to reference [65], the low-density peripheral plasma may have been the result of discharged material introduced from the pulsed Helmholtz coils within the vacuum chamber. It was noted that placing the Helmholtz coils outside of the vacuum chamber helped to mitigate the development of low-density peripheral plasma and the subsequent current losses. To minimize such losses, the data gathered for the present paper were collected using outwardly located Helmholtz coils. As a result, we observed no significant difference between the measured and expected values of B_θ both with and without $B_{z0} = 0.26$ T. In addition to the location of the Helmholtz coils, performing several "cleaning" discharges of the Z-pinch current driver both with and without B_{z0} can help to liberate and remove contaminants present on the surfaces of the current driver electrodes which is also important in mitigating current losses.

4.4 Radial Distribution of B_θ with and without B_{z0}

To further understand the current distribution in imploding gas-puff Z pinches, we utilize the ionization state distribution to construct a radial profile of the azimuthal magnetic field. Between ~ 80 and ~ 20 ns prior to stagnation, we have simultaneously observed emission from O III $3s^3P_2 - 3p^3D_2$ and O VI $3s^3S_{1/2} - 3p^2P_{3/2}$ whose edge of emission appeared at different radii. Figure 7 shows the experimental B_θ values for a given shot at different radial positions compared with simulated B_θ radial distributions. Each color corresponds to a point in time relative to pinch, both for experiment and simulations. The wide gray curve represents the expected B_θ according to Ampere's law for the range of current values associated with each data point and values of the outer plasma radius. The dashed lines in figure 4.4 connect two measured values obtained from the same shot.

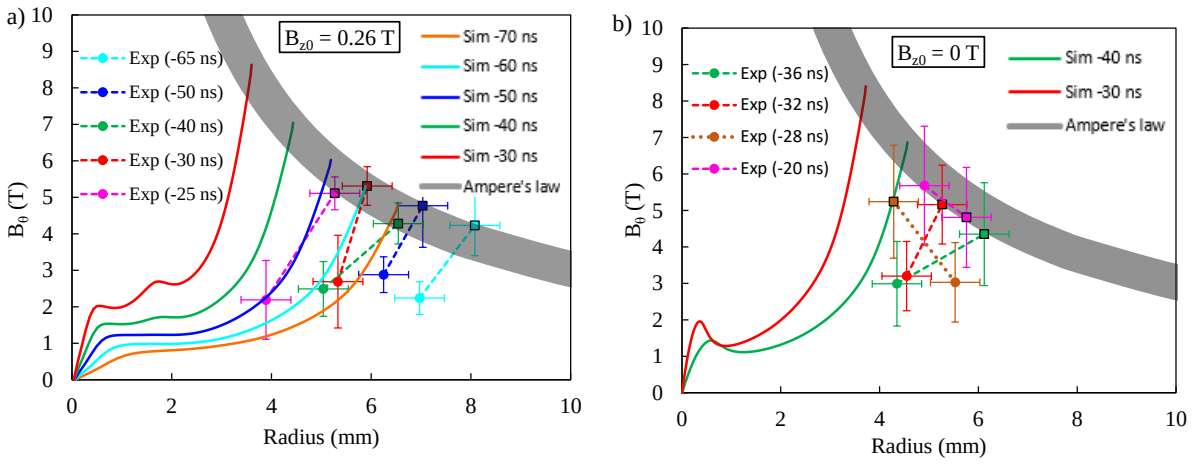

Figure 4.4: Measured (dashed lines with points) and simulated (solid lines) radial profiles of the azimuthal magnetic field for various points in time for experiment and simulation with (a) axial magnetic field and without (b). The wide band of the gray curve denoted as "Ampere's law" is such to account for the range of current values measured for all discharges. Circular points were measured from O III, while square points were measured from O VI.

In all presented cases, the outer plasma radius as measured by the imaging camera typically lies between the emission edges of O III and O VI, with the latter almost always located further out. Note that for each of the cases shown, the outermost measurement taken at the edge of the O VI emission corresponds to the value expected at that radius given the B-dot current measurement using Ampere's law.

In the case with an externally applied axial magnetic field [figure 4.4(a)], the measured B_θ profiles are lower than the simulated values for each given time and systematically appear at greater radii, resulting in an apparent time shift between measured and simulated profiles in figure 4.4(a). For example, the measured profile at -30 ns (red data points) matches the simulation profile around -60 ns. The simulations have been shown in section 4.2 to over-predict axially averaged plasma compression at times between -70 and 0 ns. Because of this overestimation, the simulated plasma radius is smaller than the measured values, and the corresponding values for B_θ are necessarily over-predicted. Since all of the measured radial profiles of B_θ were taken later than -70 ns, this discrepancy between simulation and experiment is apparent for all profiles shown in figure 4.4(a). Looking past this discrepancy, the measured B_θ data accurately follow

the same profiles as the simulation results. Overall, this means that the physics of these pinches with B_{z0} are well captured by 1D MHD calculations. Implosions with $B_{z0} = 0.26T$ also indicate a high degree of azimuthal symmetry and an accurate model of magnetic diffusion.

Experimental data confirm a high degree of azimuthal symmetry where $B_{z0} = 0.26T$. Values of B_θ measured at the opposite azimuth differed on average by only 18% for discharges where $B_{z0} = 0.26T$ and differed on average by 32% with no axial magnetic field. It should be noted that the emission intensity is highly asymmetric when $B_{z0} = 0$, often resulting in a higher uncertainty of B_θ measured from the opposite azimuth. In addition, the model of magnetic diffusion is further verified by agreement between experimental and simulated resistivity values. Mass averaged resistivity values obtained from 1D simulations were of the order $1 \times 10^{-5}\Omega m$, while the Spitzer resistivity value for the estimated plasma temperature of 10 eV during the implosion phase of the experiment was $1.8 \times 10^{-5}\Omega m$. Line intensity ratios of O III to O V transitions provide an estimate of Te between 8 and 12 eV during the implosion phase based on Saha equilibrium. The skin depth associated with this resistivity value and the current driver frequency is $\sim 5.2mm$, in good agreement with the apparent current sheath thickness presented by the measured B_θ profiles.

In the case with no axial magnetic field, the measurements and simulations do not, in general, agree. The radial distribution inside the plasma does not follow the same shape as the case with the pre-embedded axial magnetic field and is not consistent between discharges. Non-monotonic distributions of B_θ have previously been observed in implosions without axial magnetic field stabilization in reference [66] where it has been proposed that this observation may be due to flaring of the plasma caused by instability structures. While this may be the case in the experiment presented here, such large flaring seen in reference [66] was not observed for the discharges presented in figure 4.4(b). In our experiment, it is not certain that the diagnostic method is entirely valid where MRTI is present.

This diagnostic technique assumes that the magnetic field is parallel to the line of sight.

The validity of this assumption requires that the data are taken at the edge of the emission of a particular line. It is important to remember that all measurements presented here are integrated along the line of sight. In cases where hydrodynamic instabilities are present, it is conceivable that the complex three-dimensional structure of such instabilities may lead to collection of emission from plasma protruding at adjacent azimuthal positions, partially invalidating this important assumption.

In addition, spatial gradients may induce a non-homogeneous charge-state distribution affecting the current path. In fact, in one case shown in 4.4(b), at -28 ns, the charge state distribution is reversed, with O III appearing at a larger radii than O VI. In this case, the peak magnetic field strength appears at a smaller radius than the measured outer radius. A possible explanation for this phenomenon, assuming that the measurement is valid, is that hydrodynamic instabilities cause regions of plasma to displace one another, not only reversing the charge-state distribution locally, but transporting magnetic flux inward, creating an inverted magnetic field distribution on the spatial scale of the measurements ($\sim 3mm$). Furthermore, the MRT instability structure will likely result in an axially dependent radial distribution of the current, and thus of B_θ, where MRT structures are pronounced. More experimental data would be required to investigate this interesting phenomenon further. For example, duplicating diagnostic systems to simultaneously measure B_θ from multiple azimuthal positions would provide more clear information on the azimuthal asymmetry.

4.5 Measurements of B_z evolution

The axial magnetic field measurements were made by emission from a laser produced Al plasma using direct Zeeman splitting of the Al-III $4s^2S_{1/2} - 4p^2P_{1/2}$ transition. All measurements were spatially resolved along the radius, integrated along the line of sight and time gated. Measurements were made at multiple axial positions during separate shots. The measured values

of B_z are shown in figure 4.5

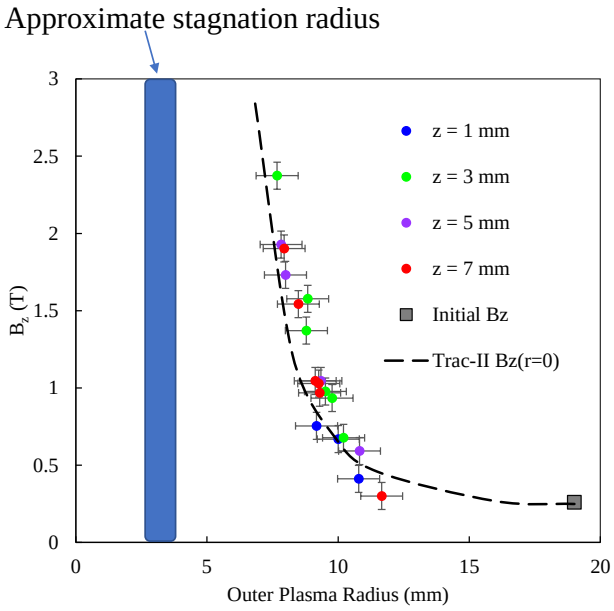

Figure 4.5: Experimental measurements of B_z and TRAC-II simulation results of the evolution of B_z at $r = 0$. The data was collected from various axial positions indicated by the colors shown in the legend. The Approximate radius of the final stagnated plasma radius is shown by the blue region.

As the implosion progresses, the outer plasma radius decreases while the plasma and axial magnetic flux is compressed, resulting in greater measured values of B_z later in the implosion. Measurements were limited to ~ 100 *ns* prior to stagnation due to continuum emission overwhelming the emission from the Al plasma. Figure 4.5 shows relatively good agreement between 1D MHD results and experimental measurements, indicating again that the plasma resistivty and magnetic diffusion is well modeled by the Lee-More model and by TRAC-II in these implosions.

Later in the implosion, the axial magnetic field near the anode may inhibit the radial compression of plasma due to the flux 'frozen-into' the rigid metallic injector nozzle. This effect can be seen in the images of figure 4.1 near the z = 0 positions. Figure 4.6 displays the implosion trajectories measured at both z = 7 and 1 mm from the anode (injector exit plane). The lesser degree of compression is pronounced in the trajectories where $B_{z0} = 0.26$ while where $B_{z0} = 0$,

the dependence of the implosion on z is less well defined.

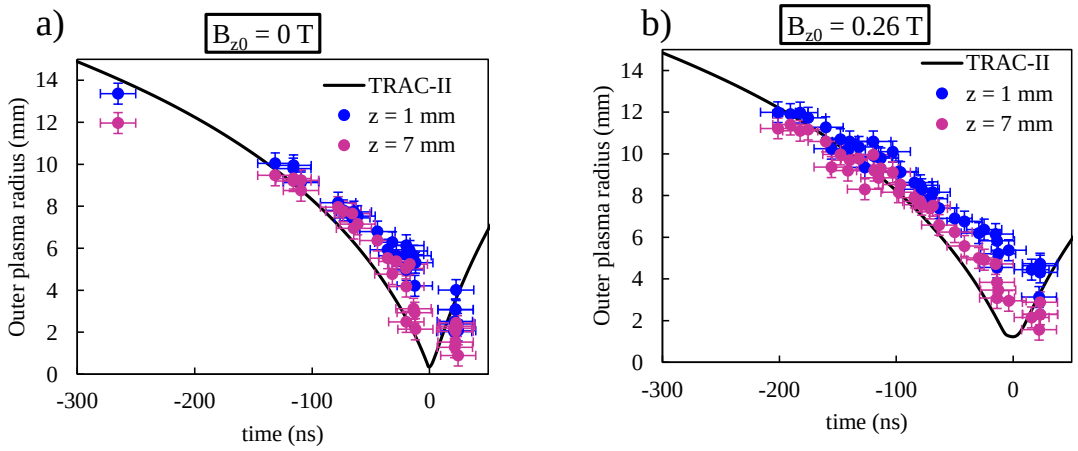

Figure 4.6: Implosion trajectories for both z = 1, and 7 = 7 mm for $B_{z0=0}$ (a) and $B_{z0=0.26T}$ (b). Measurements made at 3 and 5 mm were omitted for clarity as those data follow the same trend as measurements from z = 7 mm.

It should also be noted that the TRAC-II simulations predict a uniform expansion or 'rebound' of the plasma following the peak compression. Images recorded during the experiment post stagnation do not typically follow this trend. Instead, the plasma typically appears disrupted and unstable at these times and the 1D MHD simulations are not reliable in predicting the plasma dynamics at these times.

4.6 Conclusion

The measured evolution of B_θ at the outer plasma radius gave valuable insight about the current distribution, confirming work from previous studies that nearly all the current flows within the plasma radius defined by the higher ionization state emission which is not always visible with diagnostics such as a simple imaging camera. Our results show the importance of defining the ionization distribution over time in Z-pinch plasma experiments in order to determine the current distribution more accurately.

We compared the measured B_θ radial distribution with and without initial magnetic field and showed that better qualitative agreement between the MHD simulations and experimental results is found in the implosions where $B_{z0} = 0.26T$ than where $B_{z0} = 0T$. Still, we observed an apparent discrepancy between the experimental data and the simulations due to the overestimation, by the latter, of the plasma compression in the final $\sim 70ns$ of the implosion. However, the measured B_θ profiles without B_{z0} were not well reproduced by the simulations since the inhomogeneity of the plasma caused by instabilities is not produced in 1D simulations. In such cases, the analysis of B_θ measurements becomes increasingly complex and may require more data to accurately capture the plasma dynamics. While the implosion trajectories exhibit good reproducibility both with and without B_{z0}, the contrast between the clear behavior of the B_θ radial distribution when B_{z0} is applied and its low reproducibility without B_{z0} emphasizes the importance of stabilization in Z-pinch implosions for such measurements. Further investigation will require 2D simulations to address the development of MRTI and its effect on the magnetic field distribution in the plasma.

4.7 Acknowledgements

Chapter 4 includes material as it appears in "Azimuthal magnetic field distribution in gas-puff Z-pinch implosions with and without external magnetic stabilization", N. Aybar, M. Dozieres, D. B. Reisman, M. Cvejic, D. Mikitchuk, F. Conti, E. Kroupp, R. Doron, Y. Maron, and F. N. Beg, Phys. Rev. E, **103**, 053205 (2021). N. Aybar was the primary author of this paper.

Chapter 5

Dependence of Plasma-Current Coupling on Current Rise Time

This chapter will discuss the measured plasma-current coupling on both the WIS driver and CESZAR linear transformer driver. The two machines exhibit similar peak currents, $\sim 300kA$ at WIS, and $\sim 500kA$ on CESZAR but with dramatically different rise times (1500 ns on WIS and 180 ns on CESZAR). It should be noted that the WIS experiments were conducted with an implosion timescale near 700 ns, while CESZAR implosions occur ed in about 200 ns. An example of the current profiles and photodiode signals are juxtaposed together in figure 5.1. Besides the current drivers, the experiments are set up similarly, both using annular oxygen gas-puffs and utilizing the same emission lines for spectroscopic measurements.

The measured plasma-current coupling is measured on both drivers by comparing spectroscopic measurements of the magnetic field with total current measurements and imaging. To simplify the comparison, the data discussed in this chapter is limited to hollow shell implosions with no pre-embedded axial magnetic field. This study aims to understand the impact of pulsed power driver parameters on plasma-current coupling, especially since linear transformer drivers have not been studied in detail as gas-puff Z-pinch drivers. The discrepancies in results between

the two drivers is discussed

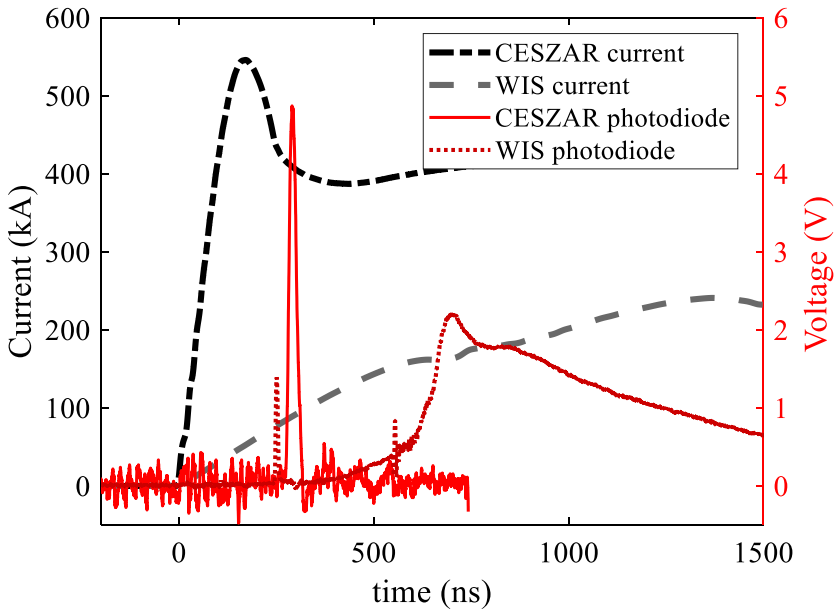

Figure 5.1: Current profiles and photodiode response signals for both the CESZAR and WIS drivers. The CESZAR photodiode shown was filtered with a 3 μm Al foil and is sensitive to photon energies between 500 and 1500 eV, though bright K-shell emission for O is expected near 570 eV. The photodiode used on the WIS driver is sensitive to the UV-visible range.

5.1 Plasma Current Coupling in Both Experiments

The spectroscopically determined values of the azimuthal magnetic field for both the CESZAR and WIS experiments are shown in figure 5.2. To examine the plasma-current coupling during the implosions, the measured values of B_θ are shown alongside their corresponding 'expected' values, represented by the wide gray curves in figure 5.2. The calculated values are obtained using Ampere's law applied to a cylindrical conductor:

$$B_\theta = \frac{\mu_0 I}{2} 2\pi r_{spect} \tag{5.1}$$

Where I is the total current measured by the b-dot probes at the time of the spectroscopic

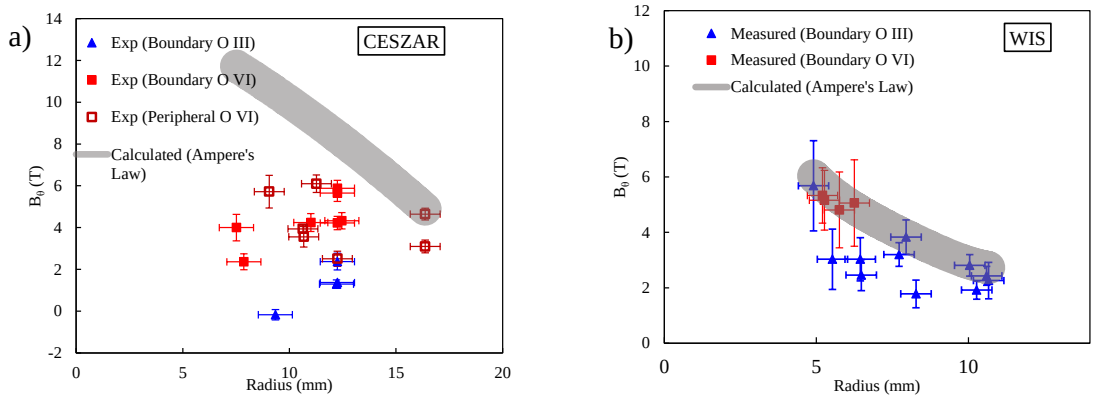

Figure 5.2: Results from the CESZAR (a) and WIS (b) experiments. The individual data points represent values of B_θ measured experimentally using line emission from the labeled charge states. For ease of viewing, the range of calculated values corresponding to each measured point are represented by the wide gray curve.

measurement, and r_{spect} is the radius at which spectral data is selected. The spectral data is selected at the largest radius possible which results in a measurement of B_θ where the uncertainty is less than 30%. Experimental results are presented using 'pinch-relative' timing, meaning that t = 0 ns corresponds to the stagnation time of the experiment, when the peak signal is detected on the photodiodes.

Comparing measured values of B_θ to values calculated with equation 5.1 indicates how much driver current is within the plasma at the selected radius. It should be noted that, for the purpose of clarity, the 'calculated' curves in figure 5.2 are made of a collection of calculated values from separate shots, each corresponding to a measured value; the curves shown therefore do not necessarily exhibit an r-1 dependence of B_θ since the current may change rapidly in the implosion. The data shown in figure 5.2 labeled 'boundary' exclusively contains results for which r_{spect} coincides with the outer plasma radii as determined by the peak intensity gradient observed with the fast-framing camera (r_{image}), within ± 0.7 mm. Conversely, the data labeled 'peripheral' contains data where r_{spect} lies beyond r_{image}. Emission from O VI is sometimes observed extending to radii greater than r_{image} for CESZAR discharges. This type of data

($r_{spect} > r_{image}$) was not observed in the comparable WIS experiment. Still, figure 5.2 shows that for many of these cases, the total circuital current is still not accounted by measurements made using the O VI transition except for the points seen at $\sim 16mm$ for which $r_{image} \approx 7mm$.

The ratios of the measured values of B_θ to the calculated ones for both WIS and CESZAR experiments are displayed in figure 5.3. The results show therein are exclusively where $r_{spect} \approx r_{image}$. While the variation in plasma-current coupling is large in both cases, the CESZAR data clearly fall below the WIS data, with a maximum of $\sim 75\%$ obtained early in the implosion phase at a relatively large radius, while the WIS data consistently exhibit plasma-current coupling near 100% relatively late in the implosion phase when the plasma reaches 5 mm radius. The average plasma-current coupling for WIS were 75% ± 18% and 95% ± 6%, for O III and O VI measurements, respectively. The values for CESZAR were 15% ± 13%, and 48% ± 18%, for O III and O VI measurements, respectively.

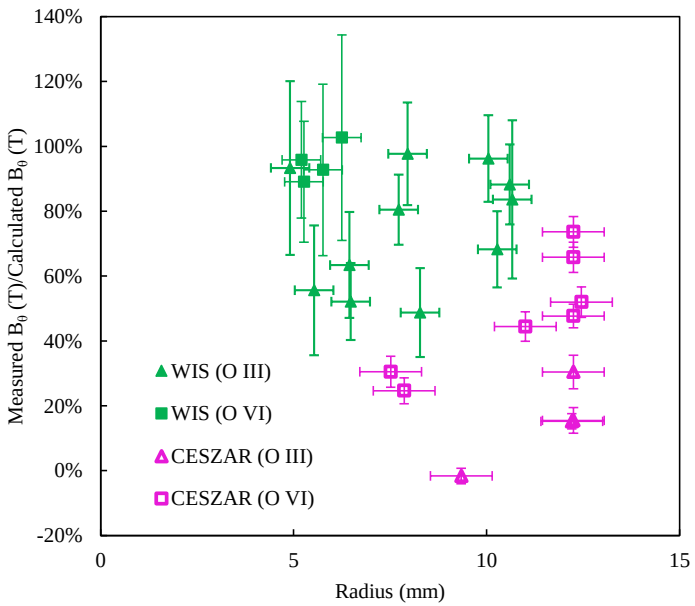

Figure 5.3: Ratios of measured/calculated values of B_θ for both WIS and CESZAR experiments. Measurements made from O III emission are displayed as triangles while O VI are displayed as squares.

In contrast to the WIS results, the CESZAR data shown in figure 5.3 show an apparent

trend as the implosion progresses. The plasma-current coupling decreases as the implosion progresses from large radius to small radius. This trend is apparent for both data measured with O VI and O III. This means that as the imploding plasma moves radially inward, a significant portion of the current remains at a greater radius, presumably being carried by plasma not 'swept up' in the implosion or trailing low density plasma. This trend may provide a clue in understanding the cause of low plasma-current coupling in the CESZAR experiments.

To understand the observed current loss from the imploding plasma driven by the CESZAR current driver, some possible explanations are considered. First, the possibility of current shunting across MRTI structures is discussed and second, the radial charge state distribution is discussed.

5.2 Magneto Rayleigh-Taylor Instabilities

One potential explanation may be that the current is shunted across the bubbles formed at the plasma-vacuum boundary due to the magneto Rayleigh-Taylor instability (MRTI) on implosions driven CESZAR. Because of the faster current rise-time of the CESZAR experiment, the plasma is accelerated at a significantly greater rate than in the WIS experiment. Average acceleration values calculated using implosion times and velocities obtained via imaging yield approximately $5.4 \pm 2.8 \times 10^8 km/s^2$ on CESZAR, and $6.8 \pm 0.5 \times 10^7 km/s^2$ at WIS. This may lead to a greater growth rate, γ, of the MRTI during the implosion phase given its dependence on g (acceleration) in the following expression for amplitude growth of MRTI perturbation of wavenumber k:

$$\gamma_{MRT} \propto \sqrt{gk} \tag{5.2}$$

The average implosion velocity can be estimated using the three images provided by the XUV framing camera in the CESZAR experiment and is typically between 100 km/s and 150 km/s. Analyzing the Doppler shifted line-profiles obtained on CESZAR also yield implosion velocities in the same range. By comparison, the average WIS implosion velocity is near 45 ± 2.5 km/s.

The images also directly provide information of the stability of the plasma-vacuum boundary. An example of the plasma images produced on CESZAR are shown in figure 5.4. Shown are two sets of images from two separate shots, a-c, and d-f, respectively. The frames shown in figure 5.4b, and 5.4d were acquired during the same window that the spectrographic image is taken; thus, the field of view of the spectrometer is illustrated by the blue circles shown in figure 5.4b, and 5.4d with the selected region used to measure B_θ highlighted in green.

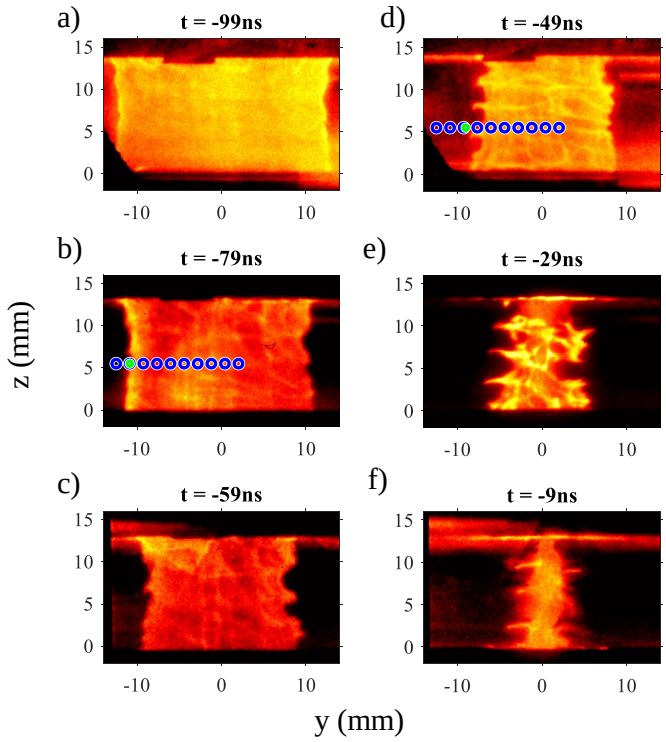

Figure 5.4: Time-gated XUV images of a CESZAR O_2 implosion. Figures a-c and d-f are from separate shots of similar conditions, but with different diagnostic timings. Parts b and d illustrates for each shot the field of view of each fiber seen by the spectrometer with the blue circles. The region selected for analysis is highlighted in green.

The relatively low degree of MRTI development seen in figure 5.4 b is typical of the CESZAR data presented here where $r_{image} \approx r_{spect}$. Even though the CESZAR imploding plasma reaches significantly greater (2-3 times) radial velocities than on the WIS driver, at the time the spectroscopic data is obtained at r_{image}, the MRT instability has not yet substantially grown.

While the WIS data discussed here exhibits a higher degree of stability than the CESZAR results shown, recent work discussed in [66] exhibits a high degree of MRTI and strong axial gradients or flaring; yet measurements of B_θ at the outer plasma boundary (r_{image}) still show close to 100% plasma-current coupling.

However, where $r_{spect} > r_{image}$, later in the CESZAR implosions, MRT instability structures have grown substantially and are shown in figure 5.4, d-f. In this case, emission from O VI remains beyond the MRT structures and B_θ measurements there yield plasma-current coupling near 50%. Therefore, the relatively low plasma-current coupling observed on the CESZAR driver cannot be attributed to shunting across MRTI structures.

5.3 Radial Charge State Distribution

A second time-gated spectrometer with a greater spectral range was also employed during the WIS experiment. When only O III was observed with the B_θ spectrometer, this wide-range spectrometer often observed emission from O IV and O V just beyond the bulk plasma radius, and just beyond where the B_θ measurement could be made using the O III transition observed with the B_θ spectrometer. Figure 5.5 and figure 5.6 shows an example of such a case, where $r_{image} = r_{spect} = 9mm$ yet emission lines from O V were observed up to $\sim 11mm$. When low plasma-current coupling is measured via an O III transition, this plasma consisting of higher charge states residing beyond r_{image} presumably carried a substantial fraction of the total current.

For both experiments, higher charge states appear at greater radii than lower charge states. This is apparent in the WIS experiment both on the B_θ spectrometer and the wide-range spectrometer. On CESZAR, emission from O III is always observed at a smaller radius than where O VI is observed. Given the greater current level reached in shorter times in the CESZAR experiment, we can expect to reach higher temperatures, and therefore higher ionization states in CESZAR implosion than in WIS implosion. This is consistent with the fact that emission from

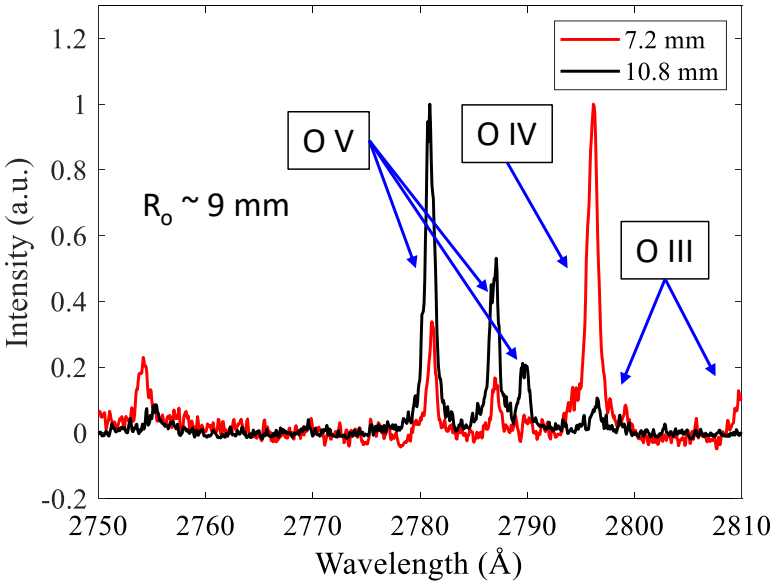

Figure 5.5: Radially resolved Spectroscopic data obtained from the WIS experiment observing a wider spectral range in second order. Shown are the spectra taken at two radial positions surrounding the outer plasma radius r_{image} where $r_{image} = 9.0mm$. The charge states of the identified spectral lines are displayed.

O VI appears relatively early in the CESZAR implosions, as early as 100 ns prior to stagnation, contrasted with 30 ns prior to stagnation in WIS implosions. In this case, it is plausible that even higher charge states are present in the CESZAR implosions that are not observable with the spectroscopic system.

Line ratios observed in the WIS experiment indicated an imploding plasma electron temperature Te of 3-10 eV with 10 eV being a sufficient temperature to produce some plasma ionized to O VI. The values were obtained by matching experimental spectra to synthetic spectra from the Saha-LTE tool on the NIST Atomic Spectra database with electron density, $n_e = 10^{17} cm^{-3}$ [94]. Conversely, simulations run using the collisional-radiative code FLYCHK indicate that O VII may make up a substantial portion of the ionization distribution at just 16 eV [95], which may be achieved during the CESZAR implosion phase. The expected ion distributions

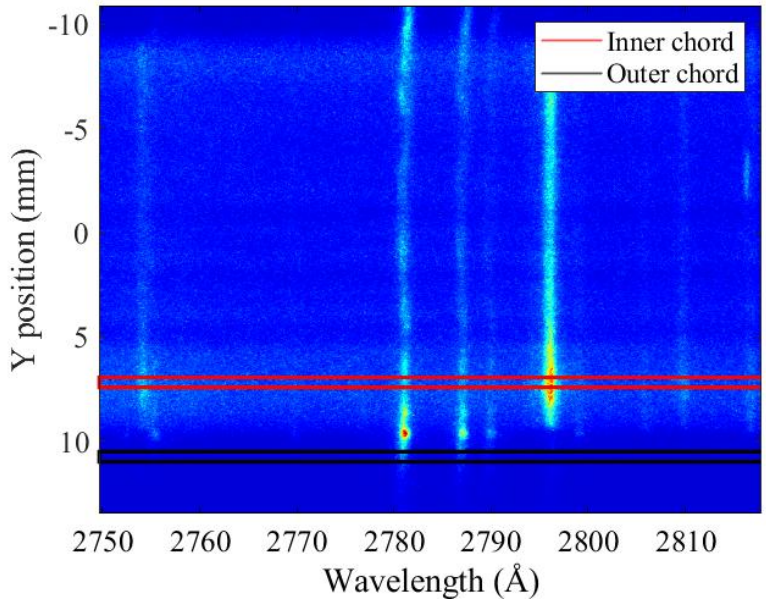

Figure 5.6: Spectral image of WIS oxygen emission. Emission from the O V and O IV lines can be seen extending past the broadband continuum emission cutoff near 9 mm.

for given electron temperatures and emission spectra in the range of the imaging diagnostic are shown in figure 5.7. At temperatures above 12 eV, emission from O VI is expected to dominate the spectral range detectable by the XUV framing camera, with the peak intensity near 70 eV in photon energy based on FLYCHK simulations; O VI emission is expected to dominate still at higher temperatures even when higher charge states are abundant ($T_e > 20eV$), predominantly O VII. This means that both the spectroscopic and imaging diagnostic systems may be unable to detect emission from higher charge states if T_e is sufficiently high.

Without a dedicated wide-range spectrometer to observe higher charge states or determine electron temperature, we cannot be certain that nearby higher charge states are responsible for the 'missing' current in the CESZAR implosions. However, given the higher charge states observed on CESZAR relatively early in the implosion, and the trend toward decreasing plasma-current coupling as the implosion progresses, trailing plasma composed higher charge states undetectable by the diagnostics used remains the most likely explanation.

In addition, we recognize that the electrode geometry may play a role in the plasma

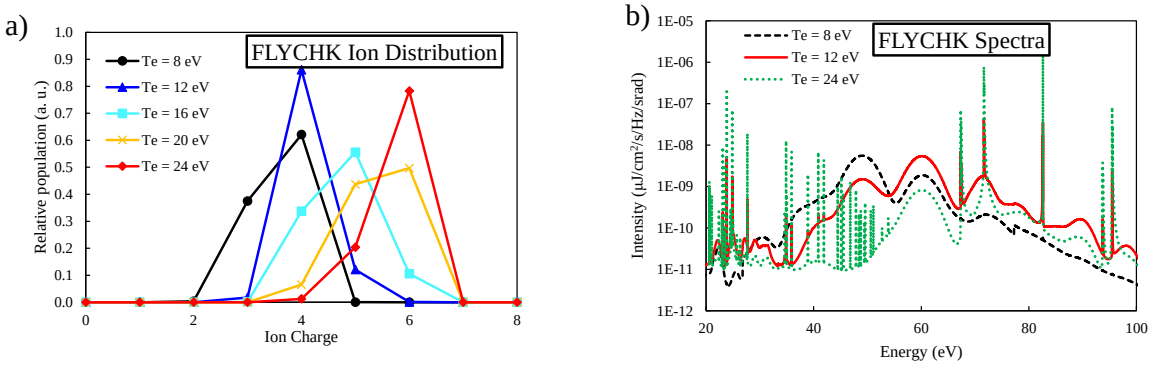

Figure 5.7: Ion distributions for given electron temperatures estimated in FLYCHK using an electron density of $10^{17} cm^{-3}$ are shown in (a). Emission spectra for three temperatures are shown in (b). The peak emission for $T_e = 8eV$ appears near 50 eV and results from O IV emission, while the peak emission for both $T_e = 12eV$ and 24 eV appears between 70 and 80 eV and results from O VI emission.

current coupling during the implosion as it may impact the breakdown phase. The knife-edge cathode geometry used on the WIS experiment may facilitate the initial gas breakdown, while a flat, honeycomb cathode was used on the CESZAR experiment. A poor initial gas breakdown may lead to un-swept or trailing plasma which may shunt current during the implosion. Furthermore, the initial gas-density profile and injector flow characteristics may impact current coupling as well. Reference [96] discusses the effect of initial breakdown on implosion dynamics up to the stagnation phase. These potential issues will be examined in chapter 6.

5.4 Radial Distributions of B_θ

Similar to the WIS experimental results discussed in chapter 4, simultaneous measurements of both O VI and O III transitions were made on the CESZAR experiments, allowing for a measured radial distribution of B_θ. For hollow oxygen implosions, spectra were obtained for four experimental shots resulting in measured profiles of B_θ which are shown in figure 5.8 along with profiles obtained from HYDRA simulations.

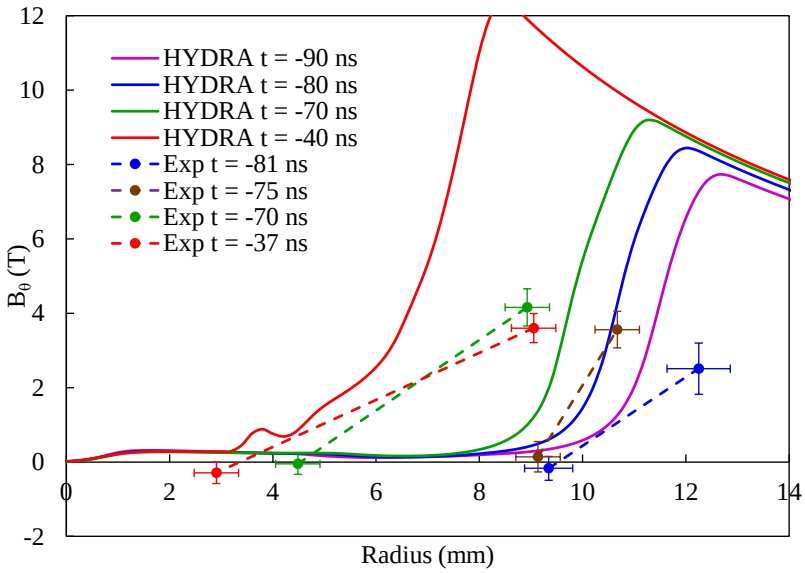

Figure 5.8: Measured and simulated profiles of B_θ during the CESZAR oxygen implosions for given times. The experimental times are relative to the stagnation time of the respective shot, while the simulation times are relative to the simulated peak compression time.

It should be noted that the radial separation between O VI and O III is significantly greater on the CESZAR implosions when compared with the WIS implosions (See ch 4). However, measurements made at these smaller radii indicate little to no magnetic field present there within the detection limits of the diagnostic system. Additionally, the measured profiles, do not indicate a radial implosion of the current layer. Later in time, measurements made at smaller radii (t = -37 ns, r = 9 mm) exhibit similar levels of magnetic field strength as measurements made earlier in the implosion. Considering the radial dependence of B_θ according to Ampere's law (equation 4.1), this means that the radial position of the bulk of the current is not following the imploding plasma.

5.5 Radial Velocity Measurements

The implosion velocity of the oxygen plasma can be obtained using two separate diagnostic systems. The outer plasma radius measured with three image frames (as in figure 5.4) can be used to obtain an average implosion velocity over the time interval of the three images, and is typically between 100 to 150 km/s. In addition, the spectral line observed from the O VI transition often exhibited a Doppler shifted line shape. A line of sight parallel to the radial motion (at y = 0) will observe plasma emitted from two opposite sides of the plasma column, where the plasma will emit red-shifted light as it travels away from the detector, and blue-shifted light where it travels toward the detector [97]. An example spectra showing this emission is displayed in figure 5.9.

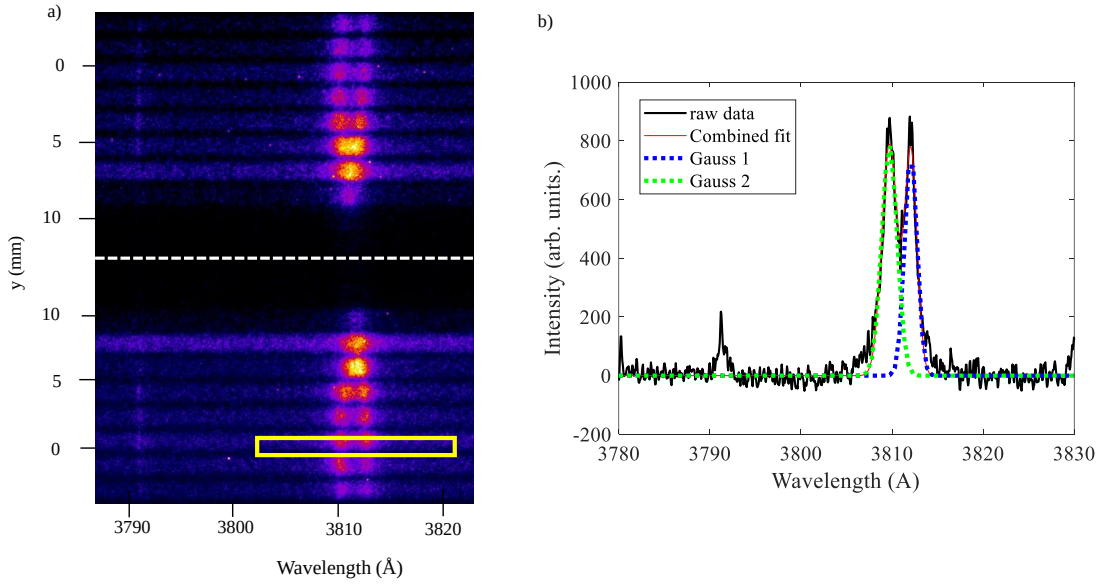

Figure 5.9: Spectrum showing a Doppler-shifted line shape. The rectangle in (a) displays the region used for fitting the Gaussian profiles which are displayed in (b).

The separation of the two peaks can be used to estimate the relative radial velocity of each side of the imploding plasma. The Doppler effect is the change in frequency of an emitter by the observer to the relative velocity between the two. Expression 5.3 quantifies the relationship between the observed change in wavelength ($\Delta\lambda$), unshifted wavelength (λ_0), relative velocity (v),

and the speed of light (c).

$$\Delta\lambda = \lambda_0 \frac{1 - \frac{v}{c}}{\sqrt{1 - \frac{v^2}{c^2}}} \tag{5.3}$$

Excluding the selected data to the region near y = 0 allows estimation of the implosion velocity of the integrated emission. Since the extent of O VI is observed on the same detector, the velocity measurement is localized to the radius of the emitting plasma. For example, figure 5.9 exhibits O VI emission (3811 Å) to a radial extent of approximately 10 mm, the measured velocity of the line observed across the plasma (observed at y = 0) yields an implosion velocity at r = 10 mm or less to be $93 \pm 3 km/s$. Furthermore, a Doppler shifted line shape is not observed from the O III transition ($\lambda = 3791$ Å). Given that the minimum measurable Doppler velocity is near 40 km/s for the 0.4 Å FWHM of the observed line, the velocity of plasma at this radius cannot be greater than 40 km/s since no Doppler shift is measured there, indicating a substantial velocity gradient between the two regions.

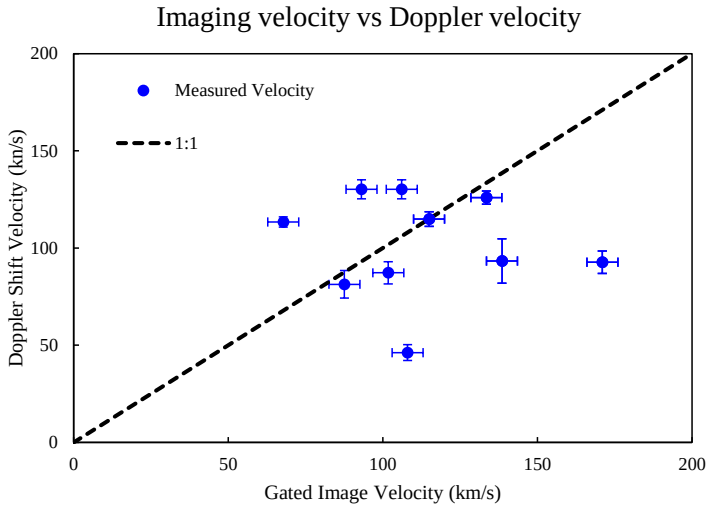

Figure 5.10: Measured velocity by imaging (horizontal axis) and Doppler shifts (vertical axis). A 1:1 correlation is plotted for reference. Values that deviate from the 1:1 reference indicate a discrepancy between velocity measurements made by the two diagnostic systems.

Comparing the local measurements of the radial velocity to average measurements made via imaging reveals the degree to which the average implosion velocity captures the dynamics at the local level. Figure 5.10. In many cases, the velocity measured by the two systems are closely correlated. When a large discrepancy is observed between the two measurements, MRT instabilities may play a role, resulting in a local velocity of O VI not captured by the average implosion velocity over a longer time scale. The local velocity measurements enabled by the spectroscopic diagnostic may provide information on the dynamics of individual charge states and their role in the current distribution. However, velocity measurements from more charge states at various radial positions would be required for further study.

5.6 Conclusion

Two similar gas-puff Z-pinch experiments were carried out using current drivers of significantly different current rise rates. Experiments on the faster rising current driver, CESZAR exhibited relatively low plasma-current coupling when compared to the slower rising current driver at WIS. Measurements of the azimuthal magnetic field were made in both experiments and compared with calculated values to determine the degree of 'plasma-current coupling' exhibited by both experimental systems. In contrast to the results produced by the WIS driver, the CESZAR data show substantially lower levels of plasma-current coupling, typically near 50%.

Examination of the stability of the imploding plasma column show that shunting across instability structures is not a likely cause of the reduced plasma current coupling. Full characterization of the radial charge state distribution and Te of the imploding plasma may provide insight into the expected current distribution evolution between the two drivers. Further work involving modeling of the plasma implosion is necessary to study this behavior.

5.7 Acknowledgements

Chapter 5 includes material as it appears in “Dependence of Plasma-Current Coupling on Current Rise Time in Gas-Puff Z-Pinches”, N. Aybar, F. Conti, M. Cvejic, D. Mikitchuk, M. Dozieres, E. Kroupp, J. Narkis, Y. Maron, and F. N. Beg, IEEE Trans. Plasma Sci., submitted for publication in 2021. N. Aybar was the primary author of this paper.

Chapter 6

Role of Initial Conditions in Liner-on-Target Implosions

6.1 Description of the Liner-on-Target Configuration

Besides their use as bright x-ray sources, gas-puffs Z-pinches have long been studied as a potential approach to controlled nuclear energy [4]. Approaches such as the magnetized liner inertial fusion (MagLIF) [98], and the staged Z-pinch [6, 99] are configured with a liner which collapses onto a target of fusion fuel, either deuterium (D_2) or a deuterium-tritium mixture (D + T). The MagLIF method has been studied on the $\sim 25MA$ Z-machine and consists of the implosion of an initially solid cylindrical metallic liner, typically chosen to be beryllium, onto a laser pre-heated deuterium target. An axial magnetic field is pre-imposed in the load region which serves to thermally insulate the liner from the target and mitigate conductive losses away from the target.

The staged Z-pinch concept instead uses a cylindrical gas liner, typically a high-Z Nobel gas such as argon or krypton which implodes onto the deuterium target. The staged Z-pinch also exhibits a pre-embedded axial magnetic field which serves to mitigate the magneto Rayleigh-

Taylor instability, which may also be helped by the chosen radial density profile [100, 101, 82]. Instead of laser pre-heating, the target fuel is preheated by shock waves which reach the target ahead of the imploding liner [102]. To date, the current distribution in liner-on-target implosions has not been studied experimentally. This chapter will discuss measurements of the azimuthal magnetic field in liner-on-target implosions made on the CESZAR linear transformer driver. These experiments are configured with an oxygen liner to facilitate the spectroscopic determination of B_θ and helium is chosen as the target gas, due to safety concerns of oxygen on deuterium experiments. A diagram of the liner-on-target approach is shown in figure 6.1.

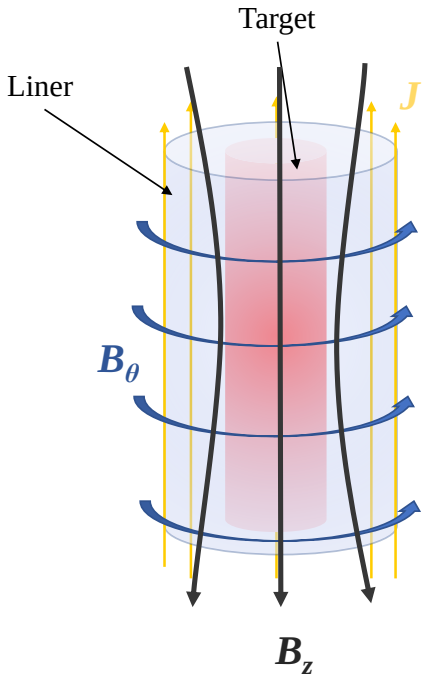

Figure 6.1: Diagram of the liner-on-target configuration. The annular liner gas surrounds the cylindrical helium target.

While the evolution of the radial distribution of B_θ within the liner and target plasmas

of these implosions are of interest, the primary area of interest discussed in this chapter is the role of various experimental initial conditions on the current distribution and plasma-current coupling in these liner-on-target implosions. First, the effect of the electrode design is studied by comparing the plasma-current coupling for three different cathode designs. Second, the effect of the initial gas-puff parameters on the current distribution is discussed. Lastly, the effect of the axial magnetic field on the instability and current coupling is examined. MHD simulations performed in HYDRA are were also performed to model the experimental results.

6.2 Effect of Initial Conditions on Plasma-Current Coupling

6.2.1 Electrode Design

To improve reproducibility between shots and the shot success rate of gas-puff Z-pinches, a pre-ionization system is often employed to assist the breakdown phase as discussed in section 2.4.1. Without a pre-ionization system, the experiment relies solely on the self breakdown allowed by the initial rise of the current driver. Since self breakdown is a highly statistical process, the nature plasma generated by the breakdown is unpredictable and may often fail. The electrode geometry may also be designed to assist the self breakdown. As discussed in section 2.4.1, self break under electrostatic conditions depends on the applied voltage, the number density in the gap, and the gap distance when considering geometrically flat electrodes. However, the introduction of pointed electrodes may assist with breakdown, since the electric field near edges may be much greater than flat regions.

The electrodes on the CESZAR driver consist of the the injector nozzle as the anode, and a flat cathode with a honeycomb hole pattern to allow transparency of the gas flow. In this study, the cathode was modified by installing twelve metallic screws in a ring pattern in the cathode that extend towards the anode. The experiment was carried out in three separate cathode configurations. 1) Flat (no screws), 2) screws at a $\sim 14mm$ radius, and 3) screws at $\sim 18.5mm$

radius. In both cases of the modified cathode, the 12 screws extend approximately 5 mm out of the honeycomb plate. The peak density produced by the liner valve occurs near 13 mm [88], which may be expected to produce the most reliable breakdown. Spectroscopic measurements of the azimuthal magnetic field can reveal the effect that this modification has on the plasma-current coupling. The approximate radial extent of the liner gas-puff is 18.5 mm. The array of screws at 19 mm was chosen to observe the plasma current coupling where the breakdown is initiated near the outer edge of the initial gas radius. A diagram of the modified cathode and photo are shown in figure 6.2.

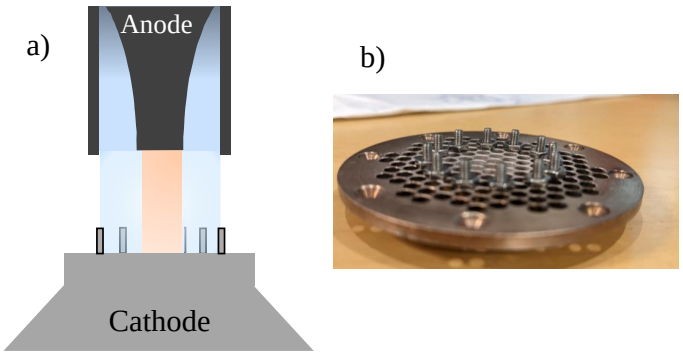

Figure 6.2: Diagram of the modified cathode (a) and photograph (b).

For many discharges, the emission measured with the spectroscopic system extended further than the plasma radius determined by the XUV framing camera, as was shown in chapter 5. This 'extended' O VI emission was observed more often at later implosion times, regardless of the cathode structure. Figure 6.3 shows an example spectral image with extended emission from O VI. The measured plasma radius from the XUV framing camera for this shot was near 5 mm, while emission on the spectrometer was observed over the entire field of view, to a radius of 16 mm. Due to the requirements of the azimuthal magnetic field measurement, B_θ can only be determined at the outer edge of this line (near 16 mm), and not at the radius observed by the XUV framing camera.

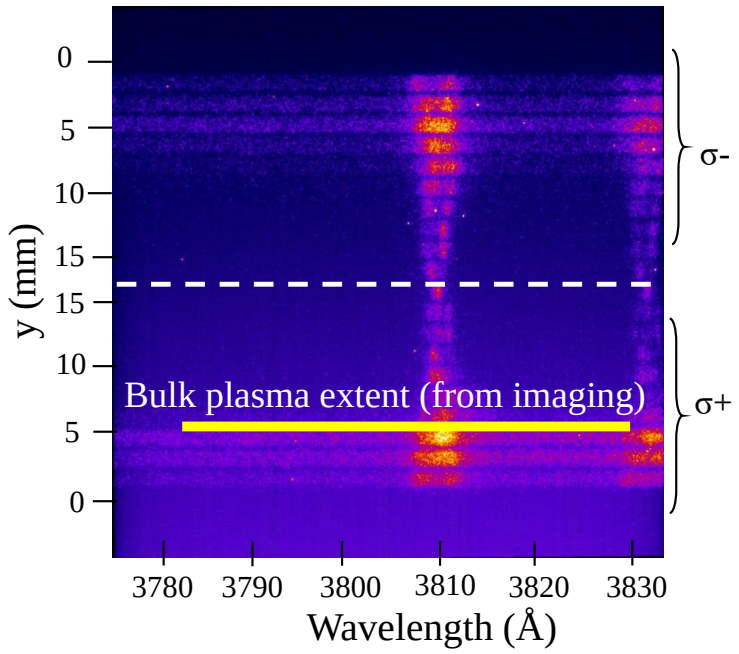

Figure 6.3: Spectral image showing greatly extended emission from O VI. The yellow line depicted on the bottom half of the image represents the plasma radius measured by the XUV framing camera, about 5 mm. Emission from low density plasma is observed well beyond this boundary, as far as 16 mm.

Figure 6.4 displays the difference in radii of the spectral emission r_{spect} and the plasma radii measured by the XUV framing camera, r_{image}. The extended O VI emission indicates the presence of a trailing or peripheral plasma of low density. While no apparent trend is observed in the peripheral plasma extent between the cathode types, the radial extent, or 'detachment' appears to increase as the implosion progresses, meaning the peripheral plasma is more pronounced closer to stagnation.

Limiting the data to cases where the spectral emission, r_{spect}, and outer plasma boundary, r_{image} are coincident allows for comparison of the 'plasma-current coupling' between the three different cathode configurations. The plasma-current coupling is again defined as the ratio of the spectroscopically determined value of B_θ and the value calculated with Ampere's law using the

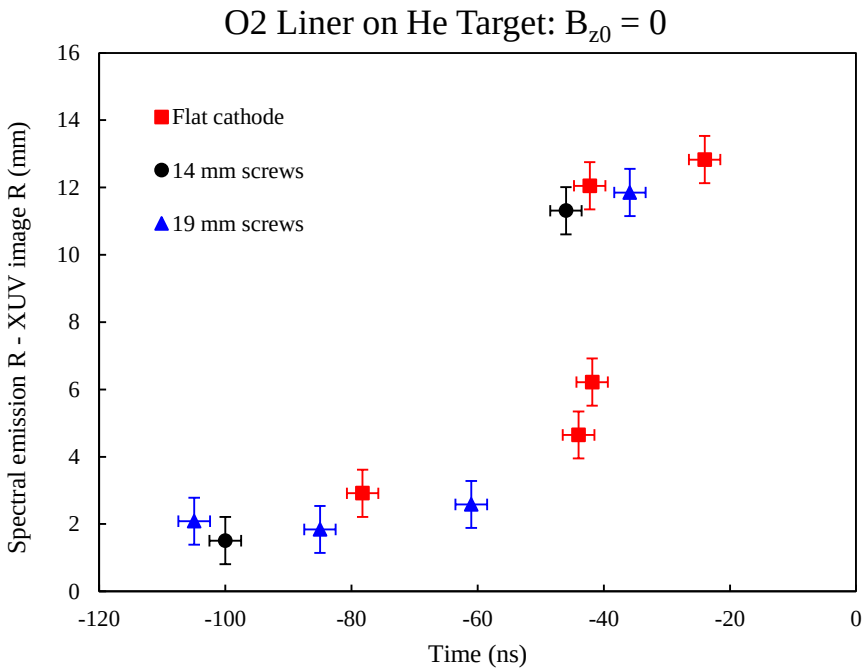

Figure 6.4: Observed radial extent of O VI emission vs plasma radius measured on framing camera plotted against time. Data are shown for all three cathode configurations.

total current measured by the b-dot probe array. The plasma-current coupling for these cases is shown in figure 6.5. The instances where $r_{spect} \approx r_{image}$ are few, but show a significantly greater degree of plasma-current coupling in for the 19 mm screws cathode when compared to both the flat cathode and 14 mm screws cathode. The plasma-current coupling was 45-60% for the 19 mm screws cathode, $\sim 20-35\%$ for the 14 mm screws cathode and 20% for the flat cathode.

While the modified cathode served to improve the shot success rate when compared to the flat cathode, the plasma-current coupling was less than 50% for the 14 mm screw cathode. Note that several data points displayed in figure 6.4 are not shown in figure 6.5 as the 'current coupling' is limited to those data where the edge of emission observed by the spectroscopic

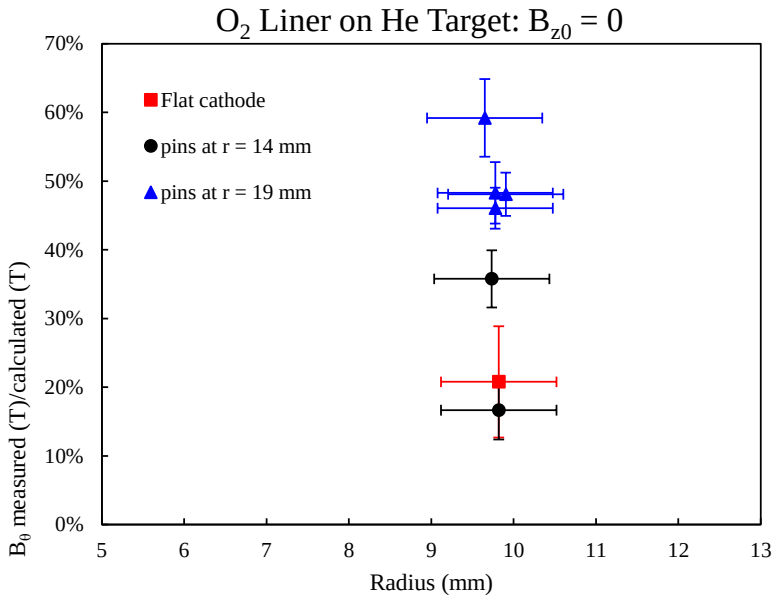

Figure 6.5: Plasma-current coupling measurements for each cathode configuration. The data are limited to those measurements where the spectral data emission extent coincides with the bulk plasma radius observed by the framing camera.

system coincides (within $\sim 2mm$) of the outer plasma radius observed by the gated imaging system. The relatively poor plasma-current coupling observed in the 14 mm screws cathode may be due to initially unionized gas residing beyond the radius of the initial breakdown. While the peak density of the liner gas puff is near 14 mm, a significant portion of gas resides up to $\sim 19mm$. The relatively greater degree of plasma-current coupling observed in the 19 mm radius screws cathode is therefore likely so due to less unionized gas lying beyond the initial breakdown radius, at least at the early times $(-110\,to-60ns)$. As in previous chapters, times are reported relative to pinch or stagnation time.

6.2.2 Gas-puff Parameters

The initial gas parameters may also affect the current distribution and plasma-current coupling of gas-puff implosions. Section 3.3 discussed the characterization of the initial gas density profile of the liner and target gases. The total linear mass supplied by the liner injector is determined by the plenum pressure, P_{LV}, and the duration that the valve is open, which for the liner valve will be called τ_{LV} in this chapter. However, the same linear mass can be achieved by multiple combinations of P_{LV} and τ_{LV}. For example, the measured LID for O_2 liner at $P_{LV} = 6psi, \tau_{LV} = 270\mu s$ is $\sim 7.2 \times 10^{16} cm^{-2}$, while the measured LID for $P_{LV} = 2.5, \tau_{LV} = 340\mu s$ is $\sim 6.1 \times 10^{16} cm^{-2}$. However, due to the limited sensitivity of the interferometry measurements, differences in the radial gas distribution between these two cases may not be detectable.

Azimuthal magnetic field measurements were made for two sets of initial gas injector parameters of similar linear masses, one with $P_{LV} = 6psi, \tau_{LV} = 270\mu s$ and the other with $P_{LV} = 2.5psi, \tau_{LV} = 270\mu s$. For brevity, the terms 'low pressure' and 'high pressure' will be used to refer to each set of gas parameters. Again, the spectroscopically determined B_θ values are compared with the calculated values of B_θ using the b-dot measured current and the radius of the spectroscopic measurement. The results are shown in figure 6.6. It should be noted that in all cases, the modified cathode with a circular array of screws at r = 19 mm were used, since they resulted in the greatest plasma-current coupling, shot success rate and shot-to-shot reproducibility. Furthermore, the data shown is again limited to cases where $r_{spect} \approx r_{image}$ to within 2 mm. It should be noted that for all cases, the same helium target parameters were used ($P_{TV} = 20psi, \tau_{TV} = 150\mu s$).

Valid measurements for the low pressure case ($P_{LV} = 2.5, \tau_{LV} = 340\mu s$) were limited to $-60\ to - 100ns$, and the measured plasma-current coupling was near 50%, while for the high pressure case ($P_{LV} = 6, \tau_{LV} = 270\mu s$), while the plasma-current coupling ranged from 50% to 85% for the same time range.

Additionally, the relatively low degree of plasma-current coupling resulted in later im-

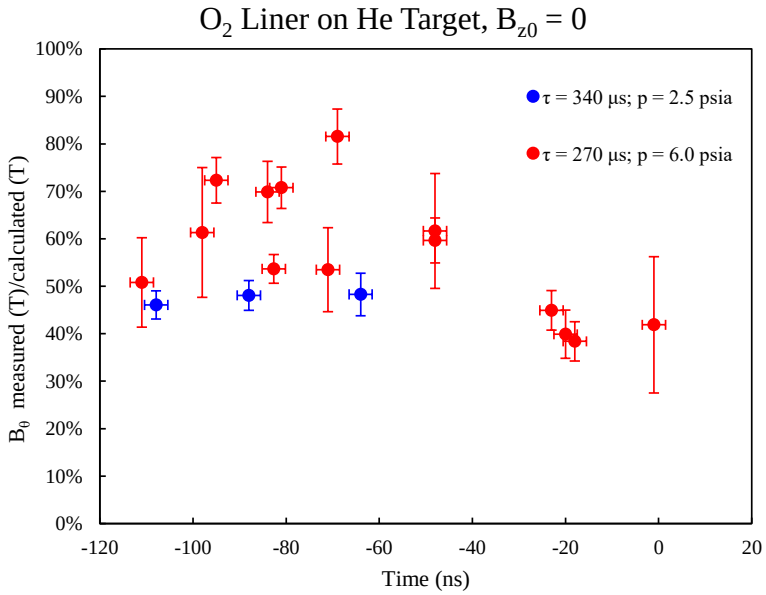

Figure 6.6: Plasma-current coupling measurements for two sets of gas parameters with similar linear masses. The greater quantity of data presented in the P = 6 psi case is partially a result of the greater shot success rate for such conditions.

plosions for the low pressure shots. A plot displaying the pinch time relative to the start of the current rise for both cases of initial gas parameters is shown in figure 6.7.

The slower implosions of the low pressure case are consistent with the relatively low measured plasma-current coupling observed in figure 6.6. The low pressure shots imploded in $288 \pm 23ns$ on average, while the high pressure shots imploded in $258 \pm 23ns$ on average Considering that roughly the same total mass per unit length is supplied by the injector in both high and low pressure cases, the longer implosion times are likely due to the reduced current coupling observed in the low pressure case.

The lower degree of current coupling, and thus slower implosions observed in the low pressure case is likely due to the longer valve duration allowing the injected gas to expand to a greater radius than in the high pressure, short valve opening duration cases. The results observed in section 6.2.1 which found greater current coupling with the breakdown assisting structures

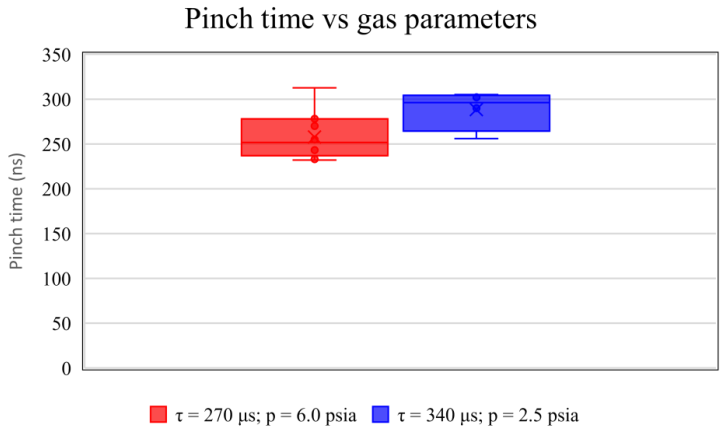

Figure 6.7: Spread of pinch times for several shots of the two sets of gas injector parameters. All times presented are relative to the start of the current rise as measured by the b-dot probe array.

placed at r = 19 mm, near the 'edge' of the initial gas profile. If a relatively longer valve open duration allows gas expansion significantly past the breakdown radius, the majority of the current may be carried by the freshly ionized, low density plasma supplied by the gas residing at radii greater than the breakdown position. The diffuse initial gas density profile was not measured in the initial characterization of the gas injector discussed in [88] and was likely below the measurement limits of the interferometry system. However, interferometric measurements of the line-integrated density of the liner gas-puff show a greater degree of uncertainty of measurements made during the steady state flow of the nozzle. Similar to the trend observed in section 6.2.1 regarding the radius of spectral emission vs radius of the framing image, the initial gas parameters have little to no impact on the emission 'detachment'. The difference in radius of the observed spectral emission from O VI and the radius observed on the image camera for both sets of initial gas parameters is shown in figure 6.8. While the detached O VI plasma is observed in both cases, a significant portion of the current is likely carried at an even greater radial position, since

spectroscopic measurements of B_θ still fall short of the expected values at these larger radii.

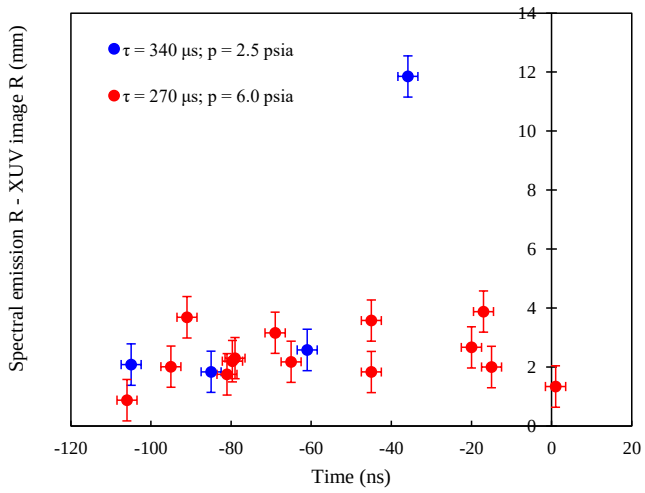

Figure 6.8: Difference of measured radius of O VI emission and radius measured via XUV framing camera for two sets of initial gas parameters.

Furthermore, because the gas injector is set in the anode position, the flow is directed towards the vacuum power feed of the CESZAR driver. Though the vertical section of the power feed is 5.3 cm from the central axis of the injector nozzle (an additional 3.4 cm from the liner outer radius, see figure 3.24), a sufficiently long duration may allow some gas to diffuse to the power feed, resulting in current shunting across the electrode gap upstream of the load region. Estimating the expansion rate with the sound speed of oxygen at 0 °C to be $0.32 mm\ /\mu s$ means molecules traveling radially outward at the sound speed may reach the power feed section after $\sim 100 \mu s$. Considering the low pressure shots had a valve duration $70 \mu s$ greater than the high pressure shots, it is plausible that shunting at the vacuum power feed played a role in the reduction of current coupling observed at the imploding plasma. However, due to the observed effect of the breakdown structure position on plasma-current coupling, and significantly greater distance between the liner nozzle outer radius and the vacuum power feed, it is likely that newly generated peripheral plasma beyond the initial breakdown radius is more important in the reduced

plasma-current coupling observed in the low pressure cases.

6.2.3 Axial Magnetic Field

The effect of a pre-embedded axial magnetic field has been discussed in the literature [65] and in chapter 4 of this thesis using the WIS driver (300 kA peak current, 1500 ns rise). In [65], it was found that the current tended to flow in a low-density peripheral plasma (LDP) when the pre-embedded axial magnetic field was applied, and the degree of current escape to the LDP increased with the magnitude of B_{z0}. In addition, chapter 4 discussed the dynamics and behavior of the radial distribution of B_θ with and without an axial magnetic field for cases when the presence of the LDP was mitigated by reducing contaminants. It was found that the axial magnetic field had little to no effect on the plasma-current coupling, but the measured radial distribution of B_θ evolved in general agreement with 1D MHD simulations when the axial magnetic field was applied.

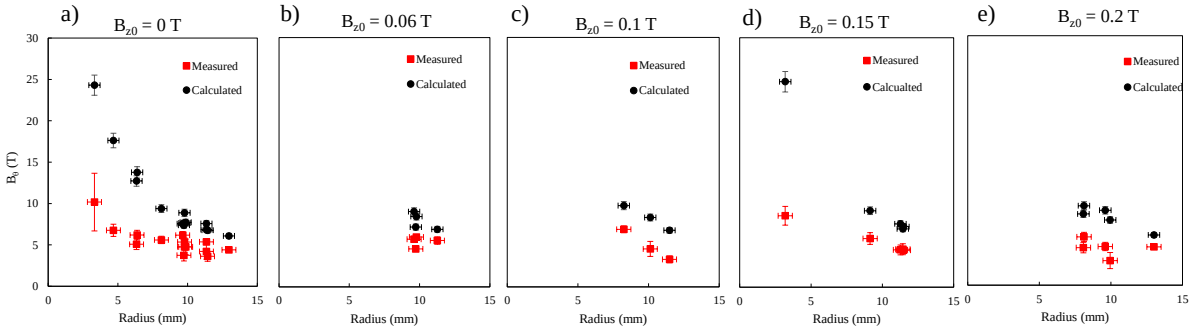

Figure 6.9: Measured and calculated values of B_θ coupling for all values of B_{z0}. Part (a) contains data for $B_{z0} = 0T$, (b) for $B_{z0} = 0.06T$, (c) for $B_{z0} = 0.1T$, (d) for $B_{z0} = 0.15T$, and (e) for $B_{z0} = 0.2T$

Experiments on the CESZAR driver were aimed to study the effect of the axial magnetic field on the faster current rising linear transformer driver. Using the parameters most favorable to high current coupling discussed in sections 6.2.1 and 6.2.2 (cathode breakdown structures at r =

19 mm, and $P_{LV} = 6psi, \tau_{LV} = 270\mu s$), the initial axial magnetic field was varied from 0 to 0.2 T and the azimuthal magnetic field was measured. The measured and calculated values of B_θ for all values of B_{z0} are shown in figure 6.9. In addition, the ratios of measured and calculated values are presented together in figure 6.10

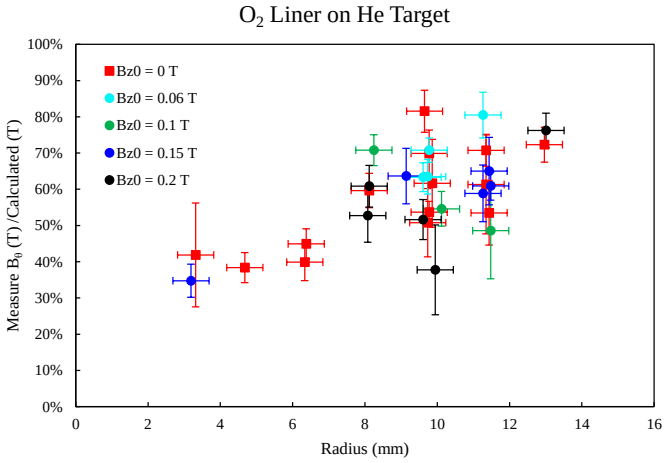

Figure 6.10: Measured plasma-current coupling for all values of B_{z0}. Each reported value of B_{z0} is accurate to within 0.02 T partly due to uncertainty in the calibration of the initial axial magnetic field and partly due to precision of the charge voltage of the axial magnetic field coil current driver.

The increasing trend of measured/calculated B_θ is largely consistent across all initial values of B_{z0} and indicates a reduction in plasma-current coupling as the implosions progress from larger to smaller radii. Early in the implosion ($-60\ to - 110ns$), when the outer plasma radius, r_o is 10-14 mm, the measured plasma-current coupling ranges from $\sim 50\%\ to\ 80\%$, largely independent of B_{z0}. Later in the implosion ($t > -50ns$), measured/calculated B_θ decreases below 50% to 30%, again both for $B_{z0} = 0$ or $0.15T$. No apparent effect of the initial axial magnetic field strength on plasma-current coupling is observed. While trailing plasma was observed in these experiments even in the absence of an axial magnetic field as shown in section 6.2.1, the relationship between escaped current to the LDP and the magnitude of B_{z0} seen in [65] is not observed on the CESZAR driver. This suggests an entirely different nature of the low density

or trailing plasma present on the CESZAR experiments compared to the low density peripheral plasma observed and discussed in [65]. The data presented in the previous sections in this chapter concerning the cathode structure and initial gas parameters, combined with the absence of an observable effect of the initial axial magnetic field on the plasma-current coupling suggests that the initial breakdown process is heavily involved in the generation of the trailing plasma, and thus the behavior of the current distribution during the implosion phase.

Once again, the degree of separation between emission from O VI observed on the spectroscopic system and the radius measured with the XUV framing camera is not ostensibly impacted by the magnitude of B_{z0}. This can be seen in figure 6.11.

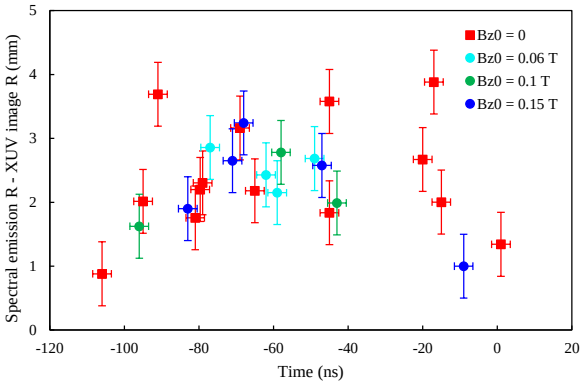

Figure 6.11: Difference of measured radius of O VI emission and radius measured via XUV framing camera for several values of B_{z0}..

The axial magnetic field is observed to mitigate the MRT instabilities present in the gas-puff implosions. Figure 6.12 displays two sets of images, with and without the axial magnetic field. As seen in the hollow imploding shell experiments discussed in chapter 5, the instability structures likely do not play a role in the shunted current, since plasma-current coupling is virtually the same regardless of the initial axial magnetic field strength, and therefore the prevalence of MRT instability structures.

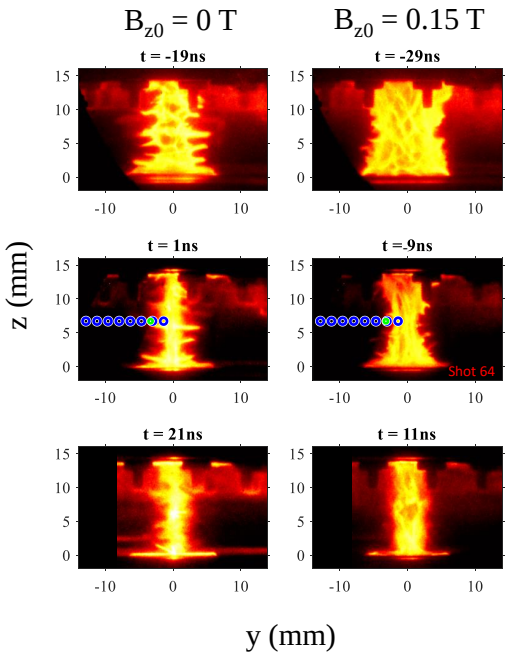

Figure 6.12: Framing camera images of the plasma near stagnation both without (left column) and with a pre-embedded axial magnetic field (right column). The middle row of frames (1 ns, -9 ns) displays the field of view of the spectroscopic system via the blue circles, and the green circles represent, including the region from which emission was selected for determination of B_θ. The timing of these middle frames coincides with the acquisition window of the spectroscopic system.

6.3 MHD Simulations

Magnetohydrodynamic simulations of the oxygen liner on helium target were performed in HYDRA, a code developed by Lawrence Livermore National Laboratory [73]. Six simulations were performed in 1D arbitrary Lagrangian-Eulerian (ALE) mode, three with $B_{z0} = 0T$, and three with $B_{z0} = 0.15T$. The simulations were run using the resistive MHD model where Hall and extended MHD effects are neglected. The modified Epperlein-Haines conductivity model [103] with Lee-More degeneracy corrections [92]. The simulations were initialized with the measured radial gas density profiles based on interferometric measurements of both the liner and target gas-puffs. The entire linear mass (M/L) of the initial gas puff was 7.6 $\mu g/cm$ (6.4 $\mu g/cm$ in the

liner and 1.2 $\mu g/cm$ in the target). Two simulations were performed with the nominal circuital parameters (one with $B_{z0} = 0\ T$, one with $B_{z0} = 0.15\ T$), which ultimately requires 100% of the current to flow within the imploding plasma. Another set of simulations were run with a reduced initial charge voltage in order to roughly simulate the fact that only a fraction of the current flows within the imploding plasma. One pair was run with a charge voltage equal to 70% of the experimental charge voltage, and another initialized at 50% of the initial charge voltage. Reducing the charge voltage in the initialization of the simulation effectively reduces the current amplitude by the same factor at all times during the simulation. This can be seen by inspection of an analytic solution to the RLC (see equation 3.1). These values were chosen to reflect the observation that the measured values of B_θ varied from $\sim 70\%\ to \sim 30\%$ during the implosion.

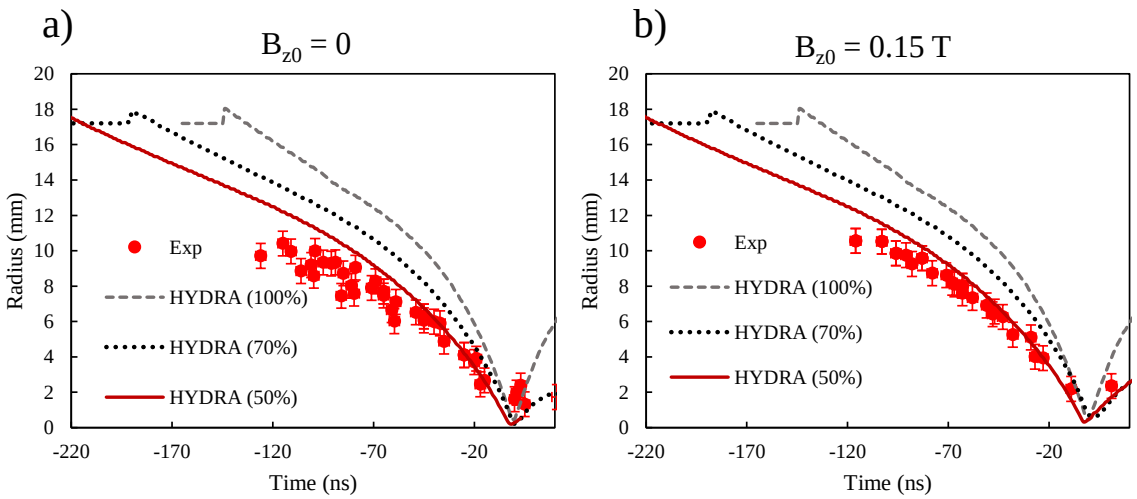

Figure 6.13: Implosion trajectories for HYDRA simulations carried out with full charge voltage (100%), 70% of full charge voltage, and 50% of full charge voltage juxtaposed against the experimental results for cases where $B_{z0} = 0T$ (a) and $B_{z0} = 0.15T$ (b). All experimental results are reported relative to the stagnation time of each respective shot. The simulation results are presented with timing relative to the bang time or minimum radius of each respective simulation.

Implosion trajectories for all MHD simulations and experimental measurements are shown in figure 6.13. The experimental results shown in figure 6.13 are limited to shots taken with

$P_{LV} = 6psi, \tau_{LV} = 270\mu s$, and breakdown pins at r = 19 mm. The times reported are relative to the stagnation time for each respective shot. For each simulation, t = 0 is chosen to coincide with the peak emissive power of radiation, which also coincides with the minimum outer plasma radius. This is important to keep in mind when considering the HYDRA simulation results for the full charge voltage, since the simulated implosion time is only 165 ns relative to the start of the current drive, while the experimental implosion time is 258 ± 20 *ns* without the pre-embedded axial magnetic field, and 245 ± 15 *ns* with $B_{z0} = 0.15T$. By contrast, the implosion time for HYDRA simulations was 220 ns at 70% charge voltage, and 260 ns at 50% charge voltage. The simulated implosion trajectories were mapped by tracing the radial position of 5% of the peak density at each time step. The trajectory mapped by tracing the peak density gradient produced by the simulation results yielded a virtually identical result.

While the measured values of B_θ were observed to vary throughout the implosion and between discharges, the implosion trajectory is well reproduced by the MHD simulations with half of the initial charge voltage. The radius measured by experiment early in the implosion (-120 ns to -70 ns) show a greater degree of compression and smaller radius than predicted by the simulation. This discrepancy is consistent with a higher degree of plasma-current coupling early in the implosion observed by the spectroscopic measurements of B_θ discussed in the previous sections of this chapter. Focusing on the experimental results and simulation results assuming 50% charge voltage, and considering that the measured B_θ near the edge of the plasma column is near 70% at early times, the magnetic pressure driving the implosion results in an experimental radius smaller than predicted by the MHD simulations. The HYDRA results for 70% charge voltage do not show overlap with experimental results for these times in figure 6.13 due to the significant discrepancy in pinch timing between experiment and simulations performed at 70% charge voltage.

Referencing the 70% charge voltage simulations to match the experimental bang time of 258 ns for $B_{z0} = 0T$, and 245 ns for $B_{z0} = 0.15T$ yields an agreement of implosion trajectories

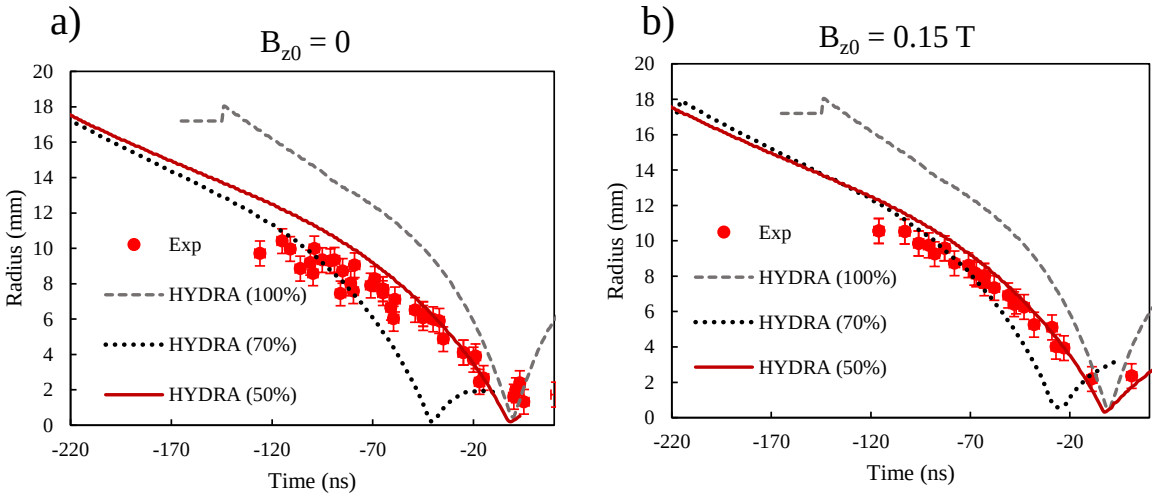

Figure 6.14: Implosion trajectories for HYDRA simulations juxtaposed with experimental results. The 70% charge voltage simulation results exhibit modified reference times to match experimental implosion times.

during these early time frames. These modified implosion trajectories for 70% charge voltage are shown in figure 6.14. Note that the simulations at full charge and half charge in figure 6.14 do not display modified timing and are identical to those displayed in figure 6.13 for the purpose of comparison.

A limited number of experimental discharges yielded spectroscopic data from O VI and O III simultaneously in a similar manner as discussed in chapters 4 and 5. This spectroscopic data allowed for determination of the radial distribution of B_θ from two radial positions. These measured distributions can be directly compared with simulated profiles produced by HYDRA for various times. The measured and simulated radial profiles of B_θ are shown in figure 6.15. Similar to the implosion trajectories discussed above, the experimentally determined radial profiles are well reproduced for the instances shown in figure 6.15 (a, b) initialized with half of the charge voltage. By contrast, a large discrepancy is observed between measured and simulated radial profiles of B_θ assuming full charge voltage in the simulation. In this case, the discrepancy is

largely due to the discrepancy in implosion times between experiment and simulations at full charge voltage.

The measured radial profiles of B_θ only loosely follow the evolution predicted by the simulations. That is, HYDRA predicts a collapsing radial profile, with a greater peak value at a smaller radius as the implosion progresses. The limited set of data displayed in figure 6.13 do not consistently exhibit this trend. For example, data collected at t = -97 ns and t = -85 ns exhibit similar radial profiles. While the measurements of plasma-current coupling at the outer radius of the imploding plasma do show a reduction in $B_{\theta measured}/B_{\theta expected}$, the lack of evolution in the profiles shown in figure 6.13 is more likely a result of the limited spatial resolution (about 1 mm) of the spectroscopic system, and thus resolution of the measured $B_\theta(r)$. Since the time frames observed are relatively near to each other (only 12 ns apart), contraction of the B_θ on this time scale may be smaller than the system can measure.

6.4 Discussion

The initial breakdown conditions may significantly impact the current distribution during the implosion phase. Data discussed in section 6.2.1 found that plasma-current coupling was improved when the electrode was modified to initiate breakdown at a relatively large radius. Section 2.4.1 found that a shorter valve opening duration, and thus, a lesser degree of initial gas expansion also led to improved plasma-current coupling. In all scenarios, a trailing or peripheral plasma was often observed, and measured values of B_θ did not exceed 80% of the expected values. However, contrary to observations discussed in [65], the initial axial magnetic field did not significantly alter the current distribution, meaning the role of the trailing or peripheral plasma was inherently different in the CESZAR experiments discussed in this chapter.

The data discussed in this chapter indicates a potential source of the trailing plasma is due to the non-uniformity of the initial breakdown of the oxygen gas. When breakdown is initiated

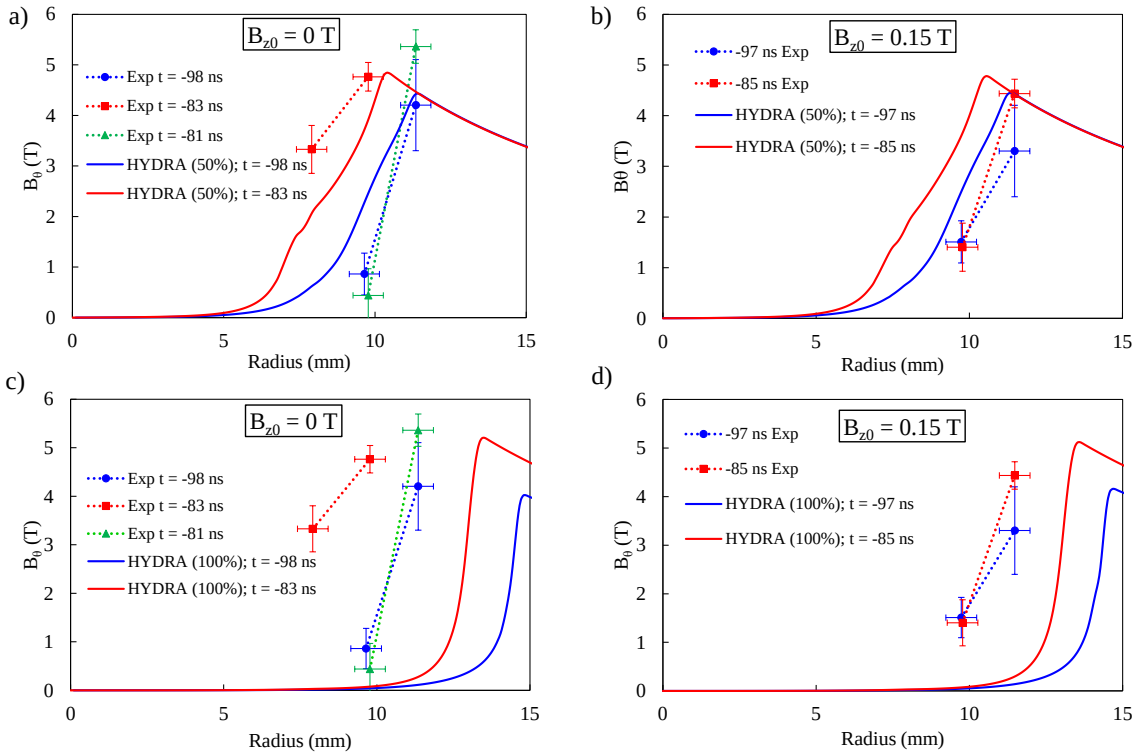

Figure 6.15: Measured radial profiles of B_θ both with $B_{z0} = 0T$ (a, c) and $B_{z0} = 0.15T$ (b, d) and simulated profiles with 50% charge voltage (a, b) and full charge voltage (c, d). All experimental times presented are relative to the pinch timing of the respective shot, while simulation results are shown relative to the simulation bang time.

near the pin structures (screws), gas lying beyond this radius may remain neutral at the start of the implosion, and begins to carry current as an ionization wave propagates radially outward as seen in previous experimental studies [104]. Figure 6.16 displays the hypothetical scenario illustrating the expansion of gas beyond the breakdown structures.

The illustration shown in figure 6.16 shows an exaggerated radial extent of the gas puff near the cathode to characterize the difference in initial gas puffs between the low pressure (long opening duration) and high pressure (short opening duration). As discussed in section 6.2.2, the longer valve opening duration may allow the gas-puff to expand to a greater degree than the short opening duration. If the initial breakdown primarily ionizes plasma near the screws located at r = 19 mm, unionized gas may remain past this boundary, especially if a longer valve opening duration has allowed it to expand there. The reduced plasma-current coupling observed in section

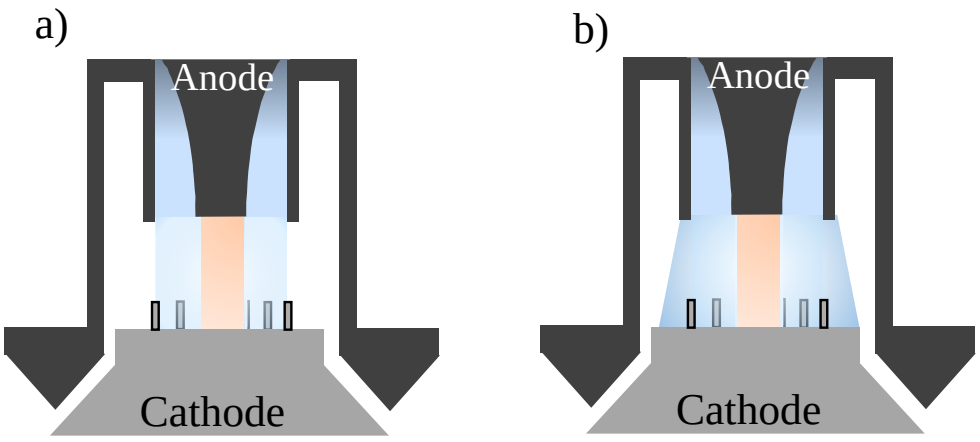

Figure 6.16: Illustration of the gas puff in the load region in two scenarios, (a) with no expansion of the gas puff past the breakdown screws and (b) with significant expansion.

6.2.2 may be due to a continuous flux of newly ionized plasma at the outer plasma boundary sourced in previously unionized gas. Alternatively and perhaps additionally, a long opening duration may allow gas to expand to the transmission line gap located at the outer edge of the cathode, allowing current to be shunted there. However, measurements of B_θ made using the extended emission of O VI (well past the bulk plasma boundary) approach 100% of Ampere's law. Since the cathode edge is ~ 3 cm beyond the field of view of the spectral system, a significant quantity of current is not likely shunted in the transmission line gap.

6.5 Conclusion

Experimental results observing the plasma-current coupling in various conditions have implications for the delivery of current in gas-puff implosions on the CESZAR driver. Experimental measurements of the azimuthal magnetic field were obtained with a time-gated, high resolution, polarization-based ultraviolet spectroscopic system. The initial breakdown of the gas-puff was

assisted by implementing breakdown structures into the cathode, this led to a substantial increase in the measured azimuthal magnetic field in the imploding plasma while the breakdown structures were located at the nominal initial outer radius of the gas puff when compared to results obtained at the peak density radius and with the flat cathode.

A short valve opening duration was also found to exhibit a higher level of azimuthal magnetic field in the imploding plasma when compared to a long valve opening duration. The average implosion time was also shorter for shots with a shorter valve opening duration when compared to shots with a longer valve opening duration and the same total mass. These indicate an important role of the initial gas distribution on the plasma-current coupling during the implosion.

The experimentally measured implosion trajectory, and implosion time is well reproduced by magnetohydrodynamic simulations performed in HYDRA where the initial charge voltage applied to the simulation was half of the experimental CESZAR charge voltage. In addition, measured radial profiles of B_θ near 100 ns prior to stagnation are also reproduced by simulations at half charge voltage. In contrast Simulations performed with 100% of the experimental CESZAR charge voltage implode in 2/3 of the experimental implosion time and neither match the experimental implosion trajectory or measured radial B_θ profiles. Simulations at an intermediate of 70% charge voltage exhibit some agreement with the implosion trajectory at early stages in the implosion, when current coupling is known to be greater than 50%. Agreement with between experimental implosion trajectories and simulations at half charge voltage further verify the findings made by the spectroscopic data of B_θ and indicate a significant loss of current in the imploding plasma to a trailing plasma or shunting in the vacuum power feed.

The strength of the pre-embedded axial magnetic field was found to have little effect on the measured/expected azimuthal magnetic field values in the imploding plasma. This fact, when considered alongside the role of the cathode structure and initial gas profile indicates that the nature and uniformity of the initial breakdown of the gas-puff is of great importance to the level of current flowing within the imploding plasma during the implosion phase.

6.6 Acknowledgements

Chapter 6 contains material which is being prepared for submission for peer-reviewed publication as “Role of Initial Conditions in Liner-on-Target Implosions” N. Aybar, F. Conti, J. Narkis, and F. Beg. N. Aybar is the primary author of this paper

Chapter 7

Conclusions & Future Work

7.1 Effects of an Axial Magnetic Field on Current Distribution

The initial experiments of this study were performed at the Weizmann Institute of Science. These experiments aimed to study the magnetic field distribution of imploding annular oxygen plasmas both with and without axial magnetic stabilization. This was achieved by relying primarily on the simultaneous detection of transmission lines from both O VI and O III charge states which were present at different radial positions, allowing spectroscopic determination of B_θ at two positions. Comparison of the experimentally determined radial B_θ profiles and simulated profiles produced by a 1D MHD model indicated good qualitative agreement in the case where $B_{z0} = 0.26T$, though an overestimation of the plasma compression by the 1D models resulted in correspondingly shifted radial B_θ profiles. Conversely, the measured B_θ profiles where $B_{z0} = 0T$ were not well represented by the 1D MHD simulations and varied between shots. The presence of instability structures may be responsible for locally inverting the B_θ distribution near the boundary, or disrupt the tangential line of sight required by the diagnostic technique.

Additionally, the spectroscopic measurements of B_θ at the plasma-vacuum boundary indicated that at least 80% of the current flowed within that boundary both with and without

magnetic stabilization. Since these experiments were designed to reduce contaminants which resulted in shunted current observed in reference [65], the axial magnetic field did not appear to result in redistributed current to a low density trailing plasma. The exception to this trend was at times approaching stagnation where the measured values of B_θ fell below 80% of the calculated values.

Measurements of the axial magnetic field at r = 0 during the implosion showed good quantitative agreement with the 1D MHD simulations. While measurements during stagnation were not available, measurements during the implosion phase together with the qualitative agreement of experiment and simulation regarding the radial profile of B_θ indicated an accurate model of magnetic diffusion, and therefore plasma resistivity employed by TRAC-II.

7.2 Dependence of Plasma-Current Coupling on Current Rise Time

Experiments carried out on the CESZAR linear transformer driver replicated the azimuthal magnetic field diagnostic and the load configuration used on the WIS experiments discussed in chapter 4. By comparing the results of two drivers of a similar current level but significantly different driver rise times, the effect of driver rise time on plasma-current coupling was explored. The CESZAR driver was found to deliver a fraction of the current to the imploding plasma, typically near 50%, contrasted by approximately 80% or greater on the WIS driver. Although a greater implosion velocity and acceleration were achieved, leading to more pronounced MRT instabilities on the CESZAR implosions, the reduced level of plasma-current coupling was not attributable to shunting across instability structures according to the data obtained.

Since the radial charge state distribution indicated higher temperatures at larger radii, it is likely that O VII was present beyond the radius at which spectroscopic measurements of B_θ were made using the O VI transition. Although undetectable by the diagnostic systems used on

CESZAR, the plasma composed of charge states higher than O VI likely carried the a significant portion of the driver current. The reduction in measured vs expected B_θ at later times in the implosion also supports this hypothesis, since electron temperatures are expected to increase as the implosion approaches stagnation.

While higher temperatures are achieved earlier on the CESZAR driver when compared to WIS, the plasma-current coupling remains lower on CESZAR during the entire implosion process. The difference in electrode structure between the two drivers may also play a role, as the quality of the initial plasma breakdown is likely affected by the cathode geometry, thereby impacting the current distribution during the implosion phase. These considerations were explored in chapter 6.

7.3 Role of Initial Conditions in Liner-On-Target Implosions

Further experiments carried out on the CESZAR linear transformer driver examined the impact of the cathode geometry, initial gas-puff parameters, and initial axial magnetic field on the plasma-current coupling in liner-on-target gas-puff Z-pinches. Spectroscopic measurements of the azimuthal magnetic field were made on an oxygen gas-puff implosion and were compared with expected values calculated using Ampere's law.

Altering the cathode geometry by placing metallic screws protruding into the anode-cathode gap assisted the initial breakdown phase, leading to a higher shot success rate and a greater fraction of current flowing within the imploding plasma. The results obtained with screws placed near the peak density of the initial gas puff may have marginally increased the current coupling when compared to the flat cathode. The breakdown screws yielded the greatest plasma-current coupling when placed near the outer edge of the initial gas puff. In addition, a shorter gas valve opening duration produced greater plasma-current coupling than data obtained with a long gas valve opening duration, for the equivalent total mass injected.

The initial axial magnetic field strength was shown to have little to no effect on the current

distribution for CESZAR implosions. While trailing or peripheral plasma was observed on these implosions, current escape to the peripheral plasma was not observed on CESZAR as described in [65].

Magnetohydrodynamic simulations of the oxygen implosions were carried out. The simulations were repeated with a reduced charge voltage (70%, and 50%) to emulate the loss of current to the imploding plasma. The experimentally measured implosion trajectories were best captured by simulations out at 50% charge voltage. Although the measured vs expected values of B_θ vary from $\sim 70\%$ to $\sim 30\%$ throughout the implosion phase, this result is consistent with a total average of approximately 50% of the current present within the imploding plasma.

These results, together, indicate that the current coupling achieved on gas-puff implosions on the linear transformer driver may be optimized by altering the conditions of the initial gas breakdown. Increasing the radial density gradient of the initial gas-puff and initializing breakdown near the outer gas-edge allows for a reduction in current loss to the trailing or peripheral plasma.

7.4 Future Work

To further improve the plasma-current coupling in gas-puff Z-pinches on the linear transformer driver, further modifying the electrode structure, altering the gas-puff configuration, and including a pulsed pre-ionization system logically follow given the results presented in this dissertation. Additionally, characterization of the initial breakdown plasma would greatly improve the understanding of plasma-current coupling in gas-puff implosions.

A preionization system, currently in development at UC San Diego consists of a cylindrical metallic ring placed beyond a mesh structure facing the gas flow. A high voltage pulse may produce a discharge in the anode region of the gas flow, generating some free electrons, improving the statistical likelihood of the Townsend avalanche. To impliment this device on the CESZAR driver, the gas-injector must be installed in the cathode position. This will also direct the flow

away from the transmission line gap, rather than towards it, reducing the likelihood of shunted current in that region. An illustration of the modified load region is shown in figure 7.1.

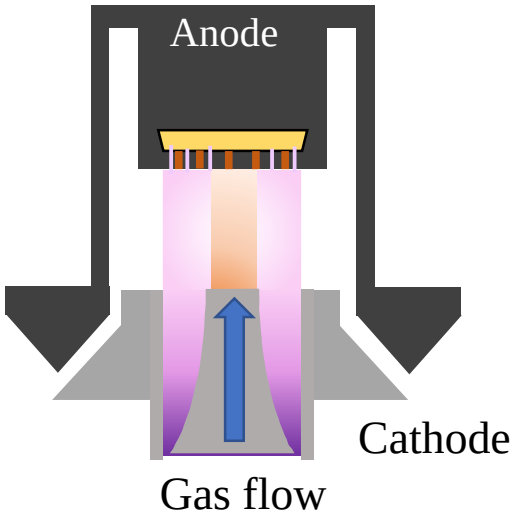

Figure 7.1: Illustration of the modified load hardware including a pulsed preionizer system in the anode position, shown in yellow (not to scale).

A wide range visible spectrometer may be used to characterize the level of ionization produced during a discharge of the pulsed preionization system into the gas flow. Spatially resolved measurements will allow for characterization of the radial distribution of charge states produced near the anode to assess the uniformity of the preionization. Measurements made in conjunction with the initial rise of the CESZAR discharge may further characterize the breakdown plasma once the current is initialized, potentially throughout the entire gas-puff volume. However, the current levels are likely far too low to measure the azimuthal magnetic field at this early stage using the diagnostic techniques available. Measurements of the azimuthal magnetic field during the implosion and stagnation phases will determine the degree to which the preionization system improves the plasma-current coupling.

The use of high-Z liner gases is of interest in the pursuit of certain approaches to thermonuclear fusion [6, 102, 105]. The atomic structure of different gas-species result in varied responses to applied voltages, therefore, the initial breakdown phase of a gas-puff Z-pinch is also likely impacted by the chosen gas or gas mixture. Characterizing the breakdown phase and subsequently, plasma-current coupling for high-Z noble gases such as argon, krypton, and neon is a worthwhile endeavor in the pursuit of gas-puff Z-pinches as an approach to thermonuclear fusion, as well as for their use as high flux x-ray sources.

The diagnostic techniques used in this thesis may be employed further to characterize the magnetic fields during the stagnation phase. Spatially resolved measurements of the axial magnetic field have not been reported in the literature to date. Axial magnetic flux amplification may be involved in a greater-than predicted mitigation of the magneto Rayleigh-Taylor instability as reported in several studies [72, 82]. To understand the role of this phenomenon in Z-pinches, experimental measurements of the axial magnetic field during the stagnation phase are necessary. The high densities and temperatures present in stagnated Z-pinches enforce practical limitations on the capabilities of diagnostics, including Zeeman spectroscopy. Experiments utilizing end-on measurements of the imploded plasma may exploit the polarization-parallel method used in this thesis to obtain measurements at relatively high densities and temperatures. Furthermore, the axial magnetic field system on CESZAR is capable of producing an initial field of up to $\sim 1T$, much greater than required for mitigation of MRTI. Considering that magnetic flux is conserved during the implosion, and that a relatively large minimum radius would be achieved in such an experiment, a lower peak density and relatively high final axial magnetic field may facilitate spectroscopic diagnosis of the axial magnetic field.

Bibliography

[1] W. H. Bennett, "Magnetically self-focussing streams," *Phys. Rev.*, vol. 45, pp. 890–897, Jun 1934.

[2] M. Blackman, "Self-magnetic field in high current discharges," *Proceedings of the Physical Society. Section B*, vol. 64, pp. 1039–1045, dec 1951.

[3] P. C. Thonemann and W. T. Cowhig, "The role of the self magnetic field in high current gas discharges," *Proceedings of the Physical Society. Section B*, vol. 64, pp. 345–354, apr 1951.

[4] D. D. Ryutov, M. S. Derzon, and M. K. Matzen, "The physics of fast z pinches," *Rev. Mod. Phys.*, vol. 72, pp. 167–223, Jan 2000.

[5] C. Deeney, T. J. Nash, R. B. Spielman, J. F. Seaman, J. S. McGurn, D. O. Jobe, M. F. Vargas, T. L. Gilliland, R. C. Mock, K. W. Struve, K. G. Whitney, P. E. Pulsifer, J. P. Apruzese, J. W. Thornhill, and J. Davis, "Improved large diameter wire array implosions from increased wire array symmetry and on-axis mass participation," *Physics of Plasmas*, vol. 5, no. 6, pp. 2431–2441, 1998.

[6] H. U. Rahman, F. J. Wessel, and N. Rostoker, "Staged z pinch," *Phys. Rev. Lett.*, vol. 74, pp. 714–717, Jan 1995.

[7] S. M. Zakharov, G. V. Ivanenkov, A. A. Kolomenskij, S. A. Pikuz, A. I. Samokhin, and I. Ulshmid, "Wire x-pinch in a high-current diode," *Pis'ma Zh. Tekh. Fiz.; (USSR)*, vol. 8:17, Sep 1982.

[8] T. A. Shelkovenko, S. A. Pikuz, A. D. Cahill, P. F. Knapp, D. A. Hammer, D. B. Sinars, I. N. Tilikin, and S. N. Mishin, "Hybrid x-pinch with conical electrodes," *Physics of Plasmas*, vol. 17, no. 11, p. 112707, 2010.

[9] M. G. Haines, "A review of the dense z-pinch," *Plasma Physics and Controlled Fusion*, vol. 53, no. 9, 2011.

[10] J. L. Giuliani and R. J. Commisso, "A review of the gas-puff z-pinch as an x-ray and neutron source," *IEEE Transactions on Plasma Science*, vol. 43, no. 8, pp. 2385–2453, 2015.

[11] J. Shiloh, A. Fisher, and N. Rostoker, "Z pinch of a gas jet," *Physical Review Letters*, vol. 40, no. 8, pp. 515–518, 1978.

[12] C. Stallings, K. Childers, I. Roth, and R. Schneider, "Imploding argon plasma experiments," *Applied Physics Letters*, vol. 35, no. 7, pp. 524–526, 1979.

[13] J. P. Chittenden, S. V. Lebedev, S. N. Bland, F. N. Beg, and M. G. Haines, "One-, two-, and three-dimensional modeling of the different phases of wire array z-pinch evolution," *Physics of Plasmas*, vol. 8, pp. 2305–2314, 5 2001.

[14] Y. Maron, A. Starobinets, V. I. Fisher, E. Kroupp, D. Osin, A. Fisher, C. Deeney, C. A. Coverdale, P. D. Lepell, E. P. Yu, C. Jennings, M. E. Cuneo, M. C. Herrmann, J. L. Porter, T. A. Mehlhorn, and J. P. Apruzese, "Pressure and energy balance of stagnating plasmas in *z*-pinch experiments: Implications to current flow at stagnation," *Phys. Rev. Lett.*, vol. 111, p. 035001, Jul 2013.

[15] E. P. Yu, M. E. Cuneo, M. P. Desjarlais, R. W. Lemke, D. B. Sinars, T. A. Haill, E. M. Waisman, G. R. Bennett, C. A. Jennings, T. A. Mehlhorn, T. A. Brunner, H. L. Hanshaw, J. L. Porter, W. A. Stygar, and L. I. Rudakov, "Three-dimensional effects in trailing mass in the wire-array z pinch," *Physics of Plasmas*, vol. 15, 2008.

[16] R. S. Pease, "Equilibrium characteristics of a pinched gas discharge cooled by bremsstrahlung radiation," *Proceedings of the Physical Society. Section B*, vol. 70, pp. 11–23, 1957.

[17] S. I. Braginskii, "The behavior of a completely ionized plasma in a strong magnetic field," *J. Exptl. Theret. Phys.*, vol. 6, pp. 645–654, 1958.

[18] I. E. Ochs, C. Stollberg, E. Kroupp, Y. Maron, A. Fruchtman, E. J. Kolmes, M. E. Mlodik, and N. J. Fisch, "Current channel evolution in ideal z pinch for general velocity profiles," *Physics of Plasmas*, vol. 26, pp. 1–10, 2019.

[19] M. Cvejić, D. Mikitchuk, E. Kroupp, R. Doron, P. Sharma, Y. Maron, A. L. Velikovich, A. Fruchtman, I. E. Ochs, E. J. Kolmes, and N. J. Fisch, "Self-generated plasma rotation in a z-pinch implosion with preembedded axial magnetic field," *Phys. Rev. Lett.*, vol. 128, p. 015001, Jan 2022.

[20] R. D. McBride, W. A. Stygar, M. E. Cuneo, D. B. Sinars, M. G. Mazarakis, J. J. Leckbee, M. E. Savage, B. T. Hutsel, J. D. Douglass, M. L. Kiefer, B. V. Oliver, G. R. Laity, M. R. Gomez, D. A. Yager-Elorriaga, S. G. Patel, B. M. Kovalchuk, A. A. Kim, P. A. Gourdain, S. N. Bland, S. Portillo, S. C. Bott-Suzuki, F. N. Beg, Y. Maron, R. B. Spielman, D. V. Rose, D. R. Welch, J. C. Zier, J. W. Schumer, J. B. Greenly, A. M. Covington, A. M. Steiner, P. C. Campbell, S. M. Miller, J. M. Woolstrum, N. B. Ramey, A. P. Shah, B. J. Sporer, N. M. Jordan, Y. Y. Lau, and R. M. Gilgenbach, "A primer on pulsed power and linear transformer drivers for high energy density physics applications," *IEEE Transactions on Plasma Science*, vol. 46, pp. 3928–3967, 11 2018.

[21] A. G. Rousskikh, A. S. Zhigalin, V. I. Oreshkin, and R. B. Baksht, "Measuring the compression velocity of a Z pinch in an axial magnetic field," *Physics of Plasmas*, vol. 24, no. 6, 2017.

[22] A. V. Shishlov, R. B. Baksht, S. A. Chaikovsky, A. Y. Labetsky, V. I. Oreshkin, A. G. Rousskikh, and A. V. Fedunin, "Double gas puff z-pinch with axial magnetic field for K-shell radiation production," *BEAMS 2002 - 14th International Conference on High-Power Particle Beams*, vol. 2, no. December 2002, pp. 117–122, 2002.

[23] R. B. Baksht, V. I. Oreshkin, A. G. Rousskikh, and A. S. Zhigalin, "Energy balance in a Z pinch with suppressed Rayleigh-Taylor instability," *Plasma Physics and Controlled Fusion*, vol. 60, no. 3, 2018.

[24] G. G. Zukakishvili, V. V. Aleksandrov, E. V. Grabosvkii, G. M. Oleinik, I. Y. Porofeev, P. V. Sasorov, and I. N. Frolov, "Measurements of the azimuthal magnetic field within imploding multiwire arrays in the angara-5-1 facility," *Plasma Physics Reports*, vol. 31, pp. 908–918, 2005.

[25] J. Greenly, M. Martin, I. Blesener, D. Chalenski, P. Knapp, and R. McBride, "The role of flux advection in the development of the ablation streams and precursors of wire array z-pinches," *AIP Conference Proceedings*, vol. 1088, pp. 53–56, 2009.

[26] K. N. Mitrofanov, E. V. Grabovski, G. M. Oleinik, V. V. Aleksandrov, A. N. Gritsuk, I. N. Frolov, Y. N. Laukhin, P. V. Sasorov, and A. A. Samokhin, "Study of the radial distribution of the magnetic field in the wire array plasma at the angara-5-1 facility," *Plasma Physics Reports*, vol. 38, pp. 797–819, 10 2012.

[27] P.-A. Gourdain, J. B. Greenly, D. A. Hammer, P. F. Knapp, B. R. Kusse, S. A. Pikuz, P. C. Schrafel, and T. C. Shelkovenko, "The impact of cathode diameter on radial foil explosions," *IEEE Transactions on Plasma Science*, vol. 38, no. 12, pp. 3363–3369, 2010.

[28] F. Suzuki-Vidal, S. V. Lebedev, S. N. Bland, G. N. Hall, G. Swadling, A. J. Harvey-Thompson, J. P. Chittenden, A. Marocchino, A. Ciardi, A. Frank, E. G. Blackman, and S. C. Bott, "Generation of episodic magnetically driven plasma jets in a radial foil z-pinch," *Physics of Plasmas*, vol. 17, 11 2010.

[29] I. H. Hutchinson, *Principles of Plasma Diagnostics*. Cambridge University Press, 2002.

[30] V. Ivanov, G. Sarkisov, P. Laca, V. Sotnikov, V. Kantsyrev, B. Jones, C. Coverdale, P. Lepell, C. Deeney, K. Struve, A. Astanovitskiy, D. Fedin, B. Le Galloudec, V. Nalajala, I. Shrestha, and T. Cowan, "Investigation of magnetic fields in 1-ma wire arrays and¡tex¿x¡/tex¿-pinches," *IEEE Transactions on Plasma Science*, vol. 34, no. 5, pp. 2247–2255, 2006.

[31] S. N. Bland, D. J. Ampleford, S. C. Bott, A. Guite, G. N. Hall, S. M. Hardy, S. V. Lebedev, P. Shardlow, A. Harvey-Thompson, F. Suzuki, and K. H. Kwek, "Use of faraday probing to estimate current distribution in wire array z pinches," *Review of Scientific Instruments*, vol. 77, no. 10, p. 10E315, 2006.

[32] A. V. Branitskii, V. D. Vikharev, A. G. Kasimov, S. L. Nedoseev, A. A. Rupasov, G. S. Sarkisov, V. P. Smirnov, V. Y. Tsarfin, and A. A. Shikanov, "Measurement of magnetic fields in high-current z pinch in angara-5-1 using faraday rotation," *Sov. J. Plasma Phys.*, vol. 18, pp. 1131–1137, 1992.

[33] F. S. Felber, F. J. Wessel, N. C. Wild, H. U. Rahman, A. Fisher, C. M. Fowler, M. A. Liberman, and A. L. Velikovich, "Ultrahigh magnetic fields produced in a gas-puff z pinch," *Journal of Applied Physics*, vol. 64, no. 8, pp. 3831–3844, 1988.

[34] V. V. Ivanov, A. A. Anderson, D. Papp, A. L. Astanovitskiy, V. Nalajala, and O. Dmitriev, "Study of magnetic fields and current in the z pinch at stagnation," *Physics of Plasmas*, vol. 22, no. 9, p. 092710, 2015.

[35] S. C. Wilks, A. B. Langdon, T. E. Cowan, M. Roth, M. Singh, S. Hatchett, M. H. Key, D. Pennington, A. MacKinnon, and R. A. Snavely, "Energetic proton generation in ultra-intense laser-solid interactions," *Physics of Plasmas*, vol. 8, pp. 542–549, 2001.

[36] M. Borghesi, A. Schiavi, D. H. Campbell, M. G. Haines, O. Willi, A. J. MacKinnon, L. A. Gizzi, M. Galimberti, R. J. Clarke, and H. Ruhl, "Proton imaging: A diagnostic for inertial confinement fusion/fast ignitor studies," *Plasma Physics and Controlled Fusion*, vol. 43, pp. 267–276, 2001.

[37] A. J. Mackinnon, P. K. Patel, R. P. Town, M. J. Edwards, T. Phillips, S. C. Lerner, D. W. Price, D. Hicks, M. H. Key, S. Hatchett, S. C. Wilks, M. Borghesi, L. Romagnani, S. Kar, T. Toncian, G. Pretzler, O. Willi, M. Koenig, E. Martinolli, S. Lepape, A. Benuzzi-Mounaix, P. Audebert, J. C. Gauthier, J. King, R. Snavely, R. R. Freeman, and T. Boehlly, "Proton radiography as an electromagnetic field and density perturbation diagnostic (invited)," *Review of Scientific Instruments*, vol. 75, pp. 3531–3536, 2004.

[38] P. M. Nilson, L. Willingale, M. C. Kaluza, C. Kamperidis, S. Minardi, M. S. Wei, P. Fernandes, M. Notley, S. Bandyopadhyay, M. Sherlock, R. J. Kingham, M. Tatarakis, Z. Najmudin, W. Rozmus, R. G. Evans, M. G. Haines, A. E. Dangor, and K. Krushelnick, "Magnetic reconnection and plasma dynamics in two-beam laser-solid interactions," *Physical Review Letters*, vol. 97, pp. 1–4, 2006.

[39] C. K. Li, F. H. Séguin, J. A. Frenje, J. R. Rygg, R. D. Petrasso, R. P. Town, P. A. Amendt, S. P. Hatchett, O. L. Landen, A. J. MacKinnon, P. K. Patel, V. A. Smalyuk, T. C. Sangster, and J. P. Knauer, "Measuring e and b fields in laser-produced plasmas with monoenergetic proton radiography," *Physical Review Letters*, vol. 97, pp. 3–6, 2006.

[40] D. Mariscal, C. McGuffey, J. Valenzuela, M. S. Wei, J. P. Chittenden, N. Niasse, R. Presura, S. Haque, M. Wallace, A. Arias, A. Covington, H. Sawada, P. Wiewior, and F. N. Beg, "Measurement of pulsed-power-driven magnetic fields via proton deflectometry," *Applied Physics Letters*, vol. 105, no. 22, p. 224103, 2014.

[41] D. A. Mariscal, *Investigation of the Magnetic Field and Current Topology in Z-pinch Plasmas*. PhD thesis, University of California, San Diego, 2015.

[42] V. Munzar, D. Klir, J. Cikhardt, B. Cikhardtova, J. Kravarik, P. Kubes, and K. Rezac, "Investigation of magnetic fields in z-pinches via multi-mev proton deflectometry," *IEEE Transactions on Plasma Science*, vol. 46, no. 11, pp. 3891–3900, 2018.

[43] F. H. Séguin, C. K. Li, M. J. Manuel, H. G. Rinderknecht, N. Sinenian, J. A. Frenje, J. R. Rygg, D. G. Hicks, R. D. Petrasso, J. Delettrez, R. Betti, F. J. Marshall, and V. A. Smalyuk, "Time evolution of filamentation and self-generated fields in the coronae of directly driven inertial-confinement fusion capsules," *Physics of Plasmas*, vol. 19, 1 2012.

[44] V. Munzar, D. Klir, J. Cikhardt, J. Kravarik, P. Kubes, J. Malir, J. Novotny, K. Rezac, A. V. Shishlov, V. A. Kokshenev, R. K. Cherdizov, and N. A. Ratakhin, "Mapping of azimuthal b-fields in z-pinch plasmas using z-pinch-driven ion deflectometry," *Physics of Plasmas*, vol. 28, 6 2021.

[45] H.-J. Kunze, *Introduction to Plasma Spectroscopy*. Springer-Verlag Berlin Heidelberg, 2009.

[46] E. L. Degl'innocenti and M. Landolfi, *Polarization In Spectral Lines*. Kluwer Academic Publishers, 2005.

[47] I. I. Sobelman, *Atomic Spectra and Radiative Transitions*. Springer, 1992.

[48] W. F. Drake, ed., *Springer Handbook of Atomic, Molecular, and Optical Physics*. Springer Science+Business Media, Inc., 2006.

[49] R. D. Cowan, *The Theory of Atomic Structure and Spectra*. University of California Press, 1981.

[50] F. C. Jahoda, F. L. Ribe, and G. A. Sawyer, "Zeeman-effect magnetic field measurement of a high-temperature plasma," *Phys. Rev.*, vol. 131, pp. 24–29, Jul 1963.

[51] N. J. Peacock and B. A. Norton, "Measurement of megagauss magnetic fields in a plasma focus device," *Phys. Rev. A*, vol. 11, pp. 2142–2146, Jun 1975.

[52] P. G. Carolan, M. J. Forrest, N. J. Peacock, and D. L. Trotman, "Observation of zeeman splitting of spectral lines from the jet plasma," *Plasma Phys. Cntrl. Fusion*, vol. 27, pp. 1101–1124, 1985.

[53] R. Arad, L. Ding, and Y. Maron, "Novel gas-doping technique for local spectroscopic measurements in pulsed-power systems," *Review of Scientific Instruments*, vol. 69, pp. 1529–1533, 1998.

[54] M. R. Gomez, S. B. Hansen, K. J. Peterson, D. E. Bliss, A. L. Carlson, D. C. Lamppa, D. G. Schroen, and G. A. Rochau, "Magnetic field measurements via visible spectroscopy on the z machine," *Review of Scientific Instruments*, vol. 85, pp. 1–4, 2014.

[55] J. T. Banasek, J. T. Engelbrecht, S. A. Pikuz, T. A. Shelkovenko, and D. A. Hammer, "Measuring 10-20 t magnetic fields in single wire explosions using zeeman splitting," *Review of Scientific Instruments*, vol. 87, 2016.

[56] C. Liu, K. Matsuo, S. Ferri, H. K. Chung, S. Lee, S. Sakata, K. F. F. Law, H. Morita, B. Pollock, J. Moody, and S. Fujioka, "Design of zeeman spectroscopy experiment with magnetized silicon plasma generated in the laboratory," *High Energy Density Physics*, vol. 33, 11 2019.

[57] R. Doron, D. Mikitchuk, C. Stollberg, G. Rosenzweig, E. Stambulchik, E. Kroupp, Y. Maron, and D. A. Hammer, "Determination of magnetic fields based on the zeeman effect in regimes inaccessible by zeeman-splitting spectroscopy," *High Energy Density Physics*, 2014.

[58] S. Sahal-Brechot, Dimitrijevic, and N. M. Moreau, "Stark-b database."

[59] E. Stambulchik, K. Tsigutkin, and Y. Maron, "Spectroscopic method for measuring plasma magnetic fields having arbitrary distributions of direction and amplitude," *Phys. Rev. Lett.*, vol. 98, p. 225001, May 2007.

[60] S. Tessarin, D. Mikitchuk, R. Doron, E. Stambulchik, E. Kroupp, Y. Maron, D. A. Hammer, V. L. Jacobs, J. F. Seely, B. V. Oliver, and A. Fisher, "Beyond zeeman spectroscopy: Magnetic-field diagnostics with stark-dominated line shapes," *Physics of Plasmas*, vol. 18, no. 9, p. 093301, 2011.

[61] G. Davara, L. Gregorian, E. Kroupp, and Y. Maron, "Spectroscopic determination of the magnetic-field distribution in an imploding plasma," *Physics of Plasmas*, vol. 5, no. 4, pp. 1068–1075, 1998.

[62] R. P. Golingo, U. Shumlak, and D. J. Den Hartog, "Note: Zeeman splitting measurements in a high-temperature plasma," *Review of Scientific Instruments*, vol. 81, no. 12, p. 126104, 2010.

[63] G. Rosenzweig, *Investigation of the magnetic field distribution and the fundamental properties of an imploding plasma, near and during stagnation*. PhD thesis, Weizmann Institute of Science, 2015.

[64] G. Rosenzweig, E. Kroupp, A. Fisher, and Y. Maron, "Measurements of the spatial magnetic field distribution in a z-pinch plasma throughout the stagnation process," *Journal of Instrumentation*, vol. 12, pp. P09004–P09004, sep 2017.

[65] D. Mikitchuk, M. Cvejić, R. Doron, E. Kroupp, C. Stollberg, Y. Maron, A. L. Velikovich, N. D. Ouart, J. L. Giuliani, T. A. Mehlhorn, E. P. Yu, and A. Fruchtman, "Effects of a preembedded axial magnetic field on the current distribution in a z-pinch implosion," *Phys. Rev. Lett.*, vol. 122, p. 045001, Jan 2019.

[66] G. Rosenzweig, E. Kroupp, T. Queller, A. Starobinets, Y. Maron, V. Tangri, J. L. Giuliani, and A. Fruchtman, "Local measurements of the spatial magnetic field distribution in a z-pinch plasma during and near stagnation using polarization spectroscopy," *Physics of Plasmas*, vol. 27, no. 2, p. 022705, 2020.

[67] H. Goedbloed, R. Keppens, and S. Poedts, *Magnetohydrodynamics of Laboratory and Astrophysical Plasmas*. Cambridge University Press, 2019.

[68] F. F. Chen, *Introduction to Plasma Physics and Controlled Fusion*. Springer International Publishing, 2016.

[69] R. J. Goldston and P. H. Rutherford, *Introduction to Plasma Physics*. IOP Publishing Ltd, 1995.

[70] B. M. Paul, *Fundamentals of Plasma Physics*. Cambridge University Press, 2006.

[71] K. Hutter and Y. Wang, *Fluid and Thermodynamics Volume 2: Advanced Fluid Mechanics and Thermodynamic Fundamentals*. Springer International Publishing Switzerland, 2016.

[72] C. E. Seyler, "Axial magnetic flux amplification in hall-magnetohydrodynamic simulations of externally magnetized z-pinches," *Physics of Plasmas*, vol. 27, 9 2020.

[73] M. M. Marinak, G. D. Kerbel, N. A. Gentile, O. Jones, D. Munro, S. Pollaine, T. R. Dittrich, and S. W. Haan, "Three-dimensional hydra simulations of national ignition facility targets," *Physics of Plasmas*, vol. 8, pp. 2275–2280, 5 2001.

[74] K. Miyamoto, *Plasma Physics and Controlled Nuclear Fusion*. Springer-Verlag Berlin Heidelberg, 2016.

[75] M. S. Roberts and J. W. Jacobs, "The effects of forced small-wavelength, finite-bandwidth initial perturbations and miscibility on the turbulent rayleigh-taylor instability," *Journal of Fluid Mechanics*, vol. 787, pp. 50–83, 12 2015.

[76] E. G. Harris, "Rayleigh-taylor instabilities of a collapsing cylindrical shell in a magnetic field," *Physics of Fluids*, vol. 5, pp. 1057–1062, 1962.

[77] A. B. Bud'ko, F. S. Felber, A. I. Kleev, M. A. Liberman, and A. L. Velikovich, "Stability analysis of dynamic z pinches and theta pinches," *Physics of Fluids B*, vol. 1, pp. 598–607, 1989.

[78] N. Qi, H. Sze, B. H. Failor, J. Banister, J. S. Levine, J. C. Riordan, P. Steen, P. Sincerny, and D. Lojewski, "Magnetic rayleigh-taylor instability mitigation in large-diameter gas puff z-pinch implosions," *Physics of Plasmas*, vol. 15, 2008.

[79] M. R. Weis, P. Zhang, Y. Y. Lau, I. M. Rittersdorf, J. C. Zier, R. M. Gilgenbach, M. H. Hess, and K. J. Peterson, "Temporal evolution of surface ripples on a finite plasma slab subject to the magneto-rayleigh-taylor instability," *Physics of Plasmas*, vol. 21, 2014.

[80] D. Mikitchuk, C. Stollberg, R. Doron, E. Kroupp, Y. Maron, H. R. Strauss, A. L. Velikovich, and J. L. Giuliani, "Mitigation of instabilities in a z-pinch plasma by a preembedded axial magnetic field," *IEEE Transactions on Plasma Science*, vol. 42, pp. 2524–2525, 10 2014.

[81] F. Conti, N. Aybar, J. Narkis, J. C. Valenzuela, H. U. Rahman, E. Ruskov, E. Dutra, S. Haque, A. Covington, and F. N. Beg, "Study of stability in a liner-on-target gas puff z-pinch as a function of pre-embedded axial magnetic field," *Physics of Plasmas*, vol. 27, 1 2020.

[82] J. Narkis, F. Conti, A. L. Velikovich, and F. N. Beg, "Mitigation of magneto-rayleigh-taylor instability growth in a triple-nozzle, neutron-producing gas-puff z pinch," *Physical Review E*, vol. 104, 8 2021.

[83] E. Kuffel, W. S. Zaengl, and J. Kuffel, *High Voltage Engineering Fundamentals (2nd Edition)*. Elsevier, 2000.

[84] W. Kies, "Power limits for dynamical pinch discharges," *Plasma Physics and Controlled Fusion*, vol. 28, pp. 1645–1657, 1986.

[85] T. W. Hussey, M. K. Matzen, and N. F. Roderick, "Large-scale-length nonuniformities in gas puff implosions," *Journal of Applied Physics*, vol. 59, pp. 2677–2684, 1986.

[86] F. Conti, J. C. Valenzuela, V. Fadeev, N. Aybar, D. B. Reisman, A. Williams, G. Collins, J. Narkis, M. P. Ross, F. N. Beg, and R. B. Spielman, "Ma-class linear transformer driver for z-pinch research," *Physical Review Accelerators and Beams*, vol. 23, p. 90401, 2020.

[87] J. R. Woodworth, W. E. Fowler, B. S. Stoltzfus, W. A. Stygar, M. E. Sceiford, M. G. Mazarakis, H. D. Anderson, M. J. Harden, J. R. Blickem, R. White, and A. A. Kim, "Compact 810 kA linear transformer driver cavity," *Physical Review Special Topics - Accelerators and Beams*, vol. 14, no. 4, pp. 1–7, 2011.

[88] F. Conti, J. C. Valenzuela, N. Aybar, F. J. Wessel, M. P. Ross, J. Narkis, H. U. Rahman, E. Ruskov, and F. N. Beg, "Characterization of a liner-on-target gas injector for staged z-pinch experiments," *IEEE Transactions on Plasma Science*, vol. 46, pp. 3855–3863, 2019.

[89] M. Wolfgang, *3 - Optical Flow Visualization*. San Diego: Academic Press, second edition ed., 1987.

[90] M. J. Weber, *Handbook of Optical Materials*. CRC Press LLC, 2002.

[91] D. B. Reisman, A. Toor, R. C. Cauble, C. A. Hall, J. R. Asay, M. D. Knudson, and M. D. Furnish, "Magnetically driven isentropic compression experiments on the z accelerator," *Journal of Applied Physics*, vol. 89, no. 3, pp. 1625–1633, 2001.

[92] R. M. More, K. H. Warren, D. A. Young, and G. B. Zimmerman, "A new quotidian equation of state (qeos) for hot dense matter," *The Physics of Fluids*, vol. 31, no. 10, pp. 3059–3078, 1988.

[93] D. Mikitchuk, *Investigation of the Compression of Magnetized Plasma and Magnetic Flux*. PhD thesis, Weizmann Institute of Science, 2016.

[94] N. I. of Standards and Technology, "Atomic spectral database," 2017.

[95] H.-K. Chung, M. Chen, W. Morgan, Y. Ralchenko, and R. Lee, "Flychk: Generalized population kinetics and spectral model for rapid spectroscopic analysis for all elements," *High Energy Density Physics*, vol. 1, no. 1, pp. 3–12, 2005.

[96] J. L. Giuliani, J. W. Thornhill, E. Kroupp, D. Osin, Y. Maron, A. Dasgupta, J. P. Apruzese, A. L. Velikovich, Y. K. Chong, A. Starobinets, V. Fisher, Y. Zarnitsky, V. Bernshtam, A. Fisher, T. A. Mehlhorn, and C. Deeney, "Effective versus ion thermal temperatures in the weizmann ne z-pinch: Modeling and stagnation physics," *Physics of Plasmas*, vol. 21, no. 3, p. 031209, 2014.

[97] B. Jones, C. A. Jennings, J. E. Bailey, G. A. Rochau, Y. Maron, C. A. Coverdale, E. P. Yu, S. B. Hansen, D. J. Ampleford, P. W. Lake, G. Dunham, M. E. Cuneo, C. Deeney, D. V. Fisher, V. I. Fisher, V. Bernshtam, A. Starobinets, and L. Weingarten, "Doppler measurement of implosion velocity in fast z-pinch x-ray sources," *Physical Review E - Statistical, Nonlinear, and Soft Matter Physics*, vol. 84, 11 2011.

[98] S. A. Slutz, M. C. Herrmann, R. A. Vesey, A. B. Sefkow, D. B. Sinars, D. C. Rovang, K. J. Peterson, and M. E. Cuneo, "Pulsed-power-driven cylindrical liner implosions of laser preheated fuel magnetized with an axial field," *Physics of Plasmas*, vol. 17, no. 5, 2010.

[99] H. U. Rahman, P. Ney, F. J. Wessel, and N. Rostoker, "Staged pinch for controlled thermonuclear fusion," *Journal of Plasma Physics*, vol. 58, no. PART 2, pp. 367–379, 1997.

[100] A. L. Velikovich, F. L. Cochran, and J. Davis, "Suppression of rayleigh-taylor instability in z-pinch loads with tailored density profiles," *Physical Review Letters*, vol. 77, no. 5, pp. 853–856, 1996.

[101] N. Qi, E. W. Rosenberg, P. A. Gourdain, P. W. De Grouchy, B. R. Kusse, D. A. Hammer, K. S. Bell, T. A. Shelkovenko, W. M. Potter, L. Atoyan, A. D. Cahill, M. Evans, J. B. Greenly, C. L. Hoyt, S. A. Pikuz, P. C. Schrafel, E. Kroupp, A. Fisher, and Y. Maron, "Study of gas-puff Z-pinches on COBRA," *Physics of Plasmas*, vol. 21, no. 11, 2014.

[102] H. U. Rahman, E. Ruskov, P. Ney, F. Conti, J. C. Valenzuela, N. Aybar, J. Narkis, F. N. Beg, E. Dutra, and A. Covington, "Ar and Kr on deuterium gas-puff staged Z-pinch implosions on a 1-MA driver: Experiment and simulation," *Physics of Plasmas*, vol. 26, no. 5, 2019.

[103] E. M. Epperlein and M. G. Haines, "Plasma transport coefficients in a magnetic field by direct numerical solution of the fokker–planck equation," *Physics of Fluids*, vol. 29, p. 1029, 1986.

[104] M. E. Foord, Y. Maron, G. Davara, L. Gregorian, and A. Fisher, "Particle velocity distributions and ionization processes in a gas-puff z-pinch," *Physical Review Letters; (United States)*, vol. 72:24, 6 1994.

[105] E. Ruskov, P. Ney, and H. U. Rahman, "Staged z-pinch modeling of high and low atomic number liners compressing deuterium targets using parameters of the z pulsed power facility," *Physics of Plasmas*, vol. 28, 11 2021.